IMPACT OF TIME AND SPATIAL AVERAGES ON THE ENERGY BALANCE CLOSURE

A dissertation submitted to the

Bayreuth Graduate School of Mathematical and Natural Sciences
University of Bayreuth, Germany

to attain the academic degree of

Doctor of Natural Sciences
(Dr. rer. nat.)

presented by

Doojdao Charuchittipan
M.Sc.
born 9 April 1977
in Koh Samui, Thailand

Thesis Supervisor
PROF. DR. THOMAS FOKEN

Bayreuth, 2013

IMPACT OF TIME AND SPATIAL AVERAGES ON THE ENERGY BALANCE CLOSURE

presented by

DOOJDAO CHARUCHITTIPAN, M.Sc.

supervised by

PROF. DR. THOMAS FOKEN

DEPARTMENT OF MICROMETEOROLOGY
UNIVERSITY OF BAYREUTH

This doctoral thesis was prepared at the Department of Micrometeorology, University of Bayreuth from August 2009 until April 2013 and was supervised by Prof. Dr. Thomas Foken.

This is a full reprint of the dissertation submitted to attain the academic degree of Doctor of Natural Sciences (Dr. rer. nat.) and approved by the Bayreuth Graduate School of Mathematical and Natural Sciences (BayNAT) of the University of Bayreuth.

Date of submission: 5 June 2013

Date of defense: 16 July 2013

Director: Prof. Dr. Franz Xaver Schmid

Doctoral Committee:

Prof. Dr. Thomas Foken, 1st reviewer

Prof. Dr. Bernd Huwe, 2nd reviewer

Prof. Dr. Andreas Held, Chairman

Dr. Johannes Lüers

Acknowledgements

I wish to express my gratitude to:

My supervisor, Prof. Dr. Thomas Foken, who always shares his profound knowledge with his students. His endless support and guidance along with his valuable discussion in all stage of my works are very meaningful for completing this thesis.

Current and former members of the department of Micrometeorology at the University of Bayreuth, for their assistance and support throughout my years in Bayreuth. Their contributed discussion and comments are very helpful to my works. In particular Dr. Rafael Eigenmann, for kindly translating my abstract from English into German and Dr. Wolfgang Babel, who partially involved in my submitted paper and edited my abstract.

Dr. Johannes Lüers and Prof. Dr. Andreas Held for being part of my mentorate committee. Prof. Dr. Bernd Huwe for being the second reviewer.

Everyone in the ELSH project, in particular Dr. Frank Beyich and Jens-Peter Leps of Deutscher Wetterdienst, for providing many data from the LITFASS-2003 experiment that were extensively analyzed throughout my thesis. Also, Prof. Dr. Jens Bange, Yvonne Breitenbach and Dr. Daniel Villagrasa of the Institute for Geoscience, Eberhard Karls Universität Tübingen, for providing the Helipod data, which allows me to carry out the analysis in the spatial average part very effectively.

Dr. Matthias Mauder, for providing many useful discussions and comments to my paper. This is very helpful for my analysis in the time average part. He also provided the wavelet analysis code, which I have modified to use in many parts of this thesis. Dr. Natascha Kjlun, for allowing me to use her LPDM-B footprint model. This is a very essential tool for my analysis in the spatial average part. Dr. Bernhard Winkler of Rechenzentrum at the University of Bayreuth, for guiding me through the University Linux cluster. This is also help for me to run the footprint model a lot more faster.

All the co-authors of my submitted paper, for their contributions to the manuscript. Everyone who participated in the LITFASS-2003 experiment, who has produced many good quality data, which I have used throughout my thesis.

Pira Korsieporn, Boripont Manmontri, Suparat Chuechote, Krist Dacharux, and Weeraya Donsomsakulkij for proofreading my thesis.

My family, who constantly supports me through out my study.

I was financially supported by the German Research Foundation (DFG) within the projects FO 226/20-1 between August 2009 - September 2012 and granted a doctorate finalizing funding from Büro der Frauenbeauftragten of University of Bayreuth from October 2012 to December 2012. I am very thankful for all these supports.

Abstract

Secondary circulations are large and relatively stationary eddies, which are caused by the surface heterogeneity and normally reside away from the ground. They are believed to be the cause of the energy balance closure problem at the earth's surface, because their contribution to the turbulent fluxes is missed by a fixed eddy-covariance tower measurement that has a typical averaging time of 30 minutes. In this thesis, data from the LITFASS-2003 experiment was used to investigate the impact of time and spatial averages on the energy balance closure. This data consisted of many observations over a large heterogeneous landscape that could generate secondary circulations; some of which might be still near the earth's surface.

For the time average analysis, the averaging time was extended to increase the possibility that secondary circulations were picked up by the sensor. Two approaches, which were the modified ogive analysis and the block ensemble average, were applied to analyze the data from ground-based measurements. The modified ogive analysis requiring a steady state condition, could extend the averaging time up to a few hours and suggested that an averaging time of 30 minutes was still overall sufficient for the eddy-covariance measurement over low vegetation. The block ensemble average, on the contrary, did not require a steady state condition, but could extend the averaging time to several days. However, this approach could only improve the energy balance closure for some sites during specific periods, when secondary circulations existed in the vicinity of the sensor. Based on this approach, it was found that the near-surface secondary circulations mainly transported sensible heat, which led to an alternative energy balance correction by the buoyancy flux ratio approach, in which the attribution of the residual depended on the relative contribution of the sensible heat flux to the buoyancy flux. The fraction of the residual attributed to the sensible heat flux by this energy balance correction was larger than in the energy balance correction that preserved the Bowen ratio.

In the spatial average analysis, two energy balance correction approaches, the buoyancy flux ratio and the Bowen ratio approaches, were applied to the area-averaged fluxes (composite fluxes) in order to include contribution from secondary circulations. These composite fluxes were aggregated from multiple ground-based measurements. The energy balance corrected fluxes were validated against the spatial average fluxes, which were measured by an aircraft and a large aperture scintillometer (LAS). In this validation, the backward Lagrangian footprint model was

used to estimate the source area of the measurement. It was found that both energy balance correction approaches did improve the agreement between time and spatial averages fluxes. This suggested that the contribution from secondary circulations could be properly accounted by the energy balance correction.

All findings in this thesis, therefore, depict that secondary circulations significantly transport energy in the atmospheric surface layer. The energy balance correction, accomplished by using either the Bowen ratio approach or the buoyancy flux ratio approach, is necessary to estimate the actual vertical transport of energy at the earth's surface.

Zusammenfassung

Sekundäre Zirkulationen sind große, nahe zu stationäre Eddies, die durch Oberflächenheterogenitäten verursacht werden und sich normalerweise entfernt vom Boden befinden. Es wird angenommen, dass sie die Ursache für das Energiebilanzschließungsproblem an der Erdoberfläche sind, da ihre Beiträge zu den turbulenten Flüssen nicht von den räumlich stationären Masten der Eddy-Kovarianz-Messung, deren typisches Mittelungsintervall 30 Minuten ist, erfasst werden. In dieser Arbeit werden Daten aus dem LITFASS-2003 Experiment verwendet, um den Einfluss der zeitlichen und räumlichen Mittelung auf die Energiebilanzschließung zu untersuchen. Das Experiment bestand aus umfassenden Messungen über stark heterogener Landschaft und bot somit die Möglichkeit, eine Vielzahl an Aspekten sekundärer Zirkulationen zu untersuchen.

In Bezug auf die zeitliche Mittelung wurde das Mittelungsintervall ausgedehnt, um den Beitrag potentieller sekundärer Zirkulationen zu berücksichtigen. Zwei Ansätze wurden mit Hilfe der Bodenmessungen angewandt: die modifizierte Ogivenanalyse und die Blockmittelungsmethode. Die modifizierte Ogivenanalyse, die stationäre Bedingungen bentigt, kann die Mittelungszeit bis zu mehreren Stunden ausdehnen und zeigt, dass die Mittelungszeit von 30 Minuten im Allgemeinen für Eddy-Kovarianz-Messungen ausreicht. Die Blockmittelungsmethode, die keine stationären Bedingungen bentigt, kann die Mittelungszeit auf mehrere Tage ausdehnen. Jedoch kann sie die Energiebilanzschließung nur für einige Standorte und nur zu bestimmten Zeiten, in denen sich die sekundären Zirkulationen in der Nähe des Sensors befinden, verbessern. Diese bodennahen sekundären Zirkulationen transportieren hauptsächlich fühlbare Wärme. Diese Ergebnisse führen zu einer alternativen Korrektur der Energiebilanzschließung durch die Methode des Auftriebsstromverhältnisses, welches den grßeren Anteil des Residuums dem fühlbaren Wärmestrom zuordnet.

Bei der räumlichen Mittelung wurde die Energiebilanzschließungskorrektur auf die flächengemittelten oder zusammengesetzten Flüsse, die aus mehreren Bodenmessungen zusammengefasst wurden, angewandt, um Beiträge von sekundären Zirkulationen mit einzubeziehen. Diese energiebilanzkorrigierten Flüsse wurden gegen Flugzeugmessungen und einem Grossflächen-Scintillometer (LAS), die beide flächengemittelte Flüsse liefern, unter Zuhilfenahme eines Footprintmodells validiert. Es

konnte gezeigt werden, dass die Energiebilanzkorrektur die Übereinstimmung zwischen zeitlich und räumlich gemittelten Flüssen verbessert.

Alle Ergebnisse dieser Arbeit lassen darauf schließen, dass sekundäre Zirkulationen einen signifikanten Anteil der Energie in der Bodenschicht transportieren. Folglich ist eine Energiebilanzkorrektur notwendig, um den tatsächlichen vertikalen Transport in der Bodenschicht zu bestimmen.

Contents

List of Tables

List of Figures

Nomenclature

Abbreviations

ABL	Atmospheric boundary layer
ASL	Atmospheric surface layer
EC	Eddy-covariance
EBC-Bo	Energy balance correction with the Bowen ratio approach
EBC-HB	Energy balance correction with the buoyancy flux ratio approach
EBEX	Energy Balance Experiment
FFT	Fast Fourier transform
LAS	Large aperture scintillometer
LES	Large-eddies simulation
LITFASS	Lindenberg Inhomogeneous Terrain–Fluxes between Atmosphere and Surface: a long-term Study
LPDM-B	Backward Lagrangian dispersion model
LS	Lagrangian stochastic
MOG	Modified ogive analysis
MOL	Meteorological observatory Lindenberg
NC	No energy balance correction
NWP	Numerical weather prediction
SC	Secondary circulations
TOS	Turbulence organized structure
UTC	Coordinated Universal Time

Symbols

Bo	Bowen ratio
c_p	Specific heat of air at constant pressure [$\approx 10^3$ J kg^{-1} K^{-1}]
c_s	Concentration footprint

$\tilde{c}$	Mesoscale term of variable c
$Co_{w,c}$	Cospectrum
d	Displacement height [m]
f	Frequency [Hz]
F	Area-averaged flux
F_c	CO_2 flux [μmol $m^{-2}s^{-1}$]
F_s	Flux footprint
$\overline{F}_{30}$	Turbulent flux at 30 minutes
$\overline{F}_{4hr}$	Turbulent flux at 4 hours
g	Gravitational acceleration (9.80 m s^{-2})
h_0	Elevation or height above sea level [m]
h_c	Canopy height [m]
H	Hyperbolic hole size
$I\uparrow$	longwave up-welling radiation [W m^{-2}]
$I\downarrow$	longwave down-welling radiation [W m^{-2}]
k_v	von Karman constant (≈ 0.4)
$K\uparrow$	shortwave up-welling radiation [W m^{-2}]
$K\downarrow$	shortwave down-welling radiation [W m^{-2}]
L	Obukhov length [m]
p	Air pressure [N m^{-2} or Pascal]
P	Time period [s]
$og_{w,c}$	Ogive function
Q_*	Net radiation [W m^{-2}]
Q_B	Buoyancy flux [W m^{-2}]
Q_E	Latent heat flux [W m^{-2}]
$Q_E^{\mathrm{EBC-Bo}}$	Latent heat flux as corrected by the Bowen ratio approach [W m^{-2}]
$Q_E^{\mathrm{EBC-HB}}$	Latent heat flux as corrected by the buoyancy flux ratio approach [W m^{-2}]
$\tilde{Q}_E$	Mesoscale flux of latent heat [W m^{-2}]
Q_G	Ground heat flux [W m^{-2}]
Q_H	Sensible heat flux [W m^{-2}]
$Q_H^{\mathrm{EBC-Bo}}$	Sensible heat flux as corrected by the Bowen ratio approach [W m^{-2}]

$Q_H^{\mathrm{EBC-HB}}$	Sensible heat flux as corrected by the buoyancy flux ratio approach [W m^{-2}]
$\tilde{Q}_H$	Mesoscale flux of sensible heat [W m^{-2}]
Q_i	The i^{th} quadrant
Ri	Bulk Richardson number
Res	Residual
SW	Source weight matrix
SW^{nor}	Normalized source weight matrix
t	Time [s]
T	Temperature [K]
(u, v, w)	Velocity components [m s^{-1}]
u_*	Friction velocity [m s^{-1}]
U	Wind speed [m s^{-1}]
x	Fetch distance [m]
z	Height above ground or vertical displacement [m]
z_0	Surface roughness length [m]
z_i	Boundary layer depth or mixed layer height[m]
z_m	Measurement height [m]
δ	Internal boundary layer height [m]
Δt	time step [second]
Δ_{max}	Maximum flux difference
η	Width of an error band
θ	Wind direction or undisturbed wind sector [Degree]
λ	Heat of evaporation of water [J kg^{-1}]
ρ	Air density [kg m^{-3}]
τ	Time period [s]

Single-used symbols are explained in the text and may not appear in this list.

1

Introduction

The atmospheric boundary layer (ABL) is the lowest 1-2 km of the atmosphere. Its most bottom part, the atmospheric surface layer (ASL), is the most immediately affected by the earth's surface. This is where the vital exchanges of energy and matter, such as momentum, sensible heat and water vapor, between the earth's surface and the atmosphere take place. Full details of the ABL and ASL are available in many textbooks, for example Stull (1988), Kaimal and Finnigan (1994) and Foken (2008b).

To deepen our understanding of the ASL and all the exchange processes, micrometeorologists have conducted many experiments since about the 1920's. They quantify these exchange processes with the surface fluxes of energy and matter, which are currently widely measured by the eddy-covariance (EC) measurement (Aubinet et al., 2012) on a fixed-tower system. The extensive developments of the sonic anemometer and gas analyser, which are important instruments in the EC measurement, over the past 10-20 years not only made the EC measurement a lot easier, but also allow us to measure fluxes continuously over a long period.

With the ability to measure the carbon dioxide and other traced gases fluxes, the EC measurement has became even more popular in the ecological research. Nowadays, there is a global network of EC measurements, FLUXNET (Baldocchi et al., 2001), which continuously monitors the exchange of energy and matter between the biosphere and the atmosphere on a long-term basis since 1990's.

Such measurement is indeed an integral part of many atmospheric models. For instance, the information on the ASL provides parameter inputs into the numerical weather prediction model (NWP), where the knowledge on surface fluxes is very important (Warner, 2011). Therefore, the accuracy of the EC measurement is definitely very crucial to many branches of research as well as our daily lives.

1.1 Energy balance closure at the earth's surface

This thesis develops around one of the major concerns in the ASL, the energy balance closure problem, which has been aware of since 1980's. Many micrometeorological experiments over low vegetation, for example the EBEX-2000 experiment (EBEX, 'Energy Balance Experiment', Oncley et al., 2007) and the LITFASS-2003 experiment ((LITFASS, 'Lindenberg Inhomogeneous TerrainFluxes between Atmosphere and Surface: a long-term Study', Beyrich and Mengelkamp, 2006), show that the available energy, which is the sum of the net radiation and the ground heat flux, is larger than the sum of the sensible and latent heat fluxes. To conserve energy, the missing energy is replaced by the residual. Then for the homogeneous and stationary ASL, the energy budget equation over low vegetation at the earth's surface becomes

$$Res = -Q^* - (Q_G + Q_H + Q_E), \tag{1.1}$$

where Res is the residual, Q^* is the net radiation, Q_G is the ground heat flux, Q_H is the sensible heat flux, and Q_E is the latent heat flux. Each energy flux in Eq. 1.1 is positive, when it is transported away from the ground.

Among all energy fluxes in Eq. 1.1, Q^* is mostly the largest, however, come with a good measurement accuracy, while Q_G is mostly the smallest. Therefore, measurement accuracies of both Q^* and Q_G do not account for the energy balance closure (Kohsiek et al., 2007; Liebethal et al., 2005) and the residual is most likely caused by an EC tower measurement, which is normally used for measuring Q_H and Q_E. An EC tower measurement is technically a fixed point in space that can only measure eddies, which have moved pass the sensor. If eddies are stationary or moving very slowly, they may not or never move pass the sensor within a typical averaging time of 30 minutes. Therefore, their contributions are definitely missed by an EC tower measurement. More details of the energy balance closure as well as additional comments on surface fluxes measurement can be found in Foken (2008a), Mahrt (2010), Foken et al. (2011) and Leuning et al. (2012).

1.2 Secondary circulations

According to several studies by a large-eddies simulation (LES), the energy imbalance can be significantly improved by including low frequency contributions from the secondary circulations (SC) or turbulence organized structure (TOS, Inagaki et al., 2006; Kanda et al., 2004; Steinfeld et al., 2007). SC are large scale eddies

(several kilometers) and relatively stationary (either static or move very slowly). They are generated by the surface heterogeneity (Stoy et al., 2013) and normally move away from the ground. Their contributions to the low frequency part of the turbulent spectrum may not be entirely captured by an EC tower measurement, which is operated near the earth's surface and typically averaged over a period of 30 minutes. This result in the underestimation of Q_H and Q_E, which are normally measured by an EC tower.

In this thesis, data from the LITFASS-2003 experiment was used to study the energy balance closure under the impact of time and spatial averages. This experiment collected high quality data set with many instruments over a large heterogeneous landscape, which could generate SC. Some of which might still reside near the earth's surface and would show their influences over the energy balance closure. More details of the LITFASS-2003 experiment and its energy balance closure can be found in Beyrich and Mengelkamp (2006) and Foken et al. (2010).

1.2.1 Time average

An EC measurement on a fixed tower seems to be the most convenient way to measure surface fluxes. Given that 30-minute averaging time can be too short, the averaging time extension beyond 30 minutes may increase the possibility of slow moving eddies to move past the sensor. There are two approaches for investigating the averaging time extensions, the ogive analysis (Desjardins et al., 1989; Oncley et al., 1990) and the block ensemble average (Bernstein, 1966, 1970; Finnigan et al., 2003).

The ogive analysis uses the turbulent spectra to estimate the turbulent fluxes at different frequency ranges. Hence it is possible to evaluate how much the low frequency parts contribute to the turbulent fluxes measured by the EC method. In Foken et al. (2006), the ogive analysis was applied to the data measured over the maize field (station A6) of the LITFASS-2003 experiment. It was mainly focused on the data from three selected days, which the averaging time was extended up to 4 hours. It was found that the time extension would not significantly increase the turbulent fluxes.

For the block ensemble average, low frequency contributions from long term fluctuations over several hours to days are added to the total fluxes . In Mauder and Foken (2006), it was also applied to the data set from the same maize field of the LITFASS-2003 experiment (A6). The selected long period was 15 days, while the block ensemble averaging period was varied from 5 minutes to 5 days. This

study shows that the block ensemble average can close energy balance at a longer averaging time.

In this thesis, both ogive analysis and block ensemble average were applied to data from all EC towers of the LITFASS-2003 experiment. If SC does matter to the energy balance closure, this study would reveal an appropriate energy balance correction in order to estimate the actual vertical transport of energy at the earth's surface.

1.2.2 Spatial average

Even the averaging time extension can increase the possibility to measure slow moving SC, a fixed-tower measurement is still unable to detect stationary SC. To overcome this weakness, a measurement which can collect data from multiple locations almost instantly is suggested. The appropriate statistics of this measurement are the spatial averaged statistics.

This type of measurement was available during the LITFASS-2003 experiment with the Helipod (Bange and Roth, 1999; Bange et al., 2002) and the large aperture scintillometer (LAS). These measurements can sample both stationary and slow moving SC. Therefore, they can be used to validate the energy balance corrected fluxes as suggested from the time average analysis. This validation needs an additional tool to relate the time and spatial averages together. In this thesis, the footprint analysis was used for this task.

Both studies in time and spatial averages would reveal how SC contribute to the surface fluxes as well as the necessity to include this contribution to the actual vertical transport of energy, which would lead to the suggestion of appropriate parameterizations in the ASL.

2

Tools

To carry out all investigations in this thesis, many tools, which could be some mathematical techniques or atmospheric models, are required. All necessary ones are presented in this chapter.

2.1 Averaging operators

Since the atmospheric turbulence is non-linear, meteorologists analyse and report the atmospheric properties like wind velocity, temperature and humidity, in term of statistics. These statistics can be obtained through suitable averaging operators, which produce representative statistics of the interested system. There are three different averaging operators: time average, spatial average and ensemble average. Only brief descriptions of each operator are presented here. Intensive details of these operators when apply to the atmospheric data can be found in any introductory books in the atmospheric sciences. For simplification, one dimensional flow is assumed. In this case, any variable $f(x,t)$ is a function of space (x) and time (t).

2.1.1 Time average:

The time average of f is denoted by $\overline{f}$. It is calculated from set of data collected at a fixed point in space over time interval P. It can be defined in both discrete and continuous data set as

$$\text{discrete} \qquad \overline{f} = \frac{1}{N}\sum_{i=1}^{N} f(x,i), \tag{2.1}$$

$$\text{continuous} \qquad \overline{f} = \frac{1}{P}\int_{t_0}^{t_0+P} f(x,t)\,dt, \tag{2.2}$$

where N is the number of data points in a time interval P. For discrete case

$$t = i\Delta t \text{ and } \Delta t = P/N \tag{2.3}$$

2.1.2 Spatial average:

The spatial average of f is denoted by ${}^{s}\overline{f}$ and calculated from set of data collected at an instant of time over a spatial domain X. It can be defined as

$$\text{discrete} \qquad {}^{s}\overline{f} = \frac{1}{N}\sum_{j=1}^{N} f(j,t), \tag{2.4}$$

$$\text{continuous} \qquad {}^{s}\overline{f} = \frac{1}{X}\int_{x_0}^{x_0+X} f(x,t)\,dx, \tag{2.5}$$

where N is the number of data points in a spatial domain X. For discrete case

$$x = j\Delta x \text{ and } \Delta x = X/N \tag{2.6}$$

This averaging operator may extend to an area or a volume average.

2.1.3 Ensemble average:

The ensemble average of f is denoted by $\langle f \rangle$, and calculated from n identical experiments. It is defined as

$$\langle f \rangle = \frac{1}{N}\sum_{i=1}^{N} f_i(x,t), \tag{2.7}$$

where N is the number of data points collected from n identical experiments.

The representative statistics, which can apply to all the governing equations, must satisfy the 'Reynolds averaging rules' (section 2.2). Among these three averaging operators, only the ensemble average is qualified. In controllable experiments, where number of experiments can be repeated with the same conditions, the ensemble average is possible. Unfortunately, in the uncontrollable atmosphere, experiments cannot be repeated with the same conditions. However, under a specific circumstance, when the atmosphere is homogeneous (statistics do not change with space) and stationary (or steady state condition, statistics do not change with time),

all three averaging operators are equivalent. This is known as the ergodic condition.

$$\overline{f} = \ {}^{s}\overline{f} = \langle f \rangle \tag{2.8}$$

2.2 Reynolds averaging rules

Let's assume that the atmosphere is homogeneous and stationary, which makes the ergodic condition to be valid. Under such condition, the time average of variable f is constant over a period P and a spatial domain X. Therefore, at any point in this period and spatial domain,

$$f(\mathbf{x}, t) = \langle f(\mathbf{x}, t) \rangle + f'(\mathbf{x}, t) = \overline{f} + f'(\mathbf{x}, t), \tag{2.9}$$

where the turbulence term $f'(\mathbf{x}, t)$ is the fluctuation from the mean. This expression is known as the 'Reynolds decomposition'. By applying the Reynolds decomposition to atmospheric variables f and g, they obey the 'Reynolds averaging rules', which are

$$(i) \qquad \overline{f+g} = \overline{f} + \overline{g} \tag{2.10}$$

$$(ii) \qquad \overline{k\,f} = k\,\overline{f} \tag{2.11}$$

$$(iii) \qquad \overline{\overline{f}\,g} = \overline{f}\,\overline{g} \tag{2.12}$$

$$(iv) \qquad \overline{\lim f_n} = \lim \overline{f_n} \tag{2.13}$$

With k is constant and f_n is a sequence of functions. The last averaging rule can be interpreted as the commutation between the averaging and differential (or integral) operators, such that

$$\overline{\frac{\partial f}{\partial t}} = \frac{\partial \overline{f}}{\partial t} \ \text{ and } \ \overline{\int_a^b f\,dt} = \int_a^b \overline{f}\,dt \tag{2.14}$$

This leads to

$$\overline{\overline{f}} = \overline{f} \tag{2.15}$$

$$\overline{f'} = 0 \tag{2.16}$$

$$\overline{fg} = \overline{f}\,\overline{g} + \overline{f'g'} \tag{2.17}$$

More details of Reynolds averaging rules when apply to meteorology can be found in most elementary textbook or many early publications in atmospheric sciences such

as de Feriet (1951).

2.3 Software package TK2/3 and flux corrections

One important task in this thesis is to analyse the data obtained from all micrometeorological stations (EC towers). The software package TK2 (the lastest version is available as TK3, Mauder and Foken, 2004, 2011; Mauder et al., 2006) was used for this task. This software package can calculate turbulent fluxes accordingly to a standard EC approach (Aubinet et al., 2012) with many choices of flux corrections. These following flux corrections were used in this thesis. The cross-correlation analysis was used for fixing a time delay between a sonic anemometer and a hygrometer. The planar-fit rotation was used to align a sonic anemometer with a long term mean streamline (Wilczak et al., 2001). The Moore correction was used to correct the spectral loss in the high frequency range (Moore, 1986). The SND correction was used to convert a sonic temperature, which is recorded by a sonic anemometer, to an actual temperature (Schotanus et al., 1983). The WPL correction was used to correct a density fluctuation (Webb et al., 1980). The Tanner correction was used to correct the cross sensitivity between H_2O and O_2 molecules (Tanner et al., 1993), which was only applied for the Krypton Hygrometer KH20. More details of flux corrections can be found in Foken et al. (2012).

TK2 can also assign quality flags to the data. These quality flags are the steady state flag, the integral turbulence characteristic (ITC) flag (Foken and Wichura, 1996) and combined flag. The steady state flag is a result of the steady state test and represents the stationarity of the data. The ITC flag is the result of the flux variance similarity test and represents a development of turbulent conditions. The combined flag is the combination of the steady state and ITC flags. All these flags range from 1-9 (from best to worst). High quality data, considered suitable for fundamental scientific researches has flag value of 1-3. More details of the data quality analysis can be found in Foken et al. (2004, 2012).

Besides flux calculation and assign data quality flag, TK2 can also generate short-term averages and covariances of each variable. In case of limited storage capacity, these short-term statistics may become more desirable to be stored than the raw data. Statistics at longer period of variables a and b can be reconstructed

from these short-term information by (Foken, 2008b)

$$\overline{a'b'} = \frac{1}{M-1}\left[(U-1)\sum_{j=1}^{N}\left(\overline{a'b'}\right)_j + U\sum_{j=1}^{N}\overline{a}_j\,\overline{b}_j - \frac{U^2}{M-1}\sum_{j=1}^{N}\overline{a}_j\sum_{j=1}^{N}\overline{b}_j\right], \quad (2.18)$$

where $\overline{a'b'}$ is a long-term covariance of a and b. M is number of measurement points of the long-term time series. This long-term time series consists of N short-term time series, whose number of measurement points is U. $\left(\overline{a'b'}\right)_j$ is a short-term covariance of a and b. $\overline{a}_j$ and $\overline{b}_j$ are short-term averages of a and b respectively. These short-term averages are derived from raw data, which none of flux corrections have been applied. Therefore, any needed flux corrections must be included, when using these short-term statistics for flux calculations.

2.4 Coordinate rotation

There are two coordinate rotation schemes available in TK2, which are the double rotation (Kaimal and Finnigan, 1994) and the planar-fit rotation. The double rotation set the mean vertical velocity of each individual period to zero ($\overline{w} = 0$). It is easy to implement and very effective in a homogeneous flow. However, over the complex terrain or long-term measurement, the double rotation may loose information that contain in the non zero mean vertical velocity and high-pass filter the data. The planar-fit rotation was introduced to overcome this disadvantage (Paw U et al., 2000; Wilczak et al., 2001).

The planar-fit rotation needs a long-term data set to define a mean streamline. The rotation angle is determined from multiple linear regression on many shorter periods within the long-term data set. The planar-fit rotation set the long term mean vertical velocity to zero ($\langle\overline{w}\rangle = 0$), while the mean vertical velocity ($\overline{w}$) of each shorter period is not necessary to be zero. Since the LITFASS experiment was performed over a complex terrain and lasted for a months, therefore, the planar-fit rotation would be more suitable.

2.5 Wavelet analysis

Wavelet analysis is a very useful mathematical tool for processing nonstationary signals. In the Fourier analysis, a signal is decomposed into sinusoidal basis functions at various frequencies. Therefore, it reveals how much of each frequency contains

in a signal, but it is impossible to tell simultaneously when (or where) each specific frequency appear in a signal. In the wavelet analysis, a signal is decomposed into basis functions called 'wavelets', which are obtained by scaling (dilate or compress) and translating (shift location) the mother wavelet (shape of basis functions). Hence, other than the frequency content, the wavelet analysis can also reveal when each frequency appear in a signal.

Suppose there is a discrete time series x_n with equal timestep δt and $n = 0, 1, ..., N-1$. A continuous wavelet transform of this time series is the convolution of x_n with the wavelet function,

$$W_x(a,b) = \sum_{n=0}^{N-1} x_n \, \psi^*_{a,b}(n), \tag{2.19}$$

where $\psi^*_{a,b}(n)$ is a complex conjugate of the wavelet function $\psi_{a,b}$, which is characterised by the type of a mother wavelet, a scale or dilation parameter a, and a translation parameter b. This wavelet transforms gives the wavelet spectrum as

$$E_x = \frac{\delta t}{N C_\delta} \sum_{n=0}^{N-1} \left| W_x(a,b) \right|^2, \tag{2.20}$$

and wavelet cross-spectrum as

$$E_{xy} = \frac{\delta t}{N C_\delta} \sum_{n=0}^{N-1} W_x(a,b) W^*_y(a,b), \tag{2.21}$$

where C_δ is a reconstruction factor and equal to 0.776 for the Morlet wavelet.

In this thesis, the wavelet analysis was used to analyse data in both time and spatial averages. Also the Morlet wavelet was chosen to be a mother wavelet because it is suitable for the atmospheric analysis. The calculation routines is similar to Mauder et al. (2007b), which is based on the algorithm provided by Torrence and Compo (1998) (also available online at http://paos.colorado.edu/research/wavelets/). To apply this routine, the investigated data set must be gap filled. The embedded gap filling routine is done by duplicating the previous available data point in the time series. When the gap is very large, this gap filling routine can create unrealistic scales in the wavelet analysis. Therefore, gap in the investigated time series must be as minimized as possible.

2.6 Backward Lagrangian footprint model

The footprint is a transfer function between an observation and a source of signal, which for any measurements, it defines the field of view of the sensor (Rannik et al., 2012; Schmid, 2002; Vesala et al., 2008). The footprint of the measurement also defines the source area, which is an area that contribute to the measurement and mainly upwind of the sensor. Each element in the source area contributes to the sensors differently, as described by the footprint function or source weight function.

In this thesis, the footprint analysis was applied to the data from the aircraft and the MOL tower (MOL, 'Meteorological Observatory Lindenberg', see more details in chapter 3), which were collected at around 50 - 100 m height. In order to fit with the high measurement and non-homogeneous flow field, the backward Lagrangian dispersion model (LPDM-B) in Kljun et al. (2002) was chosen for the footprint analysis.

The LPDM-B is categorized as the Lagrangian stochastic (LS) model (Wilson and Sawford, 1996), in which particle's trajectories are governed by the random velocity field and can be traced either backward or forward in time. One advantage of the LS model is that it can analyse both Gaussian and non-Gaussian turbulence. According to Flesch (1996), a backward LS model can be used to estimate the fluxes caused by a known source area.

For the LPDM-B, set of particles are release from the sensor and traced backward in time until the particles touch the ground. During their journey, they can reflect at the top of ABL (z_i) and at the reflection height (z_r). In this case, multiple touchdowns are allowed. Although the LPDM-B is constructed from a horizontally homogeneous probability density function, it is potentially effective over inhomogeneous terrain. This model covers wide stability range and valid for any receptor heights (measurement heights) throughout the entire boundary layer. This means the LPDM-B is suitable with an observation at large measurement height, such as aircraft and high-tower measurements, which particles encounter cross similarity scaling domains. Furthermore, the LPDM-B also shows a good agreement with a forward LS model and a Lagrangian trajectory model embedded in a LES framework (Markkanen et al., 2009).

To operate the LPDM-B, these following parameters are required, a roughness length (z_0), a friction velocity (u_*), an Obukhov length (L), a Deardorff velocity (w_*), a boundary layer height (z_i) and a reflection height (z_r). In this thesis, the value of the displacement height was used as z_r. The estimation of these input parameters is presented in chapter 3. With these input parameters, the LPDM-

B creates touchdown catalog (or table), which contains (1) touchdown locations relative to the sensor (x, y), (2) initial velocities (w_{i0}) calculated when each particle is released and (3) touchdown velocities (w_{ij}) calculated when each particle reaches the ground.

Information in a touchdown catalog can be used to estimate the mean concentration and mean flux at the sensor as

$$c_s(x, y, z) = \frac{2}{N} \sum_{i=1}^{N} \sum_{j=1}^{n_i} \frac{1}{w_{ij}} Q(X_{ij}, Y_{ij}, z_0) \tag{2.22}$$

$$F_s(x, y, z) = \frac{2}{N} \sum_{i=1}^{N} \sum_{j=1}^{n_i} \frac{w_{i0}}{w_{ij}} Q(X_{ij}, Y_{ij}, z_0) \tag{2.23}$$

where N is the number of released particles and n_i is the number of touchdown and Q is the source strength at each touchdown location.

3

Data

Many data sets of the LITFASS-2003 experiment were used through-out this thesis in both time and spatial averages parts. Therefore, this chapter will describe the steps taken in data collection and data processing.

3.1 Experimental overview

The LITFASS-2003 experiment was conducted during 19 May 2003 - 18 June 2003 near the Meteorological Observatory Lindenberg (MOL), which is located in the local time zone of UTC+1 (Fig. 3.1). This experiment covered a large heterogenous landscape with an area of 20×20 km^2, which was comprised of these following land uses: grass, maize, rape, cereals (include rye, barley and triticale), lake, pine forest and settlement (or village). The agricultural area was mostly in the eastern part, while the western part was dominated by pine forest. The land use map of this area is available at a resolution of 100 m.

There were a few significant precipitation events during the experimental period. The two heaviest ones were observed on 5 June (1-45 mm) and 8 June (8-20 mm). The former mainly affected the southern part of the LITFASS area, while the latter distributed evenly throughout the area.

There were many measurements available during the campaign, such as EC tower measurements and aircraft measurements, which covered all important land uses of this area. The related measurements are described briefly in this chapter. Full information of the LITFASS-2003 experiment can be found in Beyrich and Mengelkamp (2006) and Beyrich et al. (2004).

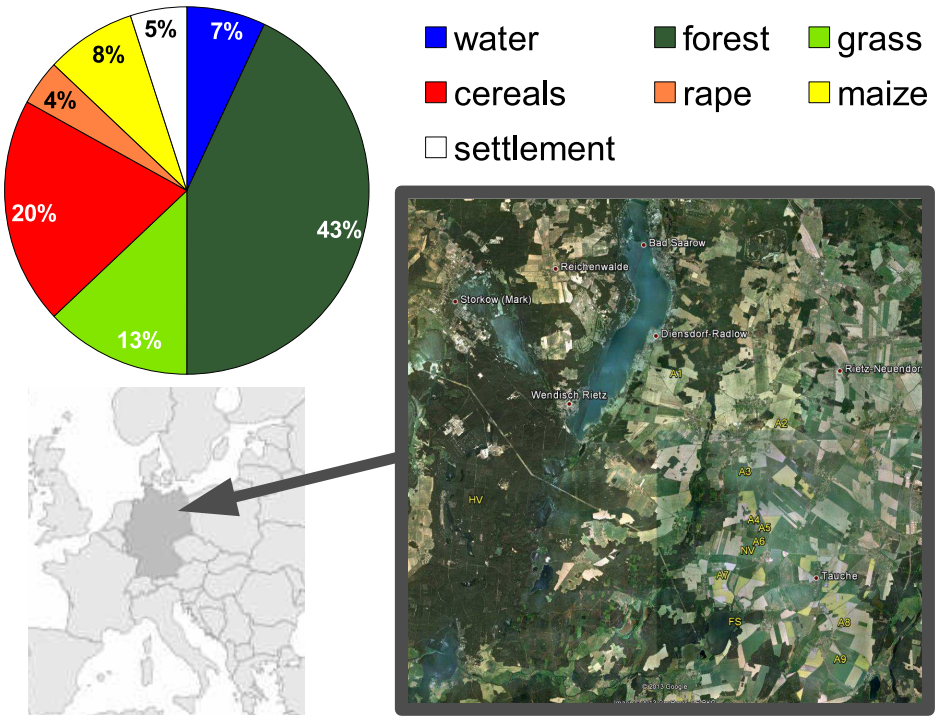

Figure 3.1: Map and land use of the LITFASS area. The land use fractions were obtained in 2003, while the map represent the terrain in 2013 (maps were generated by Google Earth and Google map chart).

3.2 Eddy-covariance tower measurements

3.2.1 Measuring stations

There were 16 EC systems installed on multiple towers during the LITFASS-2003 experiment. All of them were operated individually as a single-point measurement, in which the representative statistics are the time average statistics. Each EC system or a turbulence complex consisted of a sonic anemometer and a hygrometer, which could measure wind velocity, temperature and moisture. This measurement allowed estimations of the sensible and latent heat fluxes by the EC technique. An estimation of the CO_2 flux was also possible, if the hygrometer could measure the CO_2 concentration.

Fourteen EC systems were installed on small towers, each of which was part of a micrometeorological measuring station. These stations were operated as ground-based measuring stations on 13 sites. They were mostly scattered over the agricultural fields on the eastern part of the LITFASS area. Two stations, NV2 and NV4, were installed on the same grassland, but they were oriented to different wind

sectors. In this thesis, results from these two stations were combined and reported as one station NV. The other two EC systems were installed on the MOL tower at 50 m and 90 m height, which was a few meters away from NV2 and NV4. Instead of keeping high frequency raw data, all measuring stations kept short-term statistics at every 5 or 10 minutes. The long-term statistics can be calculated from these short-term statistics with Eq. 2.18. A brief summary with information about all measuring stations used in this thesis is shown in Table 3.1.

To measure all energy balance components in Eq. 1.1, the net radiation and ground heat flux were also measured in all 14 ground-based stations. For the net radiation measurement, four components net radiometers were installed to measure both down-welling and up-welling components of the shortwave and longwave radiations. Therefore, the net radiation could be estimated from

$$Q^* = K\uparrow + K\downarrow + I\uparrow + I\downarrow \tag{3.1}$$

where $K\uparrow$, $K\downarrow$, $I\uparrow$ and $I\downarrow$ are the shortwave up-welling radiation, shortwave down-welling radiation, longwave up-welling radiation and longwave down-welling radiation respectively.

For the ground heat flux over the terrain, the following quantities were measured at different depths; soil humidity, soil temperature and soil heat flux. Using these parameters, there are two different ways to estimate the soil heat flux at a specific depth. The first approach is by a direct measurement with the heat flux plate. This approach is known as the PlateCal approach. The second approach, the GradCal approach, uses the vertical temperature gradient to determine the soil heat flux at a specific depth. More details of these two approaches can be found in Liebethal et al. (2005). Once the soil heat flux at a specific depth was known, it was extrapolated up to the surface by using the change in heat storage of the soil (calorimetry). It must be noted that the soil humidity measurement of the A5 (rye) station was mostly not available, because of the defective sensor. Since this station was just around 100 m away from the A6 (maize) station, the soil humidity measurement of the A6 station was used to determined the ground heat fluxes of the A5 station.

Due to the high heat capacity of water, the whole lake (FS) could be approximated as a big heat reservoir. Therefore, the heat released or consumed at the lake surface can be estimated from the change in heat storage of the lake. The ground heat flux of the lake was determined from the temperature profile of the lake by assuming well-mixed conditions in a shallow lake (Nordbo et al., 2011).

Table 3.1: Brief information of EC stations in the LITFASS-2003 experiment during 20 May 2003 12:00 UTC - 18 June 2003 00:00 UTC. Notations: Sta = Station, Op = Operator, z_m = measurement height, θ = undisturbed wind sectors (clockwise), h_c = canopy height, h_0 = elevation or height above sea level [m], Res = mean residual between 10:00 - 12:00 UTC, which is also reported as a percentage to the available energy ($Res/(-Q^* - Q_G)$). Full details can be found in Beyrich and Mengelkamp (2006) and Mauder et al. (2006).

Sta	Surface	Op[1]	Turbulence sensors	z_m (m)	θ (deg)	h_c (m)	h_0 (m)	Latitude (deg)	Longitude (deg)	Res(%)
A1	Rye	TUDD	USA-1/KH20	3.55	90-300	0.95-1.55	69	52° 13′ 39″	14° 04′ 29″	-
A2	Rape	TUDD	CSAT3/KH20	3.6	90-330	1.1-1.25	93	52° 12′ 34″	14° 08′ 18″	-
A3	Barley	GKSS	CSAT3/KH20	3.25	90-270	0.6-0.7	86	52° 11′ 31″	14° 06′ 59″	109 (26%)
A4	Maize	GKSS	CSAT3/KH20	3.25	90-270	0.05-0.75	75	52° 10′ 28″	14° 07′ 18″	115 (29%)
A5	Rye	UBT	USA-1/KH20	2.8	60-30	0.9-1.50	73	52° 10′ 09″	14° 07′ 28″	147 (31%)
A6	Maize	UBT	CSAT3/LI7500	2.7	90-270	0.1-0.6	73	52° 10′ 00″	14° 07′ 29″	117 (30%)
A7	Rape	GKSS	CSAT3/KH20	3.4	30-240	0.7-0.9	67	52° 09′ 16″	14° 06′ 10″	52 (13%)
A8	Triticale	WAU	CSAT3/LI7500	3.55	30-210	0.8-1.1	52	52° 08′ 14″	14° 10′ 36″	110 (23%)
A9	Rape	WAU	CSAT3/LI7500	3.5	60-210	1-1.2	48	52° 07′ 26″	14° 10′ 27″	107 (23%)
NV2	Grass	DWD	USA-1/LI7500	2.4	60-180	0.05-0.20	73	52° 09′ 57″	14° 07′ 20″	67 (19%)
NV4	Grass	DWD	USA-1/LI7500	2.4	150-330	0.05-0.20	73	52° 09′ 57″	14° 07′ 20″	85 (24%)
FS	Lake	DWD	USA-1/LI7500	3.85	180-30	0	43	52° 08′ 15″	14° 06′ 37″	245 (63%)
HV	Pine forest	DWD	USA-1/LI7500	30.5	30-330	14	49	52° 10′ 54″	13° 57′ 09″	126 (23%)
M50	Grass	DWD	USA-1/LI7500	50	90-300	0.05-0.20	73	52° 09′ 57″	14° 07′ 20″	-
M90	Grass	DWD	USA-1/LI7500	90	90-300	0.05-0.20	73	52° 09′ 57″	14° 07′ 20″	-

[1] DWD - German Meteorological Service; TUDD - University of Technology Dresden; GKSS - GKSS Research Centre Geesthacht; WAU - Wageningen University and Research Centre; UBT - University of Bayreuth

3.2.2 Canopy heat storage

All kinds of plants store energy in their canopies. This canopy heat storage has two main contributions from the plant material (or biomass) and the air between plants. As reported by Oncley et al. (2007), over low vegetation like a cotton field, both contributions of a canopy heat storage are relatively small and negligible. According to the study in maize and soybean (Meyers and Hollinger, 2004), the stored energy in biomass is significant when a canopy is fully developed, while Q_G is very low. During the LITFASS-2003 experiment, the maize field began from bare soil and grew up to approximately 0.5 m at the end of the experiment. Therefore, their stored energy in biomass can be neglected. However, a forest's canopy heat storage is significant (Lindroth et al., 2010) and need to be included in the energy budget equation (Eq. 1.1). Unfortunately, not all required biomass properties of the forest were collected during the LITFASS-2003 experiment and the forest's canopy heat storage could not be precisely estimated. Hence, all analyses of this site were conducted without a canopy heat storage term. Since a forest's canopy heat storage during the daytime would release back to the atmosphere during the nighttime, it is more important in the sub-diurnal scale (Haverd et al., 2007). Therefore, the omission of a forest's canopy heat storage would have minimal effect over a long-term basis.

3.2.3 Data selection for the ogive analysis and block ensemble average

There were two analyses in the time average part (Chapter 4), the ogive analysis and block ensemble average. Both of them were applied to data from EC towers as listed in Table 3.1. Most of the required data was available since 20 May 2003 12:00 UTC, so the period between 20 May 2003 12:00 UTC - 18 June 2003 00:00 UTC was chosen to be analyzed in this thesis. To ensure high data quality as well as to minimize the irrelevant factors, which might influence turbulent fluxes, different data selection criteria were applied to the data in both ogive analysis and block ensemble average parts separately.

For the ogive analysis, the averaging time was extended to up to 4 hours. This 4-hour period consisted of 8 consecutive subperiods (or blocks) of 30 minutes. The ogive analysis over any 4-hour periods was carried out only if all blocks satisfy the selection criteria. The first selection criterion is the same as that found in Mauder et al. (2006), which is that the sonic anemometers must not be disturbed either by the internal boundary layer due to the surface heterogeneity, or the flow distortion

caused by obstacles. The internal boundary layer height can be estimated from (Raabe, 1983)

$$z_m \leq \delta = 0.3\sqrt{x}, \tag{3.2}$$

where z_m is the measurement height, δ is the internal boundary layer height and x is the distance from the sensor to boundary of the next land use. To keep the measurement undisturbed, z_m must not exceed δ. Hence, any wind direction, whose corresponding x did not satisfy Eq. 3.2, were excluded from the investigation. The undisturbed wind sectors (θ), from both internal boundary layer and flow distortion, of each measuring station are listed in Table 3.1. Additionally, footprint climatology was used to confirm that the target land use has a significant contribution to the measurement. This contribution varied over the stability range. Any wind sectors whose contribution from target land use is less than 80%, were also excluded from the investigation.

The next data selection criterion involves a steady state condition of the time series, which is indicated by the steady state flag (section 2.3). Accepted high quality data have quality flag 1-3. In this thesis, the ogive analysis of the energy balance components (Q_H and Q_E) and CO_2 flux ($F_c = \overline{w'c'}_{CO_2}$) were considered separately. For the energy balance components, only the steady state flags of friction velocity (u_*), Q_H and Q_E were considered. The ogive analysis was applied to any periods only when all these three steady state flags qualified. For F_c, the ogive analysis was applied on any period only when the steady state flag of u_* and CO_2 qualified.

The transition period was avoided by excluding the time period covering one hour before to one hour after both sunrise and sunset from the ogive analysis. The threshold values of each turbulent flux was set as a minimum requirement for the analysis. For u_*, which indicates the level of turbulence (Massman and Lee, 2002), its threshold value is 0.1 ms^{-1}. This was set to rule out very small turbulent fluxes, which might result from instrumentation noise. This limit normally excludes periods with very weak wind as well. For Q_H, Q_E and F_c, their threshold values were formulated to avoid complication with their measurement errors. According to Mauder et al. (2006), based on 30-minute averaging time, the measurement errors of Q_H and Q_E are 10% - 20% of the turbulent flux at 30 minutes or 10 - 20 W m^{-2}, whichever is larger. For u_* and F_c, their measurement errors are 0.02-0.04 ms^{-1} and 0.5-1 μmol $m^{-2}s^{-1}$ respectively (Meek et al., 2005). Therefore, in this thesis, the threshold values of Q_H and Q_E were set to be 20 W m^{-2}, while the threshold value of F_c was set to be 1 μmol $m^{-2}s^{-1}$. Unusually large uncertainty of F_c during the night time was taken into account by using only data periods with u_* greater than

Table 3.2: Information about selected Helipod flight legs. Notations: $\overline{z}_m$ = average height above ground, $\overline{\theta}$ = average wind direction, z_i = boundary layer height

Properties	7 Jun 2003 13:40-13:50	14 Jun 2003 9:20-9:30
$\overline{z}_m$ (m)	85	88
Direction	North to South	Northwest to Southeast
Distance (km)	18.5	20.1
$\overline{\theta}$ (deg)	254	279
z_i (m)	1350	1800
Meteorological conditions	after heavy rain events	dry
Land use coverage	mainly farmland	mainly forest and farmland

0.25 ms^{-1} (Hollinger and Richardson, 2005).

Similar selection criteria could not apply in the block ensemble average approach, as it involved averaging times of several hours to days. Therefore, the quality control of this part was done by discarding any periods with more than 10% of missing raw data. This missing data could have resulted from various factors, such as electrical black out.

3.3 Aircraft measurements

The aircraft measurements in the LITFASS-2003 experiment were done by the Helipod. The Helipod is a turbulence measurement system, which attaches below a helicopter by a 15 m rope. It collected data at 100 Hz, while the helicopter was moving at a speed of 40 ms^{-1}. This speed is much faster than the wind speed and the sampling rate is fast enough to sample the data within the evolution time scale of eddies. The Helipod is outside the down-wash area of the helicopter, which creates a smaller disturbance than a conventional research aircraft. During the LITFASS-2003 experiment, there were 27 flights over 16 days. More details of the Helipod measurements can be found in Bange and Roth (1999) and Bange et al. (2002).

Two selected flights legs on 7 and 14 June 2003 were used in the spatial average part. Brief information of each flight leg are presented in Table 3.2, while the outline of the flight paths are presented in chapter 5. According to Lenschow and Stankov (1986) and Lenschow et al. (1994), to measure flux with a good accuracy, the flight distance must be as large as possible. Distances of these two selected

flights were greater than $10z_i$, which meet the suggestion in Lenschow and Stankov (1986). The integral time scale of these two flights, which is used to estimate flux uncertainty, could be properly calculated without any approximation as well (Bange et al., 2006a).

The instantaneous fluxes along the flight path of both flights were calculated by a moving average approach. By varying the window size from 500 m to 10 km, 10% uncertainty of the entire flight's flux, in both Q_H and Q_E have been reached at the window size of 2 km for both selected flights. Therefore, a window size of 3 km was used for a comparison purposes through-out this thesis.

3.4 Scintillometer

A large aperture scintillometer (LAS) can be used to determine the sensible heat flux by measuring the structure parameter of the refractive index. It is operated at a near-infrared wavelength and suitable for estimating the sensible heat flux over path lengths of several kilometers. In 2003, there were three LASs installed over the LITFASS area.

In this thesis, the surface sensible heat flux, which was measured by the LAS over the farmland, was compared with the spatial average flux measured by the Helipod as well as surface fluxes estimated from the footprint model. This LAS had a transmitter installed on the MOL tower, while the receiver was at the observatory in Lindenberg. The outline of this LAS path is presented along with the selected Helipod flight paths in chapter 5. The effective beam was 43 m in height and covered the path length of 4.7 km. More technical and theoretical details of this LAS can be found in Meijninger et al. (2006) and the references thereafter.

3.5 Boundary layer height

Boundary layer height (z_i) or mixed layer height is the height at which the surface forcings are no longer in effect. For this thesis, it was an input parameter of the LPDM-B footprint model (section 2.6) and was used as an initial point of surface flux extrapolation. There are two basic approaches to determine z_i nowadays , which are an estimation from profile data and parameterizations by a model. Details of most available methods in the literature can be found in Seibert et al. (2000).

For the LITFASS area, z_i is estimated from the high-resolution vertical profiles of temperature, humidity and wind, which are obtained from the operational ra-

diosoundings. In this area, the operational radiosoundings are routinely released four times a day at the MOL (WMO station code 10393). Full details of z_i estimations at this station can be found in Beyrich and Leps (2012).

Each radiosonde, which is released at 00:00, 06:00, 12:00 and 18:00 UTC daily, collects the data at every 5 second and rises up at about 5 ms^{-1}. There are different criteria for estimating z_i, however, the one evaluated from the Richardson number is selected to be a standard output. The bulk Richardson number (Ri) is defined as

$$Ri(z) = (z - h_0)\,\frac{(g/\theta_0)\,(\theta(z) - \theta_0)}{U^2(z)}, \tag{3.3}$$

where z is the height above ground, $g = 9.80$ ms^{-2} is the gravitational acceleration, U is wind speed and h_0 is the elevation of the released site, which is 112 m above sea level for the MOL. z_i is then determined from the first level where Ri exceed 0.2.

There are many reasons to choose the Richardson number approach as a standard output. Firstly, it considers both thermal and mechanical effects of the turbulence. Secondly, it provides a consistent data set, and finally, it is consistent with the value from operational Numerical Weather Prediction (NWP) model output.

Other than the Richardson number approach, the MOL also estimates z_i from many different criteria, such as the level of maximum potential temperature gradient, the level of maximum humidity gradient and from a parcel method. In an ideal atmosphere, z_i from all criteria are not much different. Therefore, the deviation of z_i from all criteria are used to estimate the measurement uncertainty and assign a quality flag.

3.6 Roughness length and displacement height

The roughness length (z_0) and displacement height (d) are also input parameters of the LPDM-B. For an individual ground-based tower, the calculations of these two parameters were adapted from Martano (2000). The first step was to select 30-minute runs with neutral stratification ($|z/L| \leq 0.05$). All these runs must be during the daytime, had acceptable wind direction as listed in Table 3.1, and had Q_H and Q_E larger than 20 Wm^{-2}. For the neutral stratification, the wind speed has a logarithmic profile as

$$U(z) = \frac{u_*}{k_v} \ln\left(\frac{z - d}{z_0}\right), \tag{3.4}$$

where U is wind speed, z is a height above ground, u_* is the friction velocity and $k_v = 0.4$ is von Karman constant. Next was to take u_* from the measurement and assign the initial values of z_0 and d to be $0.1h_c$ and $2h_c/3$ respectively (h_c is a canopy height). Subsequently z_0 and d were varied iteratively until the different between $U(z)$ and the measured wind speed reached its minimum. The values of z_0 and d were taken at this minimum. Finally, a daily average was made to estimate z_0 and d for each day.

3.7 Composite fluxes

For each land use in the LITFASS area, their representative fluxes or composite fluxes of each 30-minute period were aggregated from turbulent fluxes with accepted quality flags of all ground-based measurements. Detailed formulations can be found in Beyrich et al. (2006). In principle, all ground-based stations were grouped according to their land uses such as grass (NV2 and NV4), maize (A4 and A6), rape (A2, A7 and A9), cereals (A1, A3, A5 and A8), lake (FS) and forest (HV).

For the land use with one measuring station, like lake and forest, the composite fluxes were taken from measured turbulent fluxes, which had accepted quality flags and covered undisturbed wind sectors. For the grassland, where two measuring stations were installed on the same field and each station was oriented to different wind sectors, the composite fluxes were taken from the station with undisturbed wind sector (Table 3.1). For example, if the wind direction at one 30-minute period is 150 degree, the composite fluxes of the grassland of this period are the fluxes measured by NV2 station.

For maize, rape and cereals, where two or more measuring stations were installed on different fields, the formulation of composite fluxes was more complicated. The 30-minute fluxes of all stations needed to be normalized before averaging together as composite fluxes. For each land use, the normalization factor of each station was determined from a linear regression over the time period, when data from all stations in each group was available with good quality. For example, in case of the composite flux of latent heat of cereals, all period with good quality latent heat fluxes of A1, A3, A5 and A8 were selected. The linear regression lines of each station were formed over these data. The normalization factors of each station were determined from the value from these regression lines. On 29 May 2003, the value from these regression lines of A1, A3, A5 and A8 were 1.1, 0.75, 1.3 and 0.9 respectively. Hence, their normalization factor of latent heat flux of each station on this day are 0.9 (=1/1.1),

1.33 (=1/0.75), 0.75 (=1/1.3) and 1.1 (=1/0.9) respectively. Once normalized, the average value of normalized latent heat fluxes was taken as a composite flux. The composite fluxes of grass, maize, rape and cereals were combined together as composite fluxes of the farmland. This farmland composite fluxes were combined with composite fluxes of lake and forest to form the composite fluxes or area-averaged fluxes of a whole LITFASS area.

With this composite flux formation process, the composite flux of all energy balance components was created. In this thesis, the same principle was also applied to estimate the composite quantity of u_*, z_0 and d as well. All these composite fluxes were used with the footprint analysis in the spatial average part.

4

Time average

In normal practice, the averaging time for an EC tower measurement is 30 minutes. However, this typical averaging time seems to be too short to measure contribution from SC, which is relatively stationary. Therefore, the averaging time extension beyond 30 minutes is suggested to increase the possibility that slow moving SC can move pass the sensor.

In this chapter, the averaging time extension was studied with two approaches, the ogive analysis and the block ensemble average. Both of them were applied on data from all EC towers of the LITFASS-2003 experiment. Part of the results from this chapter has been submitted to a research journal (Charuchittipan et al., 2013, see Appendix A).

4.1 Theoretical background

Suppose there is a time series of variable $a(t)$, which is measured by a fixed-tower measurement. Its suggestive statistics within a period P are the time-averaged statistics (section 2.1.1), which can be used in the conservation equations as long as they satisfy the Reynolds averaging rules (section 2.2). To satisfy these rules, homogeneous and steady state conditions are imposed to keep the ergodic condition valid.

The appropriate study site can make the homogeneous condition to be accomplished, while the restriction of the averaging time can fulfill the steady state condition. Since the fixed-tower cannot move anywhere during the measurement, it would be safe to assume that the homogeneous condition always holds. Therefore, the choice of averaging time P is very important. It must be long enough to capture most of the atmospheric turbulence, yet it must not violate the steady state

condition. The typical value of P for the EC measurement is 30 minutes. In this period P a variable $a(t)$ is decomposed with the Reynolds decomposition (Eq. 2.9) into mean part ($\overline{a}$) and fluctuation part (or turbulence term $a'(t)$) as

$$a(t) = \overline{a} + a'(t). \tag{4.1}$$

When apply this decomposition to the product of vertical velocity w and variable c, which can be a horizontal wind velocity or a scalar quantity, it gives the expression of the mean vertical transport (or flux) of a momentum or a scalar quantity as

$$\overline{w(t)c(t)} = \overline{w}\,\overline{c} + \overline{w'c'} \tag{4.2}$$

This expression can be further simplified by the coordinate rotations (section 2.4), which set $\overline{w}$ to zero. Thus this vertical transport solely depends on the turbulence motion.

It must be very careful when the averaging time is extended beyond 30 minutes. If the time averaged statistics are still a desirable representative statistics, the steady state condition is required, which may restrict the time extension up to a few hours. However, if the much longer averaging time than a few hours is a must, the new representative statistic must be considered.

4.1.1 Modified ogive analysis

The ogive analysis was introduced by Desjardins et al. (1989) and Oncley et al. (1990) for investigating the flux contribution from each frequency range and determining the suitable averaging periods that can capture most of the turbulent fluxes. The ogive function of the turbulent flux ($og_{w,c}$) is defined as the cumulative integral of the cospectrum of the turbulent flux ($Co_{w,c}$) starting with the highest frequency.

$$og_{w,c}(f_0) = \int_{\infty}^{f_0} Co_{w,c}(f)df, \tag{4.3}$$

where w is the vertical wind velocity, c is a horizontal wind velocity or a scalar quantity like temperature and humidity, and f is a frequency, which corresponds to a time period (τ) as

$$\tau = \frac{1}{f}. \tag{4.4}$$

This analysis was once applied to data measured over the maize field (A6) of the LITFASS-2003 experiment in Foken et al. (2006), where the ogive function was

calculated from the raw 20 Hz data over 4-hour period and mainly focused on 3 selected days (7-9 June 2003). This article shows that the ogive curves can be classified into three cases. Case 1, where the ogive curve exhibits the asymptotic behavior toward the low frequency within 30-minute period. This indicates that the 30-minute averaging time is sufficient to capture most of the turbulent fluxes. Case 2, in which the ogive curve shows the extreme value (peak) within 30-minute period, this means the total turbulent fluxes has been reached before 30 minutes. Hence the longer averaging time obviously reduce the flux and the period shorter than 30 minutes would be enough to capture most of the turbulent fluxes. Case 3, in which the ogive curve does not converge within 30-minute period. This implies that there is a significant contribution from the low frequency part of the turbulent spectrum and 30-minute averaging time is not enough to capture most of the fluxes.

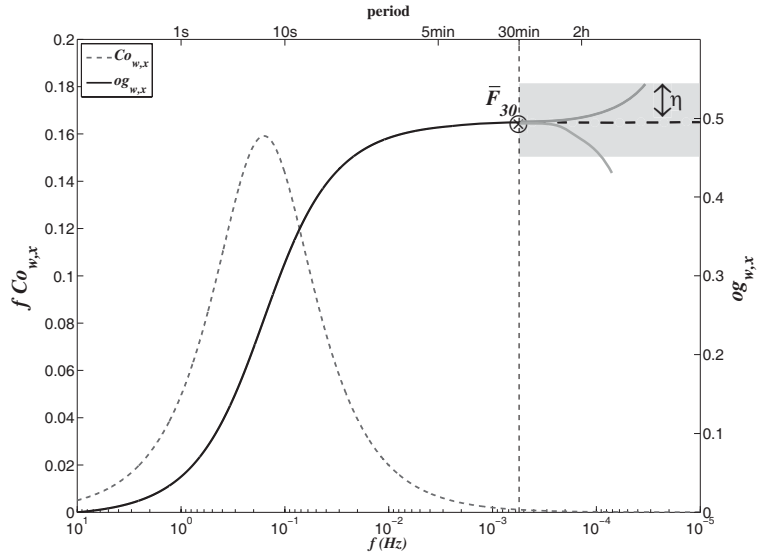

Figure 4.1: The short term average time series can estimate the turbulent flux at a 30-minute period ($\overline{F}_{30}$) and its evolution after that (gray solid lines in a gray band). The error band of width 2η (gray band) was defined for identifying the ogive case. See Table 4.1 for ogive case definition.

To apply the ogive analysis to data from all EC towers of the LITFASS-2003 experiment, the raw high-frequency data are required. Nevertheless, this type of data is not available in all EC towers. Only the short-term statistics at every 5 or 10 minutes exists for all sites, in which turbulent fluxes at a longer period can be estimated with Eq. 2.18. In this thesis, the modified ogive analysis (MOG) was developed to deal with this short-term statistics data. According to the spectral analysis, the spectra calculated from high and low frequency data behave similarly in the low frequency region (Kaimal et al., 1972). Hence, the turbulent spectra calculated from the short-term statistics data can be used to estimate the change in

the turbulent fluxes after 30 minutes without any information prior to 30 minutes.

The turbulent cospectra of the short-term average statistics were calculated with a standard Fast Fourier Transform (FFT) method. To avoid influences from the diurnal effect, the time extension was kept up to 4 hours as in Foken et al. (2006). The turbulent fluxes change after 30 minutes were determined from the cumulative integral of the cospectra starting from the frequency, which corresponds to a period of 30 minutes. Then its maximum value was set to be the maximum flux difference (Δ_{max}),

$$\Delta_{max} = \max\left(\int_{\tau=30}^{\tau} Co_{w,c}(f)df\right). \tag{4.5}$$

The ogive curves classification was done by comparing Δ_{max} with the turbulent flux at 30 minutes ($\overline{F}_{30}$). $\overline{F}_{30}$ could be estimated in two different ways. The first approach, time averaged fluxes of each 30-minute block $(\overline{w'c'})_j$ were averaged together as

$$\overline{F}_{30} = \frac{1}{8}\sum_{j=1}^{8}(\overline{w'c'})_j\,. \tag{4.6}$$

The second approach, $\overline{F}_{30}$ was determined from the difference between a total flux over 4-hour period ($\overline{F}_{4hr}$) and the turbulent flux after 30-minute period ($F_{\tau>30}$),

$$\overline{F}_{30} = \overline{F}_{4hrs} - F_{\tau>30}. \tag{4.7}$$

$\overline{F}_{4hr}$ was calculated from short term average data with the help of Eq. 2.18, while $F_{\tau>30}$ was calculated from the cumulative integral of the cospectra from the lowest frequency (f_{min}) to the frequency corresponding to 30-minute period,

$$F_{\tau>30} = \int_{f_{min}}^{\tau=30} Co_{w,c}(f)df. \tag{4.8}$$

Both estimations in Eq. 4.6 and Eq. 4.7 gave quite compatible $\overline{F}_{30}$. The error bar of width 2η was then set around the turbulent flux at 30-minute period (Fig. 4.1). If Δ_{max} was still confined in this band, it indicated that the turbulent flux difference after 30 minutes was not significant, which conformed to case 1 in Foken et al. (2006). If Δ_{max} exceeded this band, this meant the turbulent flux difference was significant and could be classified into 2 cases depending on the change of turbulent fluxes after 30-minute period. It was equivalent to case 2 in Foken et al. (2006), when the size of turbulent fluxes decreased; and case 3, when the size of turbulent fluxes increased. The size of an error band η was set to be 10% (or 20%) of the turbulent flux at

30-minute period, which must not be smaller than the measurement errors of each turbulent flux (section 3.2.3). The ogive case definition in analogy to Foken et al. (2006) is shown in Table 4.1.

Table 4.1: Ogive case definition in analogy to Foken et al. (2006). Δ_{max} is a maximum flux difference after 30-minute averaging time. $\overline{F}_{30}$ is the turbulent flux at 30-minute period. η is the width of an error band.

Case	Criterion
1	$\Delta_{max}/\overline{F}_{30} \leq \eta$
2	$\Delta_{max}/\overline{F}_{30} > \eta$ and $\Delta_{max} < 0$
3	$\Delta_{max}/\overline{F}_{30} > \eta$ and $\Delta_{max} > 0$

In this thesis, the MOG was applied to all listed stations in Table 3.1, except A1 and A2, because their data were not always available. The period of investigation also covers the entire period of the LITFASS-2003 experiment (section 3.2.3). For the energy balance component, the MOG was applied to all listed sites. For the CO_2 flux, the MOG was only applied to the sites with the LI-7500 hygrometer, except the lake which has very low concentration of CO_2. Note that none of flux corrections were applied in the MOG. Since each point of the cospectra corresponds the turbulent flux at different duration, the choice of suitable duration for the flux corrections would be ambiguous. According to Mauder and Foken (2006), flux corrections would reduce the residual by 17%. Therefore, this reduction might be assumed to reflect in the increasing of Q_H and Q_E.

4.1.2 Block ensemble average

In the ogive analysis, to keep the steady state condition valid, the time extension is restricted to a few hours. If these few hours are not enough to include the contribution from SC, the averaging time may need to be extended further. When the averaging time is much longer than a few hours, it is very difficult to maintain the steady state condition. Without a steady state condition, the time-averaged statistics no longer satisfy the Reynolds averaging rules and are not representative statistics.

Bernstein (1966, 1970) and Finnigan et al. (2003) proposed using the block ensemble average, as it always obeys the Reynolds averaging rules. This allows the formulation to be carried out without a steady state condition. Suppose that a time series $a(t)$ spans over a long-period NP, which consists of N consecutive blocks (or

subperiods or runs) of period P. Let a subscript n represents the n^{th} block, whose time average of $a_n(t)$ in this block is $\overline{a}_n(t)$. This time average becomes a function of time, because it can vary from block to block. The block ensemble average of all N blocks (denoted by $\langle\rangle$) of $a_n(t)$ over period NP is

$$\langle\overline{a}\rangle = \frac{1}{N}\sum_{n=1}^{N}\overline{a}_n(t), \tag{4.9}$$

which is equivalent to the time average of $a(t)$ over a period NP and always constant over this period. The time average of each block $\overline{a}_n(t)$ deviates from $\langle\overline{a}\rangle$ by $\tilde{a}_n(t)$,

$$\tilde{a}_n(t) = \overline{a}_n(t) - \langle\overline{a}\rangle\,. \tag{4.10}$$

Hence the Reynolds decomposition can be replaced by the triple decomposition (Fig. 4.2), which in the n^{th} block, a variable $a_n(t)$ can be separated into three parts as

$$a_n(t) = \langle\overline{a}\rangle + \tilde{a}_n(t) + a'(t). \tag{4.11}$$

As in the Reynolds decomposition, the first and the last terms are the mean term and turbulent term (instantaneous fluctuation), respectively. The second term or a mesoscale term is the block to block fluctuations, which represent the mesoscale motion caused by eddies at scale larger than P but smaller than NP [1]. This triple decomposition leads to the block ensemble average of the vertical transport of momentum or scalar over N blocks of period P as (dropping the subscript n and omitting t)

$$\left\langle\overline{w(t)c(t)}\right\rangle = \langle\overline{wc}\rangle = \langle\overline{w}\rangle\,\langle\overline{c}\rangle + \langle\tilde{w}\tilde{c}\rangle + \left\langle\overline{w'c'}\right\rangle \tag{4.12}$$

This shows that the mean vertical flux averaged over a period NP, there is not only a contribution from the usual turbulent flux $\overline{w'c'}$, but also a contribution from the mesoscale flux $\tilde{w}\tilde{c}$. Note that the block ensemble average can be obtained either with the non-overlapped block average as in Finnigan et al. (2003) or overlapped block average (or moving average) as in Bernstein (1966).

To use the block ensemble average, every single block in period NP must be in the same coordinate system, the long term coordinate. It has been shown in Finnigan et al. (2003) that a period to period rotation, like the double rotation (Kaimal and

[1] The word 'mesoscale' is used in many literatures, e.g. Nakamura and Mahrt (2006). However, in the ASL, eddies that are actually related to this term may not meet the size of what really mean mesoscale in meteorology.

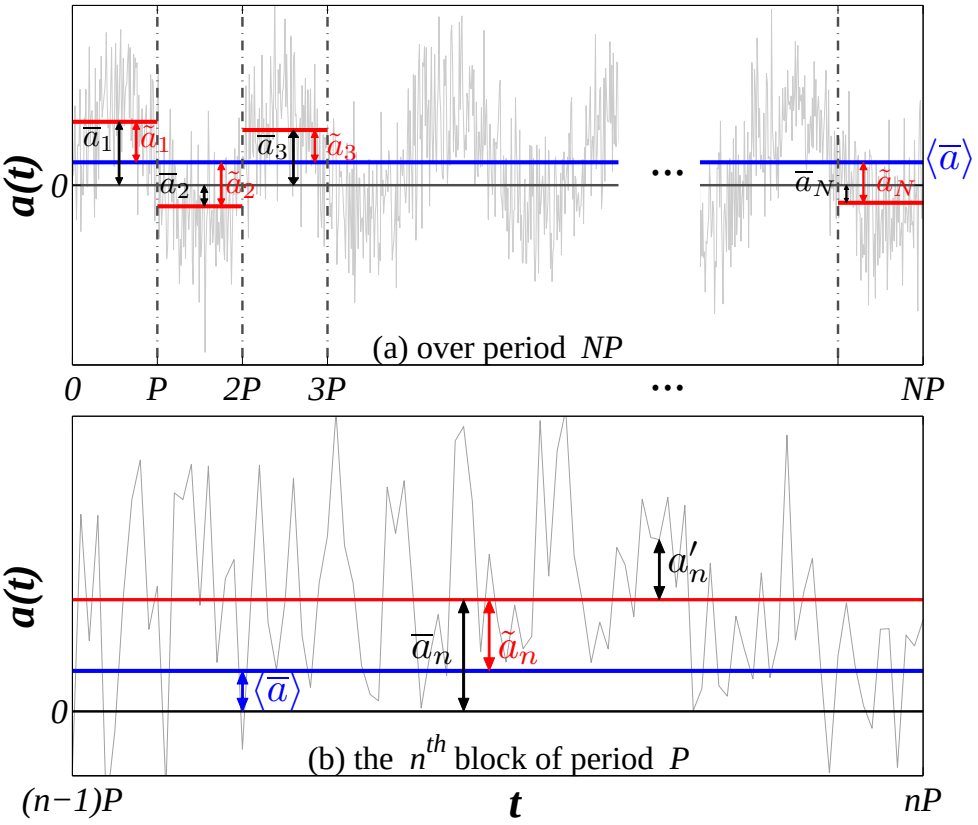

Figure 4.2: The block ensemble average and triple decomposition of $a(t)$. (a) Over a long period NP, the block ensemble average $\langle\overline{a}\rangle$ is constant, while the time average of an individual block $\overline{a}_n$ is not constant and deviates from the block ensemble average by $\tilde{a}_n$. (b) At any point in the n^{th} block, $a(t)$ can be decomposed with a triple decomposition (Eq. 4.11).

Finnigan, 1994), is not a long term coordinate. It sets $\overline{w}$ of each n^{th} period to zero and acts as a high-pass filter. In this thesis, the long term coordinate was obtained with the planar fit rotation (section 2.4), which determines the rotation angle from multiple periods. This rotation set the block ensemble average of vertical velocity of the period NP to zero ($\langle\overline{w}\rangle = 0$), while the mean vertical velocity in each period P is not necessary zero. Thus the block ensemble average of the vertical flux becomes

$$\langle\overline{wc}\rangle = \langle\tilde{w}\tilde{c}\rangle + \langle\overline{w'c'}\rangle \tag{4.13}$$

According to Finnigan et al. (2003), the mesoscale flux $\tilde{w}\tilde{c}$ has two roles, which are

1. To balance the unsteady horizontal flux divergence and transient changes in source and storage terms.

2. To carry the low frequency contribution to the long-term vertical flux.

The first role can cause $\tilde{w}\tilde{c}$ to become very large in any arbitrary periods, which

can be much larger than the mean vertical flux itself. This role is believed to be a transient effect. Therefore, if a long averaging period NP is long enough, this role would be suppressed and minimized. Then only the second role would contribute to the vertical flux. To further suppress the diurnal effects, a long period over a few days would help to balance the strong daytime fluxes with the weak nighttime fluxes as well as suppress any extreme days in between. Therefore, only the low frequency part of the diurnal effects would be left at the end, which would show as a weak inflection at this scale. However, a long period over a few days would also intensify errors in $\tilde{w}\tilde{c}$. These errors may be from instrumentation drift, gaps and some synoptic scale events. The LITFASS-2003 experiment lasted only about a month and was well installed, therefore, instrumentation drift can be neglected. Hence, any long period, which is not influenced by any synoptic events with minimum gaps, is suitable for the investigation by the block ensemble average. Note that over long averaging period, $\langle Q^* \rangle$ and $\langle Q_G \rangle$ are stable. This means that $\langle Res \rangle$ only depends on $\langle Q_H \rangle$ and $\langle Q_E \rangle$.

This block ensemble average was applied to the data set from the Amazonian rain forest in Finnigan et al. (2003). From this article, the residual reaches zero at around 4 hours. A similar strategy was applied on the 15-day data set from the maize field (A6) of the LITFASS-2003 experiment during 2 June 2003 18:00 UTC - 18 June 2003 00:00 UTC (Mauder and Foken, 2006). Overlapping blocks ensemble average was used, with the starting point of each consecutive block being shifted by 5 minutes. The period P of the block ensemble average was varied from 5 minutes to 5 days. The flux corrections as mentioned in the section 2.3 were applied in each individual blocks. It is shown that the energy balance is closed within a day and mainly caused by the increase of $\langle Q_H \rangle$.

In this thesis, to investigate whether the block ensemble average could generally close the energy balance, the block ensemble average was applied to the same data set as in the MOG (all listed station in Table 3.1, except A1 and A2) and used an identical period as in Mauder and Foken (2006). The moving block average was chosen, as it could span throughout the entire period of interest. The starting points of each consecutive block was shifted by 10 minutes, because many data sets to be used in this analysis are only available at every 10 minutes. Since data from all EC towers of the LITFASS-2003 experiment was already analyzed over 30-minute period (Beyrich et al., 2006; Foken et al., 2010), it is not necessary to investigate the averaging period shorter than 30 minutes. Therefore, the block ensemble period P was varied from 30 minutes to 5 days. The same flux corrections as in Mauder

and Foken (2006) were also applied here as well.

4.1.3 Scale analysis

In the time average analysis, the wavelet analysis (section 2.5) was used to inspect scales of eddies that contribute to the turbulent fluxes. To investigate the low frequency contribution from SC, the low frequency data might be enough. However, it would be more meaningful to compare all possible scales of eddies that can be resolved by an EC tower, in which the raw high frequency data are needed. The wavelet analysis demands a lot of computing resources when analyzing the high frequency data. Therefore, it is almost impossible to apply the wavelet analysis over a long period at once. The available computing resource, employed in this thesis, allowed the calculation of the longest period up to five days for the high frequency data.

In this thesis, the wavelet analysis firstly applied to data from A5, A6, NV, M50 and M90 stations, whose raw high frequency data are available. If the separation between small and large scales eddies are very distinctive, the low frequency data would be sufficient to inspect the large scale eddies.

4.2 Results and discussions

4.2.1 Modified ogive analysis

For ground-based stations, the data selection criteria (section 3.2.3) ruled out most of nighttime periods in both MOG analyses, because their turbulent fluxes were below thresholds. The measuring stations with broader undisturbed wind sectors, which are A5 (rye), NV (grass) and HV (pine forest), were expected to have more qualified periods. This was confirmed by number of qualified periods from NV and A5 stations. However, number of qualified periods of HV for the MOG of energy balance component was much less than other two measuring stations. This was because many data period from HV randomly had poor steady state flags (flag 4-9) of Q_E throughout the day. This was in contrast to data from FS (lake), whose steady state flags of Q_H were randomly poor. Because of these unsteadiness in Q_H and Q_E, many data periods were removed from HV (forest) and FS (lake) stations. Over low vegetation, steady state flags of Q_H and Q_E were normally good between 6:00 - 16:00 UTC. Some random unsteady period mostly appeared in the afternoon. For all selected measuring stations, steady states flags of F_c (if measurements were

available) were randomly poor throughout the day, while steady state flags of u_* were mostly good (flag 1-3). Hence, passing the steady state criterion, is mainly dependent on the stationary of Q_H, Q_E and F_c. At the end, in each measuring station, only 5% -20% of available periods were left for the MOG. They mainly spanned the duration between 6:00 - 16:00 UTC. For the energy balance components, they all had unstable stratification. While for F_c, there were a few periods with stable stratification.

The results of the MOG of energy balance component (u_*, Q_H and Q_E) and CO_2 flux (u_* and F_c) are shown in Table 4.2 and 4.3 respectively. These two tables report the number of qualified periods for the MOG (Tot #, column 1), the average of $\overline{F}_{30}$ ($\left\langle \overline{F}_{30} \right\rangle$, column 4, 6 and 9), and the percentage of qualified periods in each ogive case (#, column 5, 8 and 11). All sets of information are reported at two different sizes of error bands (η), 10% and 20%, which must be larger than the threshold fluxes (section 3.2.3). For case 2 and 3, the average of maximum flux difference for each case ($\langle \Delta_{max} \rangle$, column 7 and 10) is also presented.

According to the physical appearance of the surfaces, all selected measuring stations could be classified into three categories, which were lake (FS), low vegetation (A3-A9 and NV) and forest (HV). u_* seemed to be the only one that strictly followed this classification, while Q_H did so loosely. $\left\langle \overline{F}_{30} \right\rangle$ of u_* and Q_H were highest over the forest and smallest over the lake. For low vegetation, $\left\langle \overline{F}_{30} \right\rangle$ of u_* closely grouped together, while $\left\langle \overline{F}_{30} \right\rangle$ of Q_H grouped dispersedly. There was not much difference in $\left\langle \overline{F}_{30} \right\rangle$ of Q_E and F_c between forest and low vegetation outside the southern part of the LITFASS area. The southern part of the LITFASS area was significantly affected by the heavy rain events on 5 June 2003, which probably extremized Q_E and F_c in A7-A9 and FS stations.

Both MOG of energy balance components and CO_2 flux gave quite similar results in u_*. The MOG classified most periods from all sites as Case 1. This suggests that the time extension has almost no impact on u_* regardless of canopy types.

Over lake and low vegetation, the MOG classified most qualified period of both Q_H and Q_E as Case 1. This suggests that 30-minute averaging time is generally sufficient to capture most of turbulent fluxes. However, there were significant numbers of Case 2 and 3 of both Q_H and Q_E in some of low vegetation stations and remarkably forest stations (HV). These periods of Case 2 and 3 of low vegetation sites were closely related to the stationary of Q_H and Q_E over 4-hour period. For low vegetation sites, periods of Case 1 of Q_H and Q_E usually had 4-hour steady state flag 1, while Case 2 and 3 usually had flag 2 or more. This relation was not obviously observed in the forest site. This implies that when the atmosphere becomes less stationary at longer averaging time, the measured fluxes over low vegetation can

be either increased or decreased. As number of Case 3 was normally greater than number of Case 2 in both Q_H and Q_E for low vegetation and forest, the averaging time extension would tend to increase Q_H and Q_E. For Case 3 in low vegetation, Q_H broadly increased more than Q_E. This suggests that the averaging time extension has more impact on Q_H. The average maximum flux difference $\langle \Delta_{max} \rangle$ increased with the size of an error band (η), while less number of Case 2 and 3 was observed. This was because the fewer periods left had larger Δ_{max}. Eventually, even with the greatest Δ_{max} added on the top of flux corrections, it was still not enough to close the energy balance. Furthermore, from scalar similarity of Q_H and Q_E, these measured fluxes were expected to increase or decrease together. Thus Case 2 or Case 3 in both Q_H and Q_E should be observed simultaneously, which after all rarely happened over low vegetation. It must be noted that in A7 (Rape), the residual was relatively small and quite comparable with the measurement errors of Q_H and Q_E. Hence, small fluxes increasing from the averaging time extension might close the energy balance in this site. However, this closure would not be the act of large scale eddies.

Table 4.2: Results from the modified ogive analysis of the energy balance components (u_*, Q_H and Q_E) of the LITFASS-2003 experiment between 20 May 2003, 1200 UTC - 18 June 2003, 0000 UTC. Notations: Tot # is the number of qualified periods for the MOG; η is the width of error band, which is set to be 10% and 20% of $\overline{F}_{30}$ (average flux at 30 min period of each run) and has a minimum value equals to the measurement error of each turbulent flux; $\langle \overline{F}_{30} \rangle$ is the average of $\overline{F}_{30}$ from all runs in each ogive case; # is the percentage of qualified periods in each ogive case; $\langle \Delta_{max} \rangle$ is the average of Δ_{max} (maximum flux difference) from in each ogive case. Note that the unit of each specified flux in column 2 only applies to quantities in column 4, 6, 7, 9 and 10 of the same row.

Station (Tot #)	**Flux**	η (%)	**Case 1** $\langle \overline{F}_{30} \rangle$	**Case 1** #(%)	**Case 2** $\langle \overline{F}_{30} \rangle$	**Case 2** $\langle \Delta_{max} \rangle$	**Case 2** #(%)	**Case 3** $\langle \overline{F}_{30} \rangle$	**Case 3** $\langle \Delta_{max} \rangle$	**Case 3** #(%)
Forest	u_*	10	0.68	100.0	-	-	0.0	-	-	0.0
	(ms^{-1})	20	0.68	100.0	-	-	0.0	-	-	0.0
HV	Q_H	10	261	74.8	205	-33	3.3	224	33	22.0
	(Wm^{-2})	20	252	96.7	237	-56	0.8	217	70	2.4
(123)	Q_E	10	107	43.1	128	-33	9.8	119	27	47.2
	(Wm^{-2})	20	112	75.6	126	-45	4.9	125	40	19.5
Rye	u_*	10	0.30	100.0	-	-	0.0	-	-	0.0
	(ms^{-1})	20	0.30	100.0	-	-	0.0	-	-	0.0
A3	Q_H	10	188	93.7	124	-13	1.6	124	15	4.8
	(Wm^{-2})	20	184	100.0	-	-	0.0	-	-	0.0
(63)	Q_E	10	84	92.1	51	-12	4.8	55	11	3.2
	(Wm^{-2})	20	81	100.0	-	-	0.0	-	-	0.0

Continued on next page

Table 4.2 – continued from previous page

Station (Tot #)	**Flux**	η (%)	**Case 1** $\langle\overline{F}_{30}\rangle$	#(%)	**Case 2** $\langle\overline{F}_{30}\rangle$	$\langle\Delta_{max}\rangle$	#(%)	**Case 3** $\langle\overline{F}_{30}\rangle$	$\langle\Delta_{max}\rangle$	#(%)
Rye	u_*	10	0.34	96.8	0.25	-0.03	0.9	0.14	0.03	2.3
	(ms^{-1})	20	0.34	99.5	-	-	0.0	0.07	0.05	0.5
A5	Q_H	10	148	88.1	99	-15	2.8	85	19	9.2
	(Wm^{-2})	20	143	97.7	-	-	0.0	61	36	2.3
(218)	Q_E	10	145	89.9	118	-20	4.6	131	23	5.5
	(Wm^{-2})	20	143	97.2	116	-26	0.9	132	30	1.8
Triticale	u_*	10	0.35	100.0	-	-	0.0	-	-	0.0
	(ms^{-1})	20	0.35	100.0	-	-	0.0	-	-	0.0
A8	Q_H	10	180	98.1	117	-18	1.9	-	-	0.0
	(Wm^{-2})	20	179	100.0	-	-	0.0	-	-	0.0
(107)	Q_E	10	125	100.0	-	-	0.0	-	-	0.0
	(Wm^{-2})	20	125	100.0	-	-	0.0	-	-	0.0
Maize	u_*	10	0.34	82.9	-	-	0.0	0.23	0.04	17.1
	(ms^{-1})	20	0.32	97.4	-	-	0.0	0.26	0.06	2.6
A4	Q_H	10	123	75.0	106	-13	2.6	114	42	22.4
	(Wm^{-2})	20	121	84.2	-	-	0.0	115	54	15.8
(76)	Q_E	10	129	77.6	104	-27	15.8	73	23	6.6
	(Wm^{-2})	20	124	89.5	110	-44	6.6	81	28	3.9
Maize	u_*	10	0.31	94.0	0.18	-0.03	4.3	0.15	0.03	1.7
	(ms^{-1})	20	0.30	99.1	0.14	-0.04	0.9	-	-	0.0
A6	Q_H	10	106	84.6	98	-12	2.6	116	28	12.8
	(Wm^{-2})	20	108	94.9	-	-	0.0	92	39	5.1
(117)	Q_E	10	134	82.9	77	-20	12.0	80	18	5.1
	(Wm^{-2})	20	127	95.7	91	-37	2.6	57	22	1.7
Rape	u_*	10	0.28	100.0	-	-	0.0	-	-	0.0
	(ms^{-1})	20	0.28	100.0	-	-	0.0	-	-	0.0
A7	Q_H	10	127	90.4	83	-13	8.5	94	12	1.1
	(Wm^{-2})	20	123	100.0	-	-	0.0	-	-	0.0
(94)	Q_E	10	181	98.9	-	-	0.0	141	16	1.1
	(Wm^{-2})	20	181	100.0	-	-	0.0	-	-	0.0

Continued on next page

Table 4.2 – continued from previous page

Station (Tot #)	**Flux**	η (%)	**Case 1** $\langle\overline{F}_{30}\rangle$	#(%)	**Case 2** $\langle\overline{F}_{30}\rangle$	$\langle\Delta_{max}\rangle$	#(%)	**Case 3** $\langle\overline{F}_{30}\rangle$	$\langle\Delta_{max}\rangle$	#(%)
Rape	u_*	10	0.30	100.0	-	-	0.0	-	-	0.0
	(ms^{-1})	20	0.30	100.0	-	-	0.0	-	-	0.0
A9	Q_H	10	114	91.7	98	-11	1.7	109	15	6.7
	(Wm^{-2})	20	114	100.0	-	-	0.0	-	-	0.0
(60)	Q_E	10	200	100.0	-	-	0.0	-	-	0.0
	(Wm^{-2})	20	200	100.0	-	-	0.0	-	-	0.0
Grass	u_*	10	0.34	92.5	-	-	0.0	0.15	0.02	7.5
	(ms^{-1})	20	0.33	100.0	-	-	0.0	-	-	0.0
NV	Q_H	10	117	93.0	101	-15	6.0	132	23	1.0
	(Wm^{-2})	20	116	99.5	99	-27	0.5	-	-	0.0
(201)	Q_E	10	131	86.1	95	-19	2.0	118	19	11.9
	(Wm^{-2})	20	140	97.5	94	-31	0.5	114	27	2.0
Lake	u_*	10	0.21	90.3	0.09	-0.02	1.4	0.16	0.02	8.3
	(ms^{-1})	20	0.20	100.0	-	-	0.0	-	-	0.0
FS	Q_H	10	40	95.8	-	-	0.0	31	14	4.2
	(Wm^{-2})	20	40	100.0	-	-	0.0	-	-	0.0
(72)	Q_E	10	197	95.8	93	-15	1.4	121	14	2.8
	(Wm^{-2})	20	193	100.0	-	-	0.0	-	-	0.0
50 m	u_*	10	0.54	66.3	0.25	-0.06	8.1	0.36	0.06	25.6
	(ms^{-1})	20	0.49	91.9	0.18	-0.08	3.5	0.28	0.09	4.7
M50	Q_H	10	109	39.5	117	-25	23.3	109	24	37.2
	(Wm^{-2})	20	111	76.7	107	-38	8.1	114	36	15.1
(86)	Q_E	10	170	38.4	125	-21	4.7	140	28	57.0
	(Wm^{-2})	20	154	72.1	-	-	0.0	143	37	27.9
90 m	u_*	10	0.61	74.3	0.17	-0.05	2.9	0.44	0.06	22.9
	(ms^{-1})	20	0.57	97.1	0.17	-0.05	2.9	-	-	0.0
M90	Q_H	10	118	28.6	110	-21	37.1	115	19	34.3
	(Wm^{-2})	20	117	85.7	104	-33	8.6	85	31	5.7
(35)	Q_E	10	207	42.9	190	-62	5.7	171	37	51.4
	(Wm^{-2})	20	196	77.1	172	-97	2.9	155	52	20.0

Table 4.3: Results from the modified ogive analysis of CO_2 flux (u_* and F_c). The description is similar to Table 4.2.

Station (Tot #)	**Flux**	η (%)	**Case 1** $\langle \overline{F}_{30} \rangle$	#(%)	**Case 2** $\langle \overline{F}_{30} \rangle$	$\langle \Delta_{max} \rangle$	#(%)	**Case 3** $\langle \overline{F}_{30} \rangle$	$\langle \Delta_{max} \rangle$	#(%)
Forest	u_*	10	0.64	99.5	-	-	0.0	0.38	0.06	0.5
HV	(ms^{-1})	20	0.64	100.0	-	-	0.0	-	-	0.0
(192)	F_C	10	8.68	58.3	8.25	-1.57	12.5	7.43	1.54	29.2
	($\mu mol\ m^{-2}s^{-1}$)	20	8.29	89.1	7.73	-2.48	4.2	8.21	3.23	6.8
Triticale	u_*	10	0.34	100.0	-	-	0.0	-	-	0.0
A8	(ms^{-1})	20	0.34	100.0	-	-	0.0	-	-	0.0
(124)	F_C	10	15.78	99.2	-	-	0.0	15.65	1.89	0.8
	($\mu mol\ m^{-2}s^{-1}$)	20	15.78	100.0	-	-	0.0	-	-	0.0
Maize	u_*	10	0.31	97.4	0.26	-0.03	0.9	0.15	0.03	1.8
A6	(ms^{-1})	20	0.31	100.0	-	-	0.0	-	-	0.0
(114)	F_C	10	9.09	62.3	7.13	-1.56	14.0	7.34	2.40	23.7
	($\mu mol\ m^{-2}s^{-1}$)	20	8.69	78.9	7.10	-1.70	10.5	7.52	4.09	10.5
Rape	u_*	10	0.32	100.0	-	-	0.0	-	-	0.0
A9	(ms^{-1})	20	0.32	100.0	-	-	0.0	-	-	0.0
(91)	F_C	10	17.57	96.7	9.21	-1.59	2.2	19.75	2.70	1.1
	($\mu mol\ m^{-2}s^{-1}$)	20	17.41	100.0	-	-	0.0	-	-	0.0
Grass	u_*	10	0.33	88.8	-	-	0.0	0.27	0.04	11.2
NV	(ms^{-1})	20	0.33	96.6	-	-	0.0	0.22	0.05	3.4
(206)	F_C	10	9.95	74.3	8.80	-1.67	14.1	7.65	1.27	11.7
	($\mu mol\ m^{-2}s^{-1}$)	20	9.57	94.7	8.47	-2.74	3.9	9.41	2.82	1.5
50m	u_*	10	0.52	41.2	0.23	-0.08	3.9	0.44	0.08	54.9
M50	(ms^{-1})	20	0.50	77.8	0.19	-0.09	2.6	0.35	0.10	19.6
(153)	F_C	10	12.06	15.7	8.84	-3.13	9.8	11.58	2.38	74.5
	($\mu mol\ m^{-2}s^{-1}$)	20	11.68	62.1	8.11	-4.25	5.9	11.42	3.21	32.0
90m	u_*	10	0.54	40.2	0.25	-0.11	6.9	0.50	0.08	52.9
M90	(ms^{-1})	20	0.53	77.5	0.23	-0.13	4.9	0.45	0.10	17.6
(102)	F_C	10	13.69	10.8	13.91	-2.46	3.9	10.86	2.82	85.3
	($\mu mol\ m^{-2}s^{-1}$)	20	11.53	42.2	12.08	-3.04	2.0	11.07	3.49	55.9

For F_c, Case 1 was still a majority, with larger fraction of Case 2 and 3 than the energy balance components. Forest also had larger fraction of Case 2 and 3 than did low vegetation. Overall, number of Case 3s was greater than number of Case 2s, and $\langle \Delta_{max} \rangle$ of F_c also increased with η. The 4-hour steady state flags were

normally 1 for Case 1 and higher for Case 2 and Case 3. However, Case 2 generally had higher steady state flags than Case 3. This suggests that when the atmosphere becomes less stationary at longer averaging time, the measured F_c tends to increase. However, when the degree of unsteadiness becomes stronger, the measured F_c start to decrease.

Number of qualified periods for the MOG of M50 and M90, which measured fluxes on the same tower at different heights, was very low. This should be caused by more unsteadiness at higher measurement height. High number of Case 3s in u_* indicates that the averaging time extension can eventually increase u_*. Large fraction of Case 2 and Case 3 in both Q_H and Q_E were observed at both measurement heights. Additionally, Case 3 were observed simultaneously with either Case 2 or Case 3 in both Q_H and Q_E. The measurement heights of these two stations should be high enough (probably outside the ASL) to observe SC regularly. Therefore, all these evidences might imply that outside the ASL, SC can significantly effect Q_H and Q_E, which can be observed at a longer averaging time.

4.2.2 Block ensemble average

The block ensemble average (Eq. 4.13) of various measuring stations during 2 June 2003 18:00 UTC - 18 June 2003 00:00 UTC, are shown in Fig. 4.3. This period was chosen as a long period NP to repeat Mauder and Foken (2006) with some minor modifications (section 4.1.2). It was found that the result from A6 (Maize) station differed from the original one by less than a measurement errors of Q_H and Q_E. Therefore, these modifications still give the comparable results, which would allow modifications to other data sets to be applied confidently.

The outcome of block ensemble average was quite unexpected, because it could not close the energy balance in all sites. In all stations, both $\langle Q_H \rangle$ and $\langle Q_E \rangle$ were relatively constant in the first few hours. This finding is consistent with the results from the ogive analysis, in which the averaging time extension for a few hours would not much change the measured fluxes. When a block ensemble period P was longer than a few hours, the block ensemble average fluxes started to change. In most stations, $\langle Q_E \rangle$ were more steady at longer P.

The closures in A4 (maize), A5 (rye) and A6 (maize) were around 15 - 30 hours, which is closed to the results in Mauder and Foken (2006), and were mainly caused by the increase of $\langle Q_H \rangle$ with longer P. Note that there was an abrupt decrease of $\langle Q_H \rangle$ at very large P in A4 (maize). In A9 (rape), the increase of $\langle Q_H \rangle$ with P could not close the energy balance, because it was canceled with the decrease of $\langle Q_E \rangle$. The

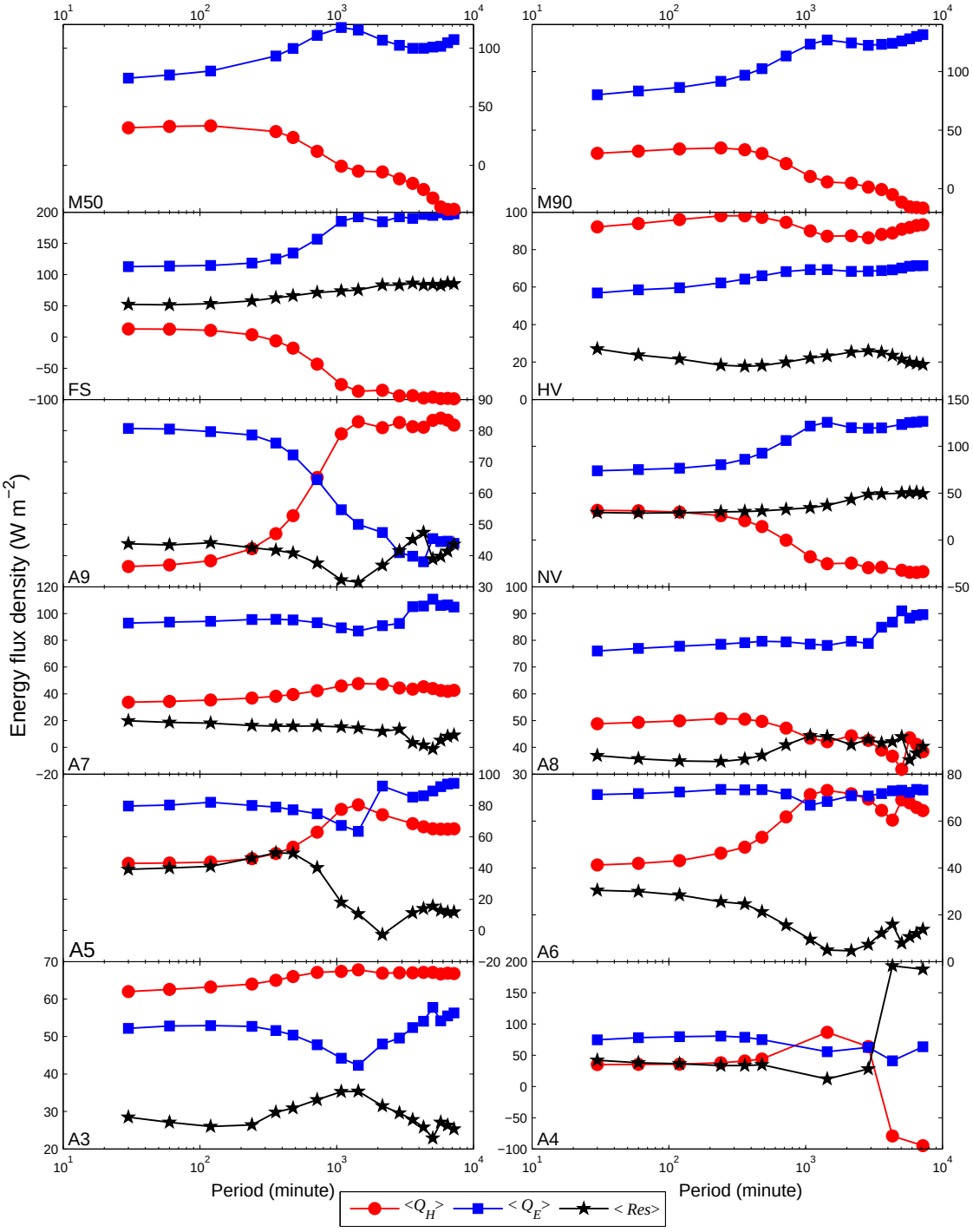

Figure 4.3: Block ensemble average fluxes evaluated using data from EC towers of the LITFASS-2003 experiment during 2 June 2003 18:00 UTC - 18 June 2003 00:00 UTC. These EC towers covered these following land uses: pine forest (HV), barley (A3), maize (A4, A6), rye (A5), rape (A7, A9), triticale (A8), grassland (NV, M50, M90) and lake (FS). M50 and M90 measured fluxes at 50 m and 90 m heights respectively.

other way around was found in FS (lake) and NV (grass), in which the increase of $\langle Q_E \rangle$ was canceled with the decrease of $\langle Q_H \rangle$, which kept the residual approximately constant at all P. Moreover, the interpretation in FS must be done carefully, because the lake has different characteristics from other terrain sites, like very high heat capacity and very low surface friction. For HV (forest), even the residual was quite low at all P, the closure can be concluded only if a precise estimation of the canopy heat storage has been included (section 3.2.2). Unfortunately, only some of required biomass properties of the forest were collected during the LITFASS-2003 experiment, the canopy heat storage can be precisely estimated . For A7 (rape), its residual was quite low and the energy balance seems to be closed at all P. Additionally, a small bump in $\langle Q_E \rangle$ at very long P was also presented in A8 (triticale) and A9 (Rape), which was probably caused by a heavy rain event in the southern part of the LITFASS area on 5 June 2003.

The inflections at the diurnal scale were found in all sites for both $\langle Q_H \rangle$ and $\langle Q_E \rangle$. As all these sites were practically in the same 20x20 km^2 area, the diurnal effects should not be much different and the degree of inflection should be similar. Therefore, the stronger inflection over some sites and fluxes might not be entirely caused by the diurnal effects.

Since the block ensemble average could not close the energy balance for all sites between 2 June 2003 18:00 UTC - 18 June 2003 00:00 UTC, it was suspected whether other observational period would behave similarly and was there anything in common among the sites that the block ensemble average could close the energy balance. As the change in the block ensemble average fluxes started at period P beyond a few hours, it would be contributed from the low frequency turbulence, which is related to the mesoscale flux $\tilde{w}\tilde{c}$. Therefore, the investigation should be directed to this term. In principle, $\tilde{w}\tilde{c}$ represents the flux contribution from eddies scale larger than P and smaller than NP. If P is set to be 30 minutes, $\tilde{w}\tilde{c}$ would represent additional flux after 30-minute averaging time up to period NP. Hence, long term observation of $\tilde{w}\tilde{c}$ would show variation of additional fluxes from the low frequency contribution, which may related to observed block ensemble average fluxes. These variations can be observed more clearly, when the observation period is long enough to suppress any transient effects in the block ensemble average fluxes.

The long period NP, which covered an entire period of LITFASS-2003 experiment, was during 20 May 2003 12:00 UTC - 18 June 2003 00:00 UTC. Since this long period is much longer than 30 minutes, the period P of 30 minutes could span all through an entire period. Hence, non-overlapping block average would be enough to

show the tendency of the mesoscale fluxes. $\tilde{w}\tilde{c}$ from all 30-minute non-overlapping blocks ($P = 30$ minutes) within this long period NP were determined to construct the Hovmøller diagrams of $\tilde{Q}_H$ ($\tilde{w}\tilde{T}$ in energetic units, T is temperature) and $\tilde{Q}_E$ ($\tilde{w}\tilde{a}$ in energetic units, a is absolute humidity). These diagrams would show the variation of additional fluxes beyond 30-minute averaging time. According to section 4.1.2, $\tilde{w}\tilde{c}$ can be very large in any arbitrary blocks. Therefore, some random large $\tilde{Q}_H$ and $\tilde{Q}_E$ in these diagrams were expected.

The Hovmøller diagrams of $\tilde{Q}_H$ and $\tilde{Q}_E$ from all stations during 20 May 2003 12:00 UTC - 18 June 2003 00:00 UTC are shown in Fig 4.4 and 4.5. Other than some randomly large $\tilde{Q}_H$ and $\tilde{Q}_E$, their consecutive large values were also observed in many stations. To observe the consistency with the block ensemble average (Fig. 4.3), part of these diagrams between 2 June 2003 18:00 UTC to 18 June 2003 00:00 UTC were firstly considered. The increase of $\langle Q_H \rangle$ at longer P in A4 (maize), A5 (rye) and A6 (maize) were consistent with consecutive large positive $\tilde{Q}_H$ at the beginning of this period. Since in A4 (maize), this period was actually dominated by negative $\tilde{Q}_H$ and its consecutive large positive $\tilde{Q}_H$ was not as strong as in A5 (rye) and A6 (maize), its $\langle Q_H \rangle$ suddenly dropped at very large P. Some extremely large negative $\tilde{Q}_E$ in A5 (rye) were consistent with the small decrease of $\langle Q_E \rangle$ at longer P, which instantaneously boosted up at around 36 hours, by one large positive $\tilde{Q}_E$ on 6-7 June 2003. Consecutive large negative $\tilde{Q}_E$ in NV (grass) and FS (lake) were also consistent with their increase of $\langle Q_E \rangle$ at longer P. The increase of $\langle Q_H \rangle$ and decrease of $\langle Q_E \rangle$ at longer P were caused by randomly large positive $\tilde{Q}_H$ and extremely large negative $\tilde{Q}_E$.

The consistency between the block ensemble average fluxes and Hovmøller diagrams of mesoscale fluxes shows that large mesoscale fluxes can significantly effect the block ensemble average fluxes. According to Finnigan et al. (2003, , section 4.1.2), large mesoscale fluxes are expected to be transient effects to cancel strong horizontal divergences in an individual block, in which suitable long period NP would suppress their effects. The randomly large mesoscale fluxes can fit with this description very well, while the consecutive large mesoscale fluxes do not, because they are certainly not transient effects. If the period of consecutive large mesoscale fluxes is not influenced by any significant synoptic events, a strong horizontal divergence can be caused by a strong horizontal advection, which is apparently related to secondary circulations (SC). This statement can be somewhat confirmed by large mesoscale fluxes, which were found more often in M50 and M90 (measured fluxes at 50 m and 90 m heights respectively, Fig. 4.5), because SC are believed to mostly

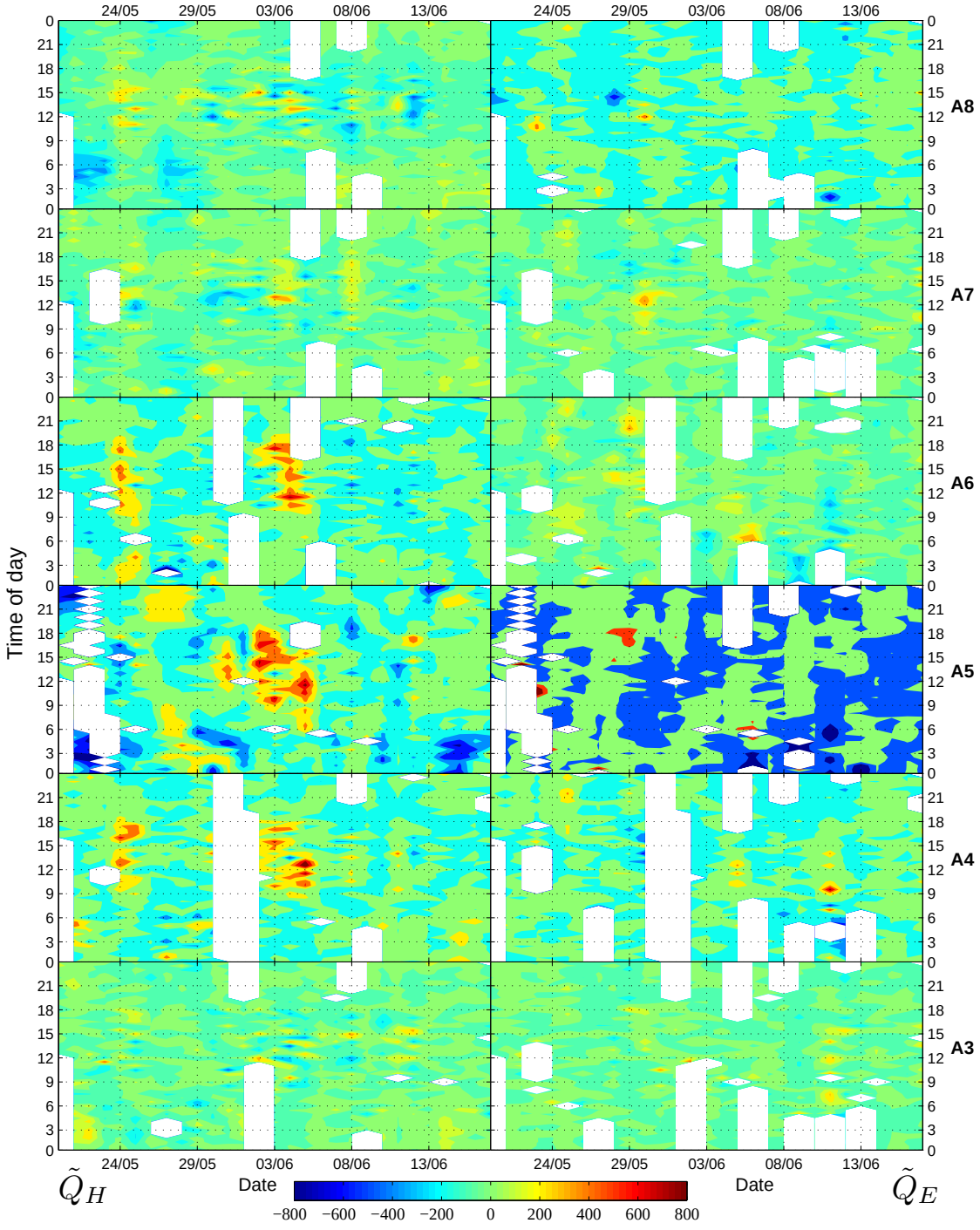

Figure 4.4: Hovmøller diagrams of mesoscale fluxes evaluated using data from EC towers of the LITFASS-2003 experiment during 20 May 2003 12:00 UTC - 18 June 2003 00:00 UTC. Diagrams on the left-hand side represent mesoscale fluxes of the sensible heat ($\tilde{Q}_H$), while ones on the right-hand side represent mesoscale fluxes of the latent heat ($\tilde{Q}_E$). These EC towers covered these following land uses: barley (A3), maize (A4, A6), rye (A5), rape (A7) and triticale (A8).

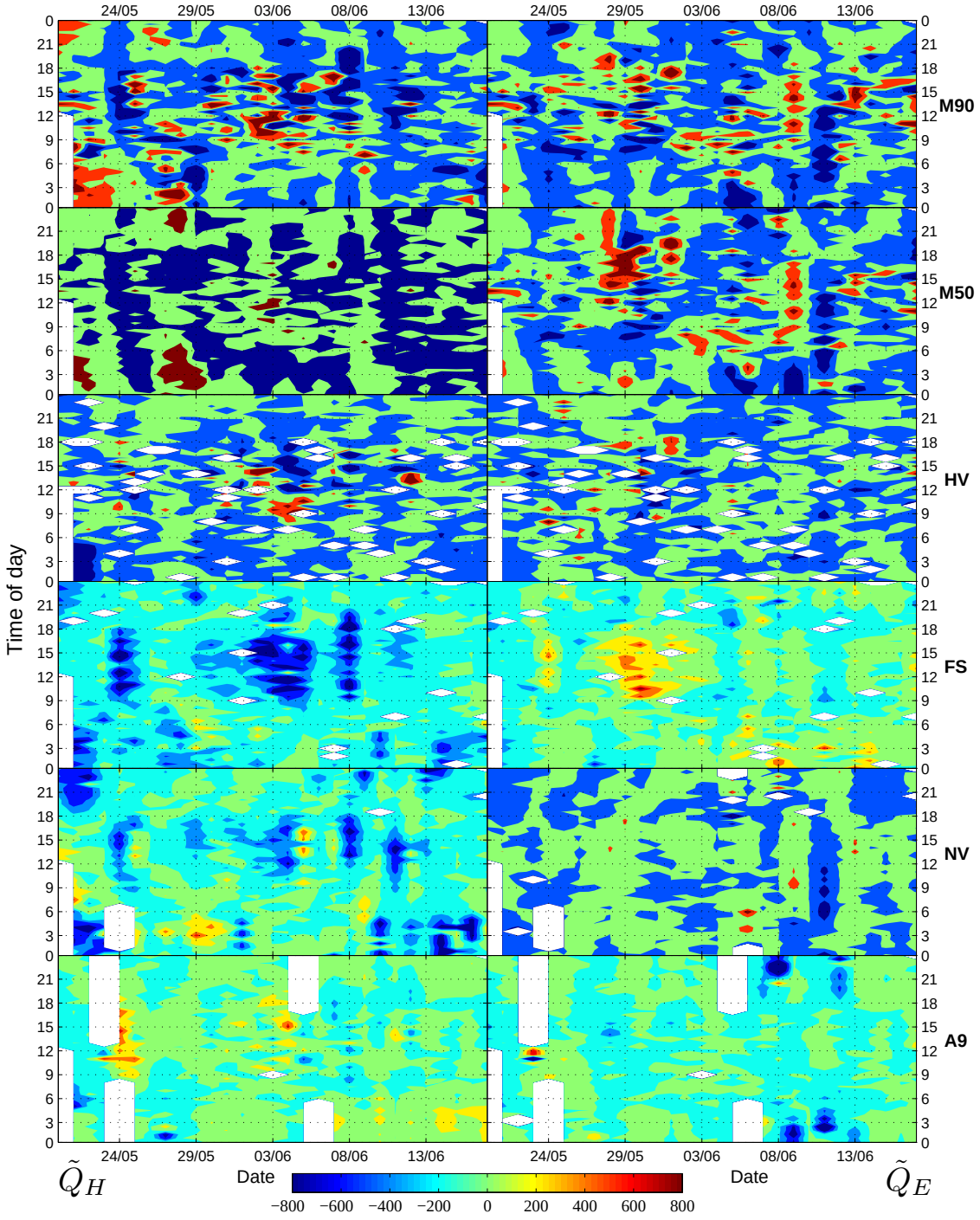

Figure 4.5: Hovmøller diagrams of mesoscale fluxes evaluated using data from EC towers of the LITFASS-2003 experiment during 20 May 2003 12:00 UTC - 18 June 2003 00:00 UTC. Diagrams on the left-hand side represent mesoscale fluxes of the sensible heat ($\tilde{Q}_H$), while ones on the right-hand side represent mesoscale fluxes of the latent heat ($\tilde{Q}_E$). These EC towers covered these following land uses: rape (A9), grassland (NV, M50, M90), lake (FS) and pine forest (HV). M50 and M90 measured fluxes at 50 m and 90 m heights respectively.

exist outside the ASL. It was noticed that in M50 and M90, large $\tilde{Q}_E$ were also found as often as $\tilde{Q}_H$, which were consistent with the increasing or decreasing of both $\langle Q_H \rangle$ and $\langle Q_E \rangle$ at longer P.

To observe the effect of SC in the ASL more clearly, the other period NP should be investigated. This period should contain consecutive large mesoscale fluxes, might has few gaps, and must not be influenced by any synoptic events. To find this new period of interest, the Hovmøller diagram of mesoscale fluxes were constructed in two different ranges. The first range, the Hovmøller diagram could show the mesoscale fluxes, which were larger than usual. For the LITFASS-2003 experiment, this suitable range was found to be between -800 to 800 W m^{-2} (as shown in Fig. 4.4 and 4.5). This range could show possible period that contain SC as consecutive large mesoscale fluxes, however, the extreme mesoscale fluxes caused by errors or synoptic events might just be hidden inside this pattern. Therefore, the Hovmøller diagram with the second range, which covered all observed scales, was constructed to separate extremely large mesoscale fluxes from the rest. For all ground-based stations of the LITFASS-2003 experiment, the extremely large fluxes could be as large as -1400 W m^{-2}. For example, the southern part of the LITFASS area was suffered by a heavy rain event on the evening of 5 June 2003, which conformed with the extremely large $\tilde{Q}_H$ (up to -1400 W m^{-2}, not shown in any diagrams in this thesis). It was very interesting that in all ground-based stations, none of consecutive large $\tilde{Q}_E$ was found without influence from synoptic events. This would suggest that SC are mainly transport Q_H.

The period between 1 - 5 June 2003 seemed to be a good candidate as it contained consecutive large $\tilde{Q}_H$ in A4 (maize), A5 (rye) and A6 (maize), and was not disturbed by any significant synoptic events. Since there were large data gaps in A6 (maize) on the morning of 1 June 2003 and to complete a daily cycle, the new long period NP was chosen to be during 1 June 2003 15:00 UTC - 5 June 2003 15:00 UTC. Since this period lasted only for 4 days, the block ensemble averaging period P was varied from 10 minutes to 3 days. Note that data from A3 (barley) contained big gaps during this new period NP, hence, any justifications could not be made from this data set. The block ensemble average of this new long period from all stations is shown in Fig. 4.6. As expected, the block ensemble average could close the energy balance in A4 (maize), A5 (rye) and A6 (maize) within a day by the increase of $\langle Q_H \rangle$ at longer P.

According to Eigenmann et al. (2009), SC can reach down to levels near the earth's surface under the free convection condition. Such condition occurs when the

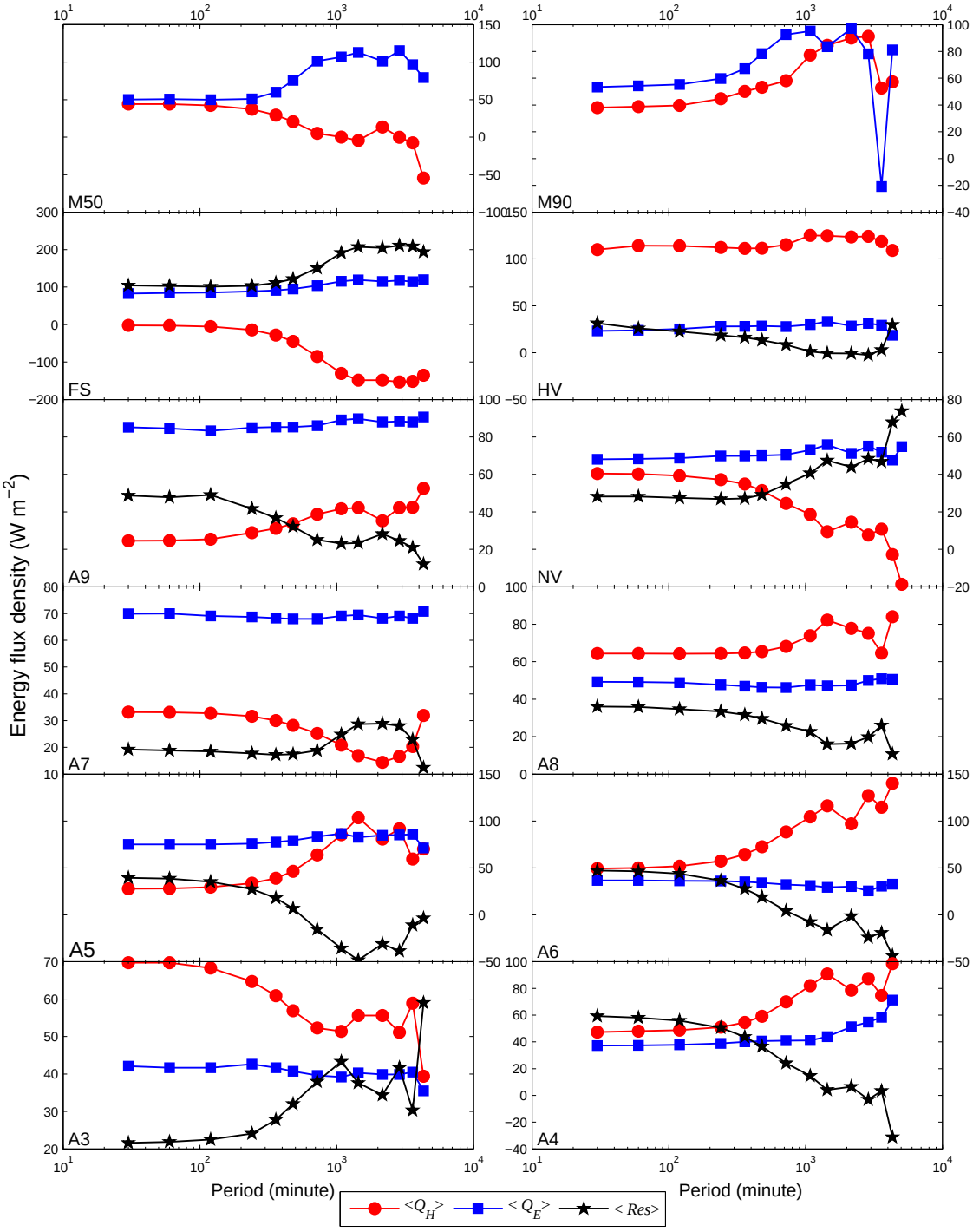

Figure 4.6: Block ensemble average fluxes evaluated using data from EC towers of the LITFASS-2003 experiment during 1 June 2003 15:00 UTC - 5 June 2003 15:00 UTC. These EC towers covered these following land uses: pine forest (HV), barley (A3), maize (A4, A6), rye (A5), rape (A7, A9), grassland (NV, M50, M90) and lake (FS). M50 and M90 measured fluxes at 50 m and 90 m heights respectively.

buoyancy term dominates the shear production term as $z/L \leq -1$. This situation is also accompanied by the low friction velocity. Since the free convection was not observed during 1 June 2003 - 5 June 2003, these near-surface SC were reasonably caused by the surface heterogeneity(Stoy et al., 2013). In case of the LITFASS area, this surface heterogeneity included the thermal heterogeneity, which could be induced by the difference in surface temperatures between different land uses.

4.2.3 Scale analysis

In this part, the wavelet analysis was applied to the raw high frequency data from A5 (rye), A6 (maize) and NV (grass) in order to resolve scales of turbulence that contribute to the vertical fluxes during 1 June 2003 15:00 UTC - 5 June 2003 15:00 UTC. Wavelet cross-scalograms from these three stations are shown in Fig. 4.7. From these diagrams, there were two turbulent scales. The smaller scale was observed daily during the daytime and transport both Q_H and Q_E. This scale ranged from a few seconds to a few minutes and should be captured by the EC measurement with 30-minute averaging time. The larger scale mainly transported Q_H and did not appear on a daily basis. At this larger scale, the positive contribution, which tended to increase Q_H was found in the A5 (rye) and A6 (maize), while negative contribution that decreased Q_H was found in NV (grass). This conformed with consecutive large $\tilde{Q}_H$ in the Hovmøller diagrams of mesoscale fluxes and the increase or decrease of the block ensemble average fluxes at longer P. According to the wind speed of A5 (rye), A6 (maize) and NV (grass), this larger scale corresponded to the inverse frequency and inverse wavenumber of around 4-5 hours and 35 km respectively, which could not be captured by the EC measurement averaging over 30-minute period.

At higher measurement height, smaller scale turbulence was slightly larger than the ground-based stations, while larger scale turbulence was found in both Q_H and Q_E. For example during 1 June 2003 15:00 UTC - 5 June 2003 15:00 UTC of M50 (50 m), the increase of $\tilde{Q}_E$ and decrease of $\tilde{Q}_H$ at longer P (Fig. 4.6) were consistent with the pattern in the Hovmøller diagrams of mesoscale fluxes (Fig. 4.5) and larger scale turbulence from the wavelet analysis (Fig. 4.8 a). Application of the wavelet analysis on the low frequency data can still show the larger scale turbulence, while loosing the information of smaller scale ones. Therefore, if only larger scale turbulence was needed to be inspected, this low frequency data would be sufficient. The wavelet cross-scalograms from low frequency data of FS (lake, $\Delta t = 10$ minutes) and A8 (triticale, $\Delta t = 5$ minutes) during 1 June 2003 15:00 UTC - 5 June 2003 15:00 UTC are shown in Fig. 4.8 b and c. For FS (lake), strong negative contribution

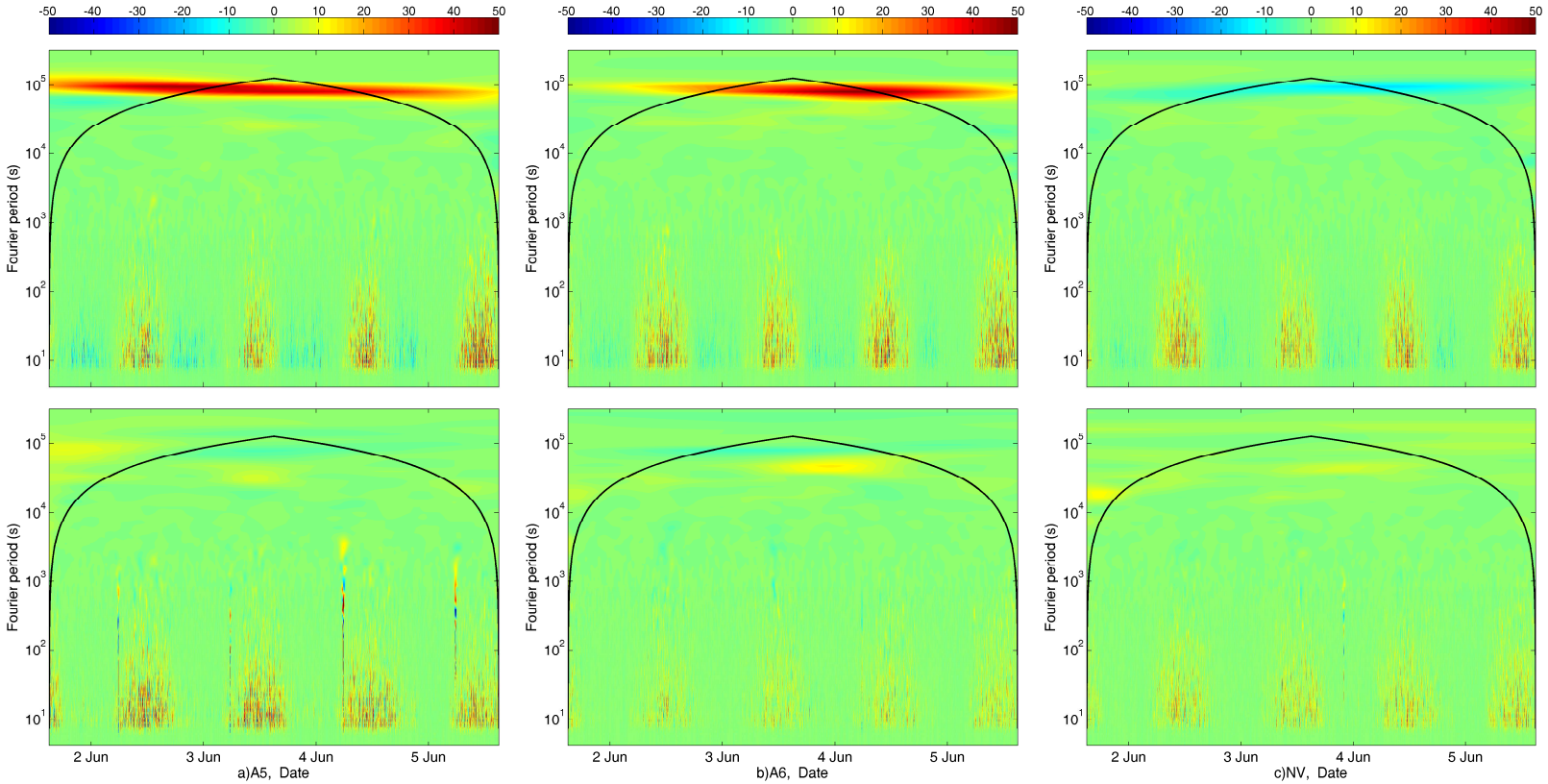

Figure 4.7: Wavelet cross-scalogram of sensible heat fluxes (upper panels) and latent heat fluxes (lower panels) evaluated using high frequency data from a) A5 (rye), b) A6 (maize) and c) NV (grass). These data sets spanned the period between 1 June 2003 15:00 UTC - 5 June 2003 15:00 UTC. Colors represent the value in W m^- and the black solid line is the cone of influence.

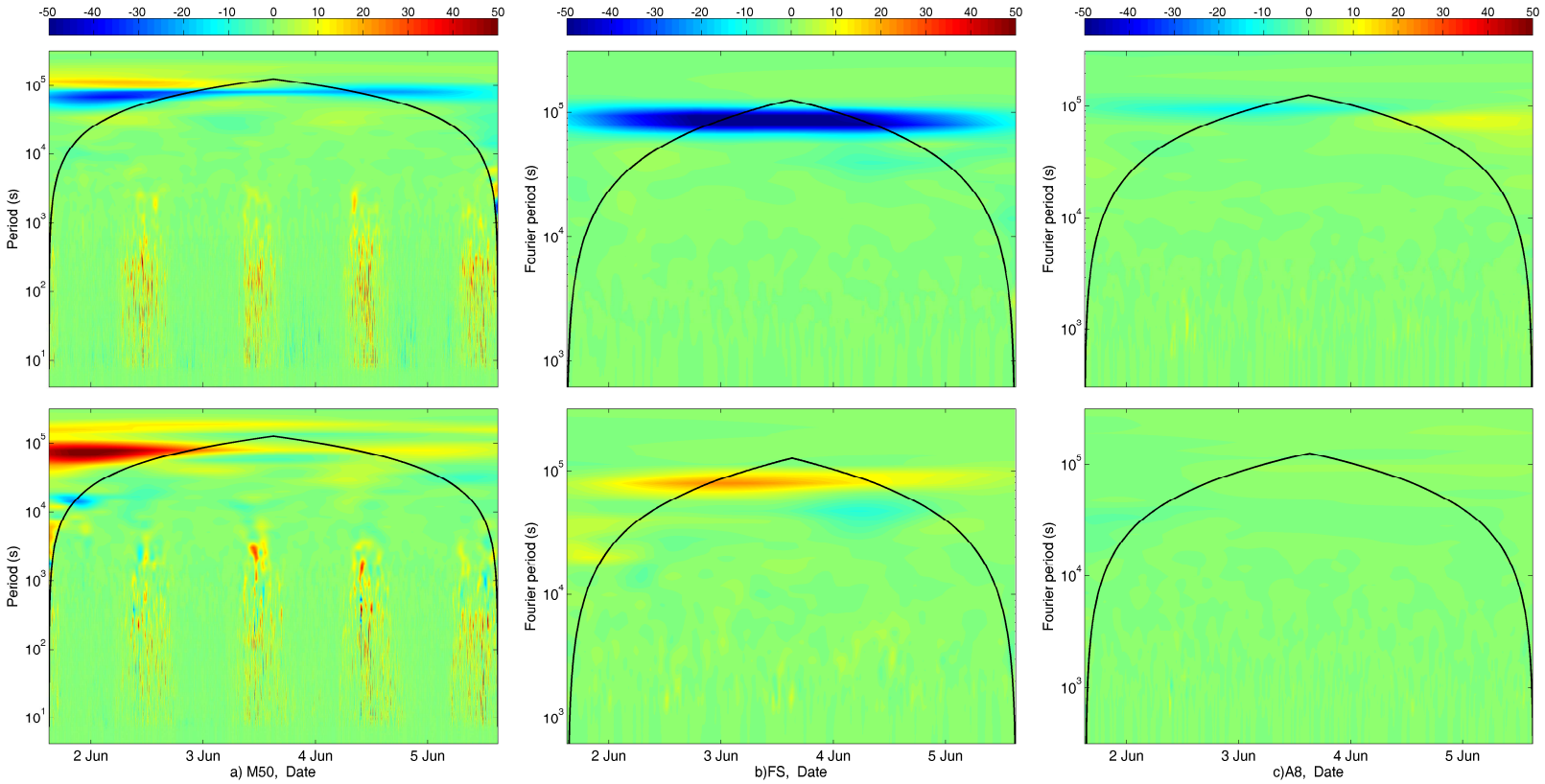

Figure 4.8: Wavelet cross-scalogram of sensible heat fluxes (upper panels) and latent heat fluxes (lower panels) evaluated using high frequency data from a) M90 (90 m), and low frequency data from b) FS (lake, $\Delta t = 10$ minutes) and c) A8 (triticale, $\Delta t = 5$ minutes) These data sets spanned the period between 1 June 2003 15:00 UTC - 5 June 2003 15:00 UTC. Colors represent the value in W m^{-} and the black solid line is the cone of influence.

was found in the larger scale turbulence, which was consistent with the consecutive large negative $\tilde{Q}_H$ and the decrease of $\langle Q_H \rangle$ at longer P. For A8 (triticale), the contribution from larger scale turbulence was not significant in both Q_H and Q_E, which was consistent with the block ensemble average and Hovmøller diagrams of mesoscale fluxes.

Both patterns from the Hovmøller diagram and wavelet analysis showed the positive or negative mesoscale fluxes. However, they did not actually show what contributes to these fluxes. For the turbulent fluxes, the quadrant analysis can be used by dividing the instantaneous contribution into four quadrants (Shaw, 1985). Since the results from the block ensemble average, Hovmøller diagrams of mesoscale fluxes and wavelet analysis suggested that the main contribution for closing the energy balance were mesoscale fluxes, the principle of quadrant analysis was adopted and applied to the mesoscale fluxes $\tilde{w}\tilde{c}$. Let $\tilde{T}$ (temperature) and $\tilde{a}$ (absolute humidity) to be the abscissa and $\tilde{w}$ (vertical velocity) to be the ordinate, the four quadrants $(Q_i, i = 1, ..., 4)$ are

Q_1**:** $\tilde{w} > 0$ and $\tilde{T} > 0$ or $\tilde{a} > 0$ warm air rising or moist air rising,

Q_2**:** $\tilde{w} > 0$ and $\tilde{T} < 0$ or $\tilde{a} < 0$ cold air rising or dry air rising,

Q_3**:** $\tilde{w} < 0$ and $\tilde{T} < 0$ or $\tilde{a} < 0$ cold air sinking or dry air sinking,

Q_4**:** $\tilde{w} < 0$ and $\tilde{T} > 0$ or $\tilde{a} > 0$ warm air sinking or moist air sinking.

Q_1 and Q_3 contribute to the positive flux, while Q_2 and Q_4 contribute to the negative flux. The abscissa and ordinate were then normalized by their standard deviations. The hyperbolic hole of size 0.5 ($H = 0.5$) was set to classify the strength of the contribution. Any points inside this hole weakly contributed to the mesoscale fluxes and could be neglected. Therefore, points with significant contribution outside the hyperbolic hole must satisfy

$$\left| \frac{\tilde{w}\tilde{T}}{\sigma_{\tilde{w}}\sigma_{\tilde{T}}} \right| \text{ or } \left| \frac{\tilde{w}\tilde{a}}{\sigma_{\tilde{w}}\sigma_{\tilde{a}}} \right| > H. \tag{4.14}$$

With the quadrant analysis, contributions of the mesoscale fluxes were expected to be identified. To be conformed with the Hovmøller diagram (Fig. 4.4 and 4.5), the same long period NP, which is 20 May 2003 12:00 UTC - 18 June 2003 00:00 UTC, and $P = 30$ minutes (non-overlapped) were used. Therefore, any points on the quadrant analysis diagram represented the normalized $\tilde{w}\tilde{c}$ from each non-overlapped 30-minute period.

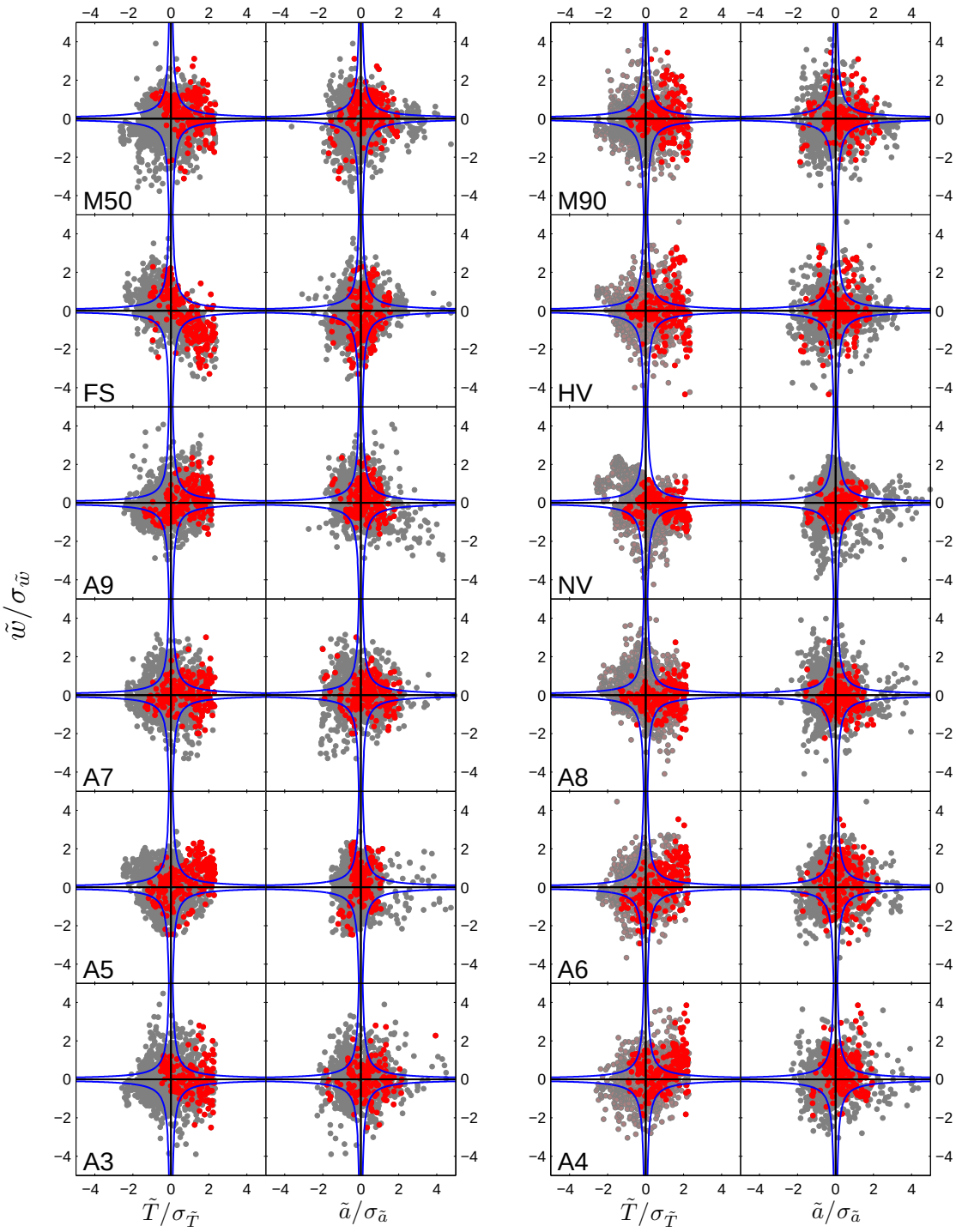

Figure 4.9: Quadrant analysis of the mesoscale flux evaluated using data from EC towers of the LITFASS-2003 experiment during 20 May 2003 12:00 UTC - 18 June 2003 00:00 UTC. Each dot represents the normalized mesoscale flux of each 30-minute block, in which the period from 1 June 2003 15:00 UTC to 5 June 2003 15:00 UTC is highlighted using red dots. The blue solid lines represent the hyperbolic hole (H = 0.5)

The results of the quadrant analysis of all stations are shown in Fig. 4.9. In these diagrams, all points during 1 June 2003 15:00 UTC - 5 June 2003 15:00 UTC are distinguished from the rest by the red color dots. By considering only strong contribution outside a hyperbolic hole (blue line), it was found that during this period, $\tilde{Q}_H$ (via $\tilde{w}\tilde{T}$) had more contribution from Q_1 (warm air rising) for A4 (maize), A5 (rye) and A6 (maize), while there was more contribution from Q_4 (warm air sinking) for NV (grass) and FS (lake). The cancellation between Q_1 and Q_4 were found for the rest of the ground-based stations. For $\tilde{Q}_e$ (via $\tilde{w}\tilde{a}$), significant contribution outside the hyperbolic hole was not found in most ground-based stations. These results implied that the increase of $\langle Q_H \rangle$ at longer P in A4 (maize), A5 (rye) and A6 (maize) were caused by warm air near the surface rising, while the decrease of $\langle Q_H \rangle$ in NV and FS were caused by warm air aloft sinking. When significant contribution from two opposite sign quadrants was found, their cancellation kept the vertical fluxes constant and only a weak inflection was found at the diurnal scale. For M50 (50 m) and M90 (90 m), even their block ensemble average fluxes did change significantly at longer P, it was very difficult to judge that which specific quadrant significantly contribute to the vertical flux. Since both of them were outside the ASL and always experienced SC, their mesoscale contribution might not behave similarly to the ground-based measurement.

4.3 Energy balance correction

All the findings in section 4.2.2 4.2.3 suggest that without assuming steady state condition, the block ensemble average can extend the averaging time to several days, by including the period to period fluctuations or mesoscale fluxes ($\tilde{w}\tilde{c}$) into the mean vertical flux. However, the increased fluxes are not always enough to close the energy balance. With the assistant of the Hovmøller diagram, which shows variation of mesoscale fluxes over long period, the period when SC exist in the vicinity of the sensor can be uncovered by exhibiting consecutive large mesoscale fluxes. This implies that when SC exist near the earth's surface, they mainly transport the sensible heat, which supports the poor scalar similarity between the sensible and latent heat fluxes in the low frequency region (Foken et al., 2011; Ruppert et al., 2006).

Since SC move very slowly and are very large in size, an EC tower measurement averaging over 30 minutes is unable to detect them. If the sensor is coincidentally at the right time and spot, when SC transport near-ground warm air upward, positive

contributions from $\tilde{Q}_H$ would yield higher $\langle Q_H \rangle$ over long period that can improve the energy balance closure. However, when these near-surface SC transport warm air aloft downward, their negative contribution of $\tilde{Q}_H$ would decrease $\langle Q_H \rangle$ at longer averaging time. This suggests that near-surface SC are responsible for the energy balance closure problem rather than the sensor efficiency.

To account for low frequency turbulent fluxes caused by SC, it must be accepted that the scalar similarity between the sensible and latent heat fluxes is no longer valid throughout all scales. Therefore, the widely used energy balance correction in Twine et al. (2000), EBC-Bo, which assumes the scalar similarity between sensible and latent heat fluxes by preserving the Bowen ratio would not generally hold. As near-surface SC transport more sensible heat, EBC-Bo may attribute less residual to the sensible heat flux than expected. This leads to an alternative energy balance correction through the buoyancy flux ratio (EBC-HB), in which the convection play a key role. The buoyancy flux, Q_B, is defined as

$$Q_B = \rho c_p \, \overline{w' T_v'}, \tag{4.15}$$

where ρ is the air density. c_p is the specific heat capacity of air at constant pressure. T_v is the virtual temperature, which can be replaced by the sonic temperature (T_S) with negligible loss of accuracy (Kaimal and Gaynor, 1991). This means that Q_B can be directly measured with a good accuracy by the sonic anemometers. The virtual temperature is related to the actual temperature (T) and specific humidity (q) in the same way as the sonic temperature (Schotanus et al., 1983), which leads to

$$\begin{aligned} Q_B = \rho c_p \, \overline{w' T_v'} &= \rho c_p \, \left(\overline{w' T'} + 0.61 \, \overline{T} \, \overline{w' q'} \right) \\ &= Q_H \, \left(1 + 0.61 \, \overline{T} \, \frac{c_p}{\lambda \, Bo} \right), \end{aligned} \tag{4.16}$$

where λ is the heat of evaporation of water and Bo is the Bowen ratio. The residual can be partitioned with EBC-HB, which contains both sensible and latent heat fluxes. A fraction of the residual, which would attribute to the sensible heat flux is dependent on the relative contribution of the sensible heat flux to the buoyancy flux, while the remaining go to the latent heat flux. Therefore the corrected sensible and latent heat fluxes with EBC-HB ($Q_H^{\mathrm{EBC-HB}}$ and $Q_E^{\mathrm{EBC-HB}}$ respectively) are,

$$Q_H^{\mathrm{EBC-HB}} = Q_H + f_{HB} \cdot Res, \tag{4.17}$$

$$Q_E^{\mathrm{EBC-HB}} = Q_E + (1 - f_{HB}) \cdot Res, \tag{4.18}$$

with

$$f_{HB} = \frac{Q_H}{Q_B} = \left(1 + 0.61\,\overline{T}\,\frac{c_p}{\lambda\,Bo}\right)^{-1}. \tag{4.19}$$

Since this method does not preserve the Bowen ratio, thus Eq. 4.17-4.19 must be calculated iteratively until the Bowen ratio in the Eq. 4.19 converges. The comparison between EBC-Bo and EBC-HB is shown in the Fig. 4.10. Both approaches are identical at very high Bowen ratio, in which all the residual is shifted to the sensible heat flux. For the typical range of Bowen ratio, however, EBC-HB attributes larger fraction of the residual to the sensible heat flux than that by EBC-Bo. This is more consistent with the findings in this chapter.

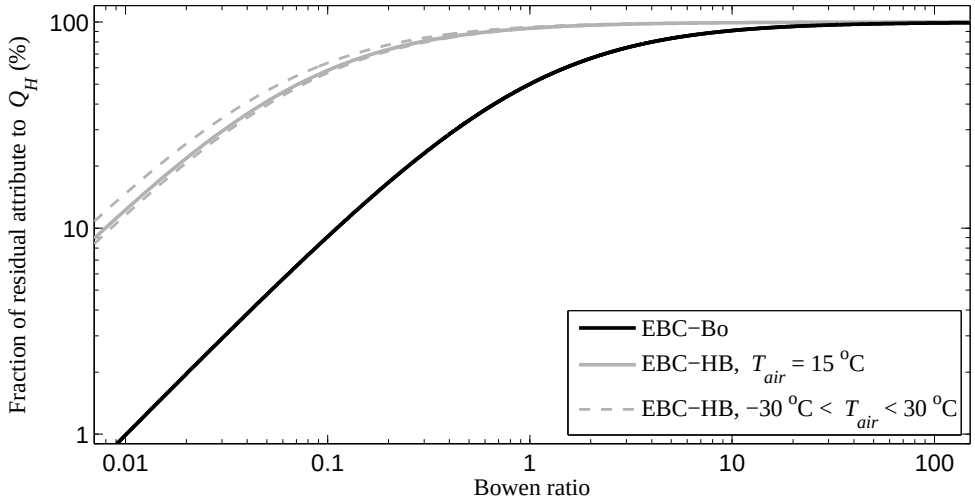

Figure 4.10: Fraction of the residual attributed to the sensible heat flux at different Bowen ratios evaluated from two different approaches. The Bowen ratio approach (EBC-Bo, black line) assumes the scalar similarity between the sensible and latent heat fluxes by preserving the Bowen ratio (Twine et al., 2000). The buoyancy flux ratio approach (EBC-HB, gray lines) partitions the residual according to the ratio between the sensible heat flux and the buoyancy flux, and is shown at different temperatures from -30°C to 30°C. Even both approaches are identical at very large Bowen ratio, EBC-HB mostly attributes larger fraction of the residual to the sensible heat flux than that by EBC-Bo

5

Spatial average

In this chapter, to prove whether the energy balance correction (chapter 4) could properly include contributions from secondary circulations, the energy balance correction was applied on area-averaged fluxes (or composite fluxes), which were aggregated from fluxes measured by multiple EC towers in the LITFASS area. These corrected composite fluxes were supposed to include contribution from secondary circulations and expected to be more comparable with the spatial averaged fluxes, which were measured by the Helipod and LAS.

5.1 Spatial measurement

A fixed EC tower measurement, whose turbulent fluxes are obtained through time averaging, has been proven to be effective over the homogeneous surface. With the Taylor's frozen hypothesis (Taylor, 1938), the time averaged fluxes from the EC measurement can also represent spatial averaged fluxes over a limited area surrounding the tower. However, when the terrain becomes more complex, it would reduce the validity of Taylor's frozen hypothesis, so the time averaged fluxes may no longer represent the spatial averaged fluxes (Crawford et al., 1996). Moreover, even the averaging time has been extended, a fixed tower never measures contributions from stationary SC (Mahrt, 2010). This drawback suggests that any measurements that operates on the spatial average basis and can probe through stationary SC become necessity.

The measurement that operate on a spatial average basis, normally collects data at multiple locations (almost) simultaneously. It normally covers the larger area than a fixed-tower measurement. This type of measurement can be measured by either a fixed instruments, a LAS or an array of fixed towers as examples, or sensors on

a moving vehicle, like a tram (Oncley et al., 2009) or an aircraft. All these measurements are expected to included contributions from both moving and stationary SC, which is supported by many literatures. For instance, in Meijninger et al. (2006), spatial averaged fluxes measured by the LAS over the LITFASS area are systematically higher than composite fluxes (section 3.7). Or in Mauder et al. (2008), spatial averaged fluxes from a network of ground-based sensors over agricultural land give additional 50 W m^{-2} in Q_H.

Over the past ten years, many aircraft-based measurements have been conducted and their measured fluxes can be representative in a regional scale (Desjardins et al., 1995). There are many types of aircraft-based measurements performed recently, such as the Helipod (Bange et al., 2002), an Unmanned Aerial Vehicle (Kroonenberg et al., 2012) and a weight-shift microlight aircraft (Metzger et al., 2012). These measurements cannot operate over a long period. Therefore, they rather more compliment to the tower-based measurements than replacement (Desjardins et al., 1997; Mauder et al., 2007a).

For the LITFASS-2003 experiment, there were measurements from the Helipod and LAS available (section 3.3 and 3.4). Their measured fluxes were systematically higher, but broadly agreed with the composite fluxes or area-averaged fluxes estimated from ground-based measurements (section 3.7). These composite fluxes were formulated from 30-minute averaged fluxes of multiple EC towers, which might not include the contribution from SC. From the findings in Chapter 4, the missing contributions from SC can be included by the energy balance corrections either with the Bowen ratio approach (EBC-Bo) or Buoyancy flux ratio approach (EBC-HB). Therefore, two additional set of composite fluxes with EBC-Bo and EBC-HB were created from the original set of composite fluxes (without energy balance correction, NC, section 3.7). Each set of composite fluxes consisted of composite sensible and latent heat fluxes of each land use.

To test whether these new set of composite fluxes could improve the agreement with the fluxes measured by the Helipod and the LAS, additional aggregation strategy was done. This strategy required the source area of the Helipod, which could be estimated by the footprint analysis. In Metzger et al. (2013), the simple parameterizations model of the backward footprint model (Kljun et al., 2004) was used to determine the source area of the aircraft fluxes. In this thesis, the full version of this footprint model, LPDM-B (section 2.6 or Kljun et al., 2002), was used for this task. This investigation would reveal the connection between the spatial averaged fluxes measured by the Helipod and the LAS with the time averaged fluxes, which

were used to determine the composite fluxes in the LITFASS area.

5.2 Surface fluxes aggregation with the footprint model

5.2.1 Helipod

To estimate the surface fluxes that influence the Helipod by the LPDM-B footprint model, artificial towers were put along the Helipod's flight path. Each tower was apart by 300 meter. The measurement height of each tower is the moving average height of the Helipod with the windows size of 3 km. To run the footprint model, input parameters (L, w_*, u_*, z_m, z_i, z_0 and d, section 2.6) of each tower were required. All input parameters, except z_m and z_i, were surface parameters and depend on the source area of each tower. All of them were estimated with the 'tile-approaches' (Hutjes et al., 2010; Mahrt et al., 2001).

Suppose there are multiple land uses in the source area. Each land use has different forcings and contributes differently to the source area. An area-averaged flux of the source area can be estimated from the linear combination from each land use as

$$F = \sum_i A_i \, F_i \ , \tag{5.1}$$

where i indicates the land use, F_i is the flux of each land use and A_i is the weight, which indicating how much each land use contribute to the source area. In Hutjes et al. (2010), A_i is the fractional coverage of each land use in the source area. Since Obukhov length (L) and Deardorff velocity (w_*) depend on the temperature flux, their effective value of the source area can be estimated with the linear weight average in the same way as in Eq. 5.1, in which

$$L_{eff} = \sum_i A_i \, L_i \tag{5.2}$$

$$w_{*,eff} = \sum_i A_i \, w_{*i} \ , \tag{5.3}$$

where L_i and w_{*i} are Obukhov length and Deardorff velocity of each land use respectively.

For effective friction velocity and roughness length, the weight A_i from each land use should remain the same. However, their formulations are non-linear, therefore

their effective values should not be estimated in the same way as in Eq. 5.1. In this thesis, both of them were estimated with the non-linear weight average. For the effective friction velocity, it is (Hasager and Jensen, 1999)

$$u_{*,eff} = \sqrt{\sum_i A_i u_{*i}^2} \ , \tag{5.4}$$

where u_{*i} is friction velocity of each land use. For the effective roughness, it is (Hasager and Jensen, 1999; Taylor, 1987)

$$\ln z_{0eff} = \sum_i A_i \ln z_{0i} \ , \tag{5.5}$$

where z_{0i} is a roughness length of each land use (section 3.6). Same principle was applied to find the effective displacement height as

$$\ln d_{eff} = \sum_i A_i \ln d_i \ , \tag{5.6}$$

where d_i is a displacement height of each land use.

However, this source area of each artificial tower is just vaguely known as some distance upwind from the sensor. Therefore the average flight statistics were extrapolated to the ground to estimate the surface statistics (Fig. 5.1) with

$$Q_{sfc,exp} = \frac{z_i Q(z_m)}{z_i - z_m}, \tag{5.7}$$

where $Q_{sfc,exp}$ is extrapolated surface flux, z_i is boundary layer height, $Q(z_m)$ is the flux measured at the height z_m like $\overline{w'T'}$, Q_H, Q_E. All surface input parameters of the LPDM-B, except z_0 and d, could be determined from the ground extrapolated statistics (Eq. 5.7). Since both selected Helipod flights were mainly on farmland of the eastern part of the LITFASS area, their z_0 and d were calculated with Eq. 5.5 and 5.6 over the eastern part of the LITFASS area. For this calculation, A_i was the fractional coverage of each land use in the eastern part, using the composite roughness and displacement height to represent each land use's value (section 3.6 and 3.7). According to the land use map, there were two land uses without measurements, which were village and unknown agricultural area. Village or residential area consisted of houses, barns and other constructions, which tended to increase the surface friction, therefore surface statistics of village were taken from the forest. For the unknown agricultural area, its surface statistics were taken from the grassland,

because the grassland would be a mean statistics of the farmland.

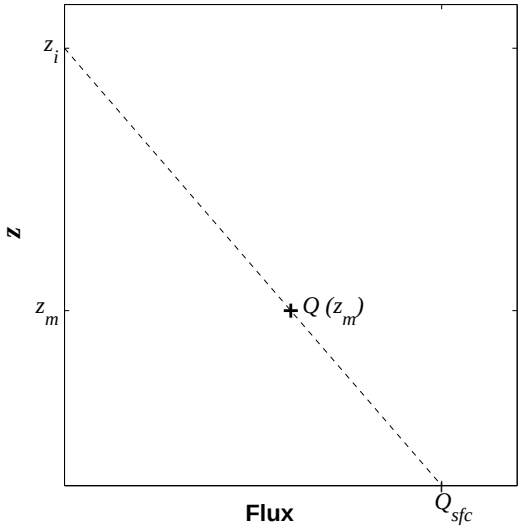

Figure 5.1: The surface flux, Q_{sfc} is determined by extrapolating the flux Q, which is measured at the height z_m, to the surface. Q can be replaced by temperature or scalar fluxes.

For both days of selected Helipod flights (section 3.3), the effective roughness length and displacement height of the eastern part of the LITFASS area were 0.17 m and 1.4 m respectively. Then LPDM-B was run with input parameters at three different height, which are the average height of a whole flight path ($\overline{z_m}$) and $\overline{z_m} \pm 1.5\sigma_z$ (σ_z is a standard deviation of z_m). The contribution of each grid cell (100 m resolution) of the source area to the sensor, which was represent by each element in the source weight matrix, was calculated from Eq. 2.23. With the source weight matrix, the area where 90% of the flux footprint had been reached (Area90) could be identified. For each artificial tower, the touchdown table of closest measurement height was chosen and assumed that only the Area90 influence the measurement. Therefore, the dimension of the original source weight matrix was reduced to cover only Area90. Each element (each grid cell) of this source weight matrix SW is

$$SW_{jk} = \frac{2}{N} \sum_{l}^{n_t} \frac{w_{l0}}{w_l}, \tag{5.8}$$

where N is the total number of particle released from the sensor, index l runs over all particle touchdown in each grid cell, n_t is number of particle touchdown in each grid cell, and w_{l0} and w_l are initial and touchdown velocity of each particle respectively. This source weight matrix was then normalized. Each element in this normalized

source weight matrix SW^{nor} is described as

$$SW_{jk}^{nor} = SW_{jk} \left(\sum_{j,k} SW_{jk} \right)^{-1} \tag{5.9}$$

$$\text{and} \qquad \sum_{j,k} SW_{jk}^{nor} = 1. \tag{5.10}$$

SW^{nor} was imposed to the land use map to determine the fractional contribution from each land use in this Area90. Note that any artificial towers in the very northern or southern parts of the LITFASS area might have some touchdown points outside the land use map. This unknown land use was treated as a grassland. The fractional contributions from each land use were treated as weight A_i in Eq. 5.1, that is

$$A_i = \sum_{j,k} SW_{jk}^{nor} I_{jk}, \tag{5.11}$$

where I_{jk} of each grid cell is one, when this grid cell contains land use i, otherwise is zero. By applying the weight A_i along with the composite quantities of each land use (section 3.6 and 3.7) to Eq. 5.2 - 5.6, the new surface input parameters for LPDM-B for each artificial tower were determined. These new sets of input parameters were used to run LPDM-B and generated a new touchdown table of each artificial tower throughout the entire flight.

In each touchdown table, even the touchdown distance would be as large as 20 km upwind from the sensor, extensive contributions to the sensor is mostly limited to the first few kilometers. Suppose the horizontal wind velocity at the Helipod height is 5 ms^{-1}, each released particle would travel up to 9 km within 30 minutes. In selected Helipod flights, their horizontal velocity were less than 5 ms^{-1}, so it would be safe to follow the upwind distance up to 10 km, at which any touchdown beyond this distance are neglected. The new source weight matrix of each artificial tower was created and normalized to determined the fractional contribution of each land use A_i in the same way as Eq. 5.8 - 5.11. Since each Helipod flight flied much faster than the wind speed, the Taylor's frozen hypothesis would be valid over a few kilometers flight length (Bange et al., 2006b). For each artificial tower, whose statistics were spatially averaged over 5 km length, its spatial averaged fluxes can represent the time averaged fluxes under a steady state condition. Therefore, the surface fluxes as seen by each artificial tower can be determined from Eq. 5.1 with A_i and replacing F_i by the composite fluxes of each land use. These surface sensible and latent heat fluxes (marked with subscript 0 and $footprint$), which determined

from the footprint model , are

$$Q_{H0,footprint} = \sum_i A_i Q_{H,i} \tag{5.12}$$

$$Q_{E0,footprint} = \sum_i A_i Q_{E,i}, \tag{5.13}$$

where $Q_{H,i}$ and $Q_{E,i}$ are the composite sensible and latent heat fluxes of each land use respectively. To compare these surface fluxes with the fluxes measured by the Helipod, the Helipod fluxes must be downscale to the same level. This downscale scheme were done by extrapolated the Helipod fluxes down to the surface in the same way as Eq. 5.7. These surface sensible and latent heat fluxes (marked with subscript 0 and *helipod*), which extrapolated from the Helipod fluxes are

$$Q_{H0,helipod} = \frac{z_i Q_{H,helipod}}{z_i - z_{helipod}} \tag{5.14}$$

$$Q_{E0,helipod} = \frac{z_i Q_{E,helipod}}{z_i - z_{helipod}}, \tag{5.15}$$

where z_i is the boundary layer height, $z_{helipod}$ is the measurement height of the Helipod, and $Q_{H,helipod}$ and $Q_{E,helipod}$ are respectively sensible and latent heat fluxes measured by the Helipod. For the flight on 7 June 2003, it was additionally compared with the fluxes measured by the LAS.

5.2.2 Tower

Similar strategy as in section 5.2.1 also applied to the 30-minute averaged fluxes from M50 and M90 tower. Sensible and latent heat fluxes determined from the footprint model are still the same as in Eq. 5.12 and 5.13, while surface fluxes extrapolated from M50 and M90 are in this form,

$$Q_{H0,tower} = \frac{z_i Q_{H,tower}}{z_i - z_{tower}} \tag{5.16}$$

$$Q_{E0,tower} = \frac{z_i Q_{E,tower}}{z_i - z_{tower}}, \tag{5.17}$$

where $Q_{H0,tower}$ and $Q_{E0,tower}$ are respectively surface sensible and latent heat fluxes extrapolated from the tower (M50 or M90), $Q_{H,tower}$ and $Q_{E,tw}$ are respectively sensible and latent heat fluxes as measured by the tower at the measurement height z_{tower}.

The selected period of interested were restricted to when data from M50, M90,

composite fluxes of all land uses and boundary layer heights are available with good quality. By removing some periods, which had almost identical conditions, only 15 runs are available for the footprint analysis.

5.3 Results and Discussion

5.3.1 Helipod

Most diagrams of Helipod analysis are marked with set of references points (P). Each point represents a specific location on the flight path, which is identical in all diagrams of the same flight. Outline of selected flights and all reference points can be found in Fig. 5.2.

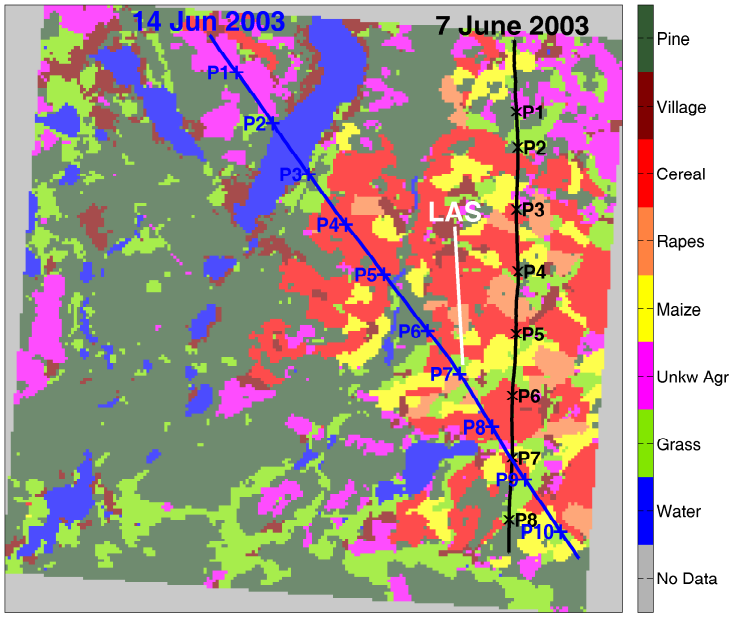

Figure 5.2: Two selected Helipod flight paths as flied on 7 and 14 June 2003. The LAS path over the farmland is also presented. The underlying surface consisted of these following land uses: water (lake), grass, unknown agricultural area (Unkw Agr), maize, rapes, cereal, cereal, village and pine.

Q_H and Q_E along the Helipod flight path are shown in Fig. 5.3. Fluxes estimations along the flight path with the moving average (window size 3 km) broadly agreed with fluxes estimated from the wavelet analysis (section 2.5). This meant that the moving average fluxes could represent instantaneous fluxes as seen by the Helipod. At the beginning and the end of the flight, the measured fluxes might subject to larger error, therefore, these regions should be avoided in all analyses. In

both flights, the regions with minimum Q_H seemed to be coincide with the presence of the lakes upwind of the flight paths. These regions are P5-P8 of Fig. 5.3 a and P2-P4 of Fig. 5.3 b. There were more flux variabilities in Q_H when the Helipod passed over the farmland. For the flight on 7 June 2003, which occurred in between two heavy rain events, its Q_E was averagely larger than that of the flight on 14 June 2003. Moreover, the southern part averagely showed larger Q_E than the northern part of the flight. This was consistent with the rain event on 5 June 2003, which occurred mainly in the southern part of the LITFASS area.

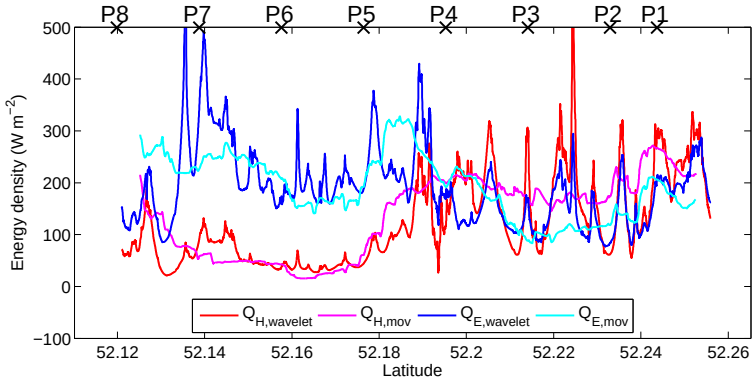

(a) 7 June 2003

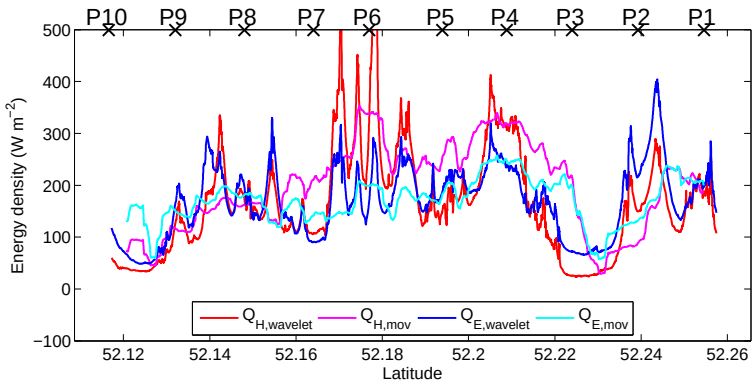

(b) 14 June 2003

Figure 5.3: Sensible and latent heat fluxes, deduced from a wavelet analysis (subscript wavelet) and moving average (windows size = 3 km, subscript mov), of the Helipod flight on a) 7 Jun 2003 14:40 - 13:50 UTC and b) 14 Jun 2003 09:20 - 09:30 UTC. Both estimations broadly agree to each other.

The wavelet analysis of selected flights are shown in Fig. 5.4. There were the absences of the signal in Q_H that coincided with the region of minimum Q_H in both flights. The absences of Q_H in the wavelet analysis are a typical signature of the lake. Eddies, which suddenly disappeared, had Fourier period up to 1 km, which corresponded to the inverse wavenumber of 100-200 m. These would be the scale

of eddies that transported Q_H between the atmosphere at the Helipod's height and the surface below. For the flight on 7 June 2003 (Fig. 5.4 a), these scale of eddies extensively transported Q_E. This indicated that the absence of Q_H over the lake might be rather caused by the missing of the temperature fluctuations. However, for the flight on 14 June 2003 (Fig. 5.4 b), the wavelet analysis showed the absences in both Q_H and Q_E simultaneously. 14 June was comparatively dry with respect to 7 June. This suggested that the existence of Q_E over the lake on 7 June would be caused by the wet air mass after the rain event on 5 June 2003.

Fractional contributions of each land use A_i (Eq. 5.11) along the flight paths, which were estimated from the LPDM-B model, are shown in Fig. 5.5. By using Eq. 5.12 and 5.13, three set of $Q_{H0,footprint}$ and $Q_{E0,footprint}$ were calculated from three types of composite fluxes: NC (green lines), EBC-Bo (blue lines) and EBC-HB (red lines). These three fluxes, which were estimated from the footprint model, were compared with the fluxes extrapolated from the Helipod (5.14 and 5.15, black lines). It was found that they did mostly show the same tendency. This would suggest that surfaces forcings or source areas as predicted by the footprint were acceptable.

$Q_{H0,footprint}$ with EBC-Bo and EBC-HB were consistent very well with $Q_{H0,helipod}$ when the Helipod was over the farmland and forest. For 7 June 2003, the discrepancy between $Q_{H0,footprint}$ and $Q_{H0,helipod}$ was large in the southern part, which can be caused by the presence of the lake and the rain events on 5 June 2003. However, this rain event did not much disturbed the measurement of Q_H in the southern part of the LITFASS area. Hence, the discrepancy between $Q_{H0,footprint}$ and $Q_{H0,helipod}$, which was also found over the lake in the flight on 14 June 2003, should be mainly caused by the lake. This discrepancy might be explained by the internal boundary layer over the lake, whose frictional velocity suddenly drops from the surrounding area. This internal boundary layer might trap all particles beyond this lake. Even the footprint model predicted that there were significant contributions from forest and farmland in this area, their contributions could be neglected, if they were beyond the lake. Since the touchdown table does not contain the detailed trajectory of each particle, it is very difficult to precisely remove the trapped particles. Therefore, it must be reminded that when the source area contains fractional of water or lake, its $Q_{H0,footprint}$ tends to be over estimated. This condition must be considered carefully and suggests that points with significant contribution from the lake should not be included in the comparison.

For Q_E, which was much disturbed by the rain event, its composite fluxes could

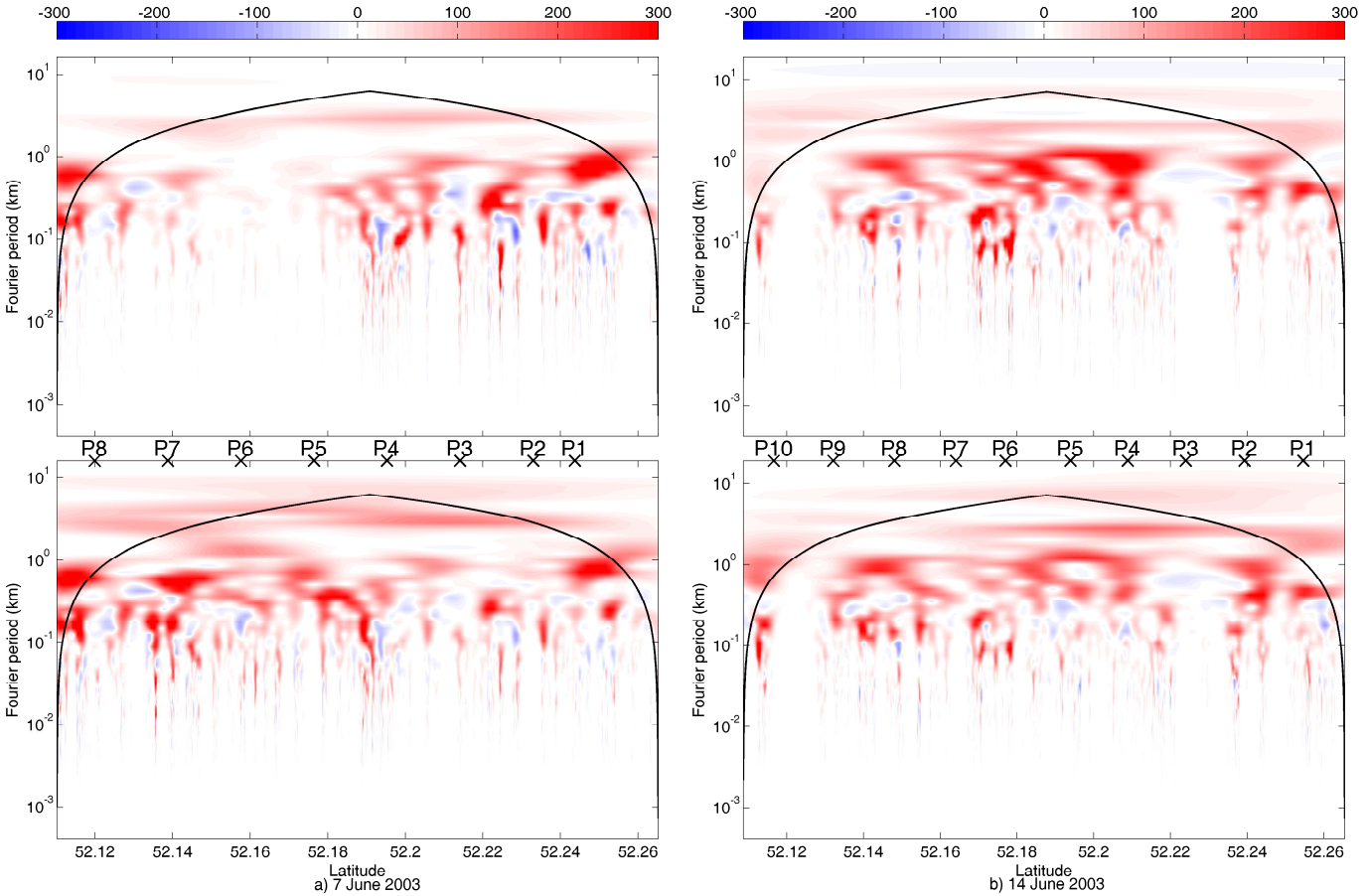

Figure 5.4: Wavelet cross-scalogram of the Helipod flight on a) 7 June 2003 and b) 14 June 2003. The upper panels represent the sensible heat fluxes, while the lower ones represent the latent heat fluxes. Colors represent the value in W m^{-1} and the black solid line is the cone of influence.

be very different from locally measured one. This caused a large discrepancy between $Q_{E0,footprint}$ and $Q_{E0,helipod}$ throughout the entire flight on 7 June 2003. A spatial shift between $Q_{E0,footprint}$ and $Q_{E0,helipod}$ were also clearly observed in both flights. This spatial shift was not obviously shown in Q_H, therefore, it was most likely caused by the scalar similarity between moisture and temperature, which do not hold over the whole frequency range. Hence, small difference would be added up and could be observed at a large observation distance. For the flight on 14 June 2003, which was not disturbed by the rain event, if a spatial shift was taken into account, $Q_{E0,footprint}$ with EBC-Bo over the lake tended to be overestimated, while with EBC-HB and NC tended to be underestimated. Therefore, the discrepancies between $Q_{E0,footprint}$ and $Q_{E0,helipod}$ would be caused by the composite fluxes rather than the presence of the lake.

Table 5.1: The surface fluxes from different estimations within the range that least effect by the lake (bounded by vertical dashed lines in Fig. 5.5). These estimations are: NC = No energy balance correction; EBC-Bo = energy balance correction with Bowen ratio approach; EBC-HB = energy balance correction with buoyancy flux ratio approach; and Helipod - mov = the extrapolation to the surface of moving average fluxes (3km windows) of the Helipod

	7 Jun 2003		14 Jun 2003	
Estimation	Q_{H0}(Wm^{-2})	Q_{E0}(Wm^{-2})	Q_{H0}(Wm^{-2})	Q_{E0}(Wm^{-2})
LPDM-B - NC	122	170	231	140
LPDM-B - EBC-Bo	163	229	305	186
LPDM-B - EBC-HB	215	177	347	144
Helipod - mov	192	191	281	187

To observe how well can the footprint model predict the surface fluxes, only part of the flight that least influence by the presence of the lake should be considered. This region is bounded by the vertical black dashed lines in Fig. 5.5. The average of $Q_{H0,footprint}$, $Q_{E0,footprint}$, $Q_{H0,helipod}$ and $Q_{E0,helipod}$ within this range are shown in Table 5.1 and represented by the horizontal dashed lines in Fig. 5.5 (color codes after the solid lines). For 7 June 2003, a fractional contributions from the lake was pretty low. It was found that $Q_{H0,footprint}$ with EBC-Bo and EBC-HB did equally well and were much better than NC. Since the composite latent heat fluxes of this flight might not a good representative of this flight segment, the comparison between $Q_{E0,footprint}$ and $Q_{E0,helipod}$ would be inconclusive. For 14 June 2003, the bounded region was a little bit disturbed by the presence of the lake, which suggested that $Q_{H0,footprint}$ could be overestimated. By taking this issue into account, it can be concluded that $Q_{H0,footprint}$ with EBC-Bo and EBC-HB did equally well and were much better than NC as well. For $Q_{E0,helipod}$, it was best fit with $Q_{E0,footprint}$ with EBC-Bo. However when the spatial shift was considered, average $Q_{E0,helipod}$ of this

flight segment should be lower than estimated. Therefore, $Q_{E0,footprint}$ with EBC-HB and NC were acceptable as well.

One more thing that may need to be considered is that the Helipod measurement height was clearly not in the ASL and would be in different similarity scaling domain. According to the time average analysis (chapter 4), both sensible and latent heat fluxes significantly change at long block ensemble averaging period in M50 and M90 (measured fluxes at 50 m and 90 m heights respectively). This implies that large scale eddies, which transport the energy at these heights, may not behave similarly to the ones near the earth's surface and tend to preserve the Bowen ratio. Therefore, the extrapolation to the surface from these measurement heights may fit better with the surface fluxes estimated with EBC-Bo. To get rid of this ambiguity, the spatial average measurements conducted near the earth's surface are needed.

Part of the flight on 7 June 2003 was right above the LAS path over the farmland (section 3.4 and Fig. 5.2). The source areas of this Helipod's segment and the LAS should not be much different, in which both measured sensible fluxes would be comparable. The comparison between sensible heat fluxes measured from this Helipod segment, measured by the LAS, and estimated from the footprint model is shown in Fig. 5.6. For the entire flight on 7 June 2003, the measurement error of the sensible heat flux was around 33 W m^{-2} and the measurement error for the flight segment above the LAS should be not much different. Sensible heat flux, which was measured over this flight segment, was $Q_{H,helipod}$ =166 W m^{-2} (upper black circle). Its extrapolation down to the surface was $Q_{H0,helipod}$ = 175 W m^{-2} (lower black circle). The surface sensible heat flux deduced from the LAS was $Q_{H0,LAS}$ = 171 W m^{-2} and represented by blue diamond. It was actually within the measurement error of the Helipod. All surface fluxes estimated from the footprint model are represented by the red symbols. $Q_{H0,helipod}$ and $Q_{H0,LAS}$ seemed to be best fit with $Q_{H0,footprint}$ with EBC-Bo (156 W m^{-2}). Nevertheless, they were also in good agreement with $Q_{H0,footprint}$ with EBC-HB (208 W m^{-2}). Moreover, the southern part of this flight segment had small contribution from the lake, which implied that all sets of $Q_{H0,footprint}$ would be slightly overestimated. When this issue was taken into account, all footprint estimated fluxes (all red symbol), should be a little bit shifted to the left. This would lead to the same conclusion earlier that both EBC-Bo and EBC-HB are equally good for predicting the surface sensible heat flux by the footprint model and they are much better than no energy balance correction at all.

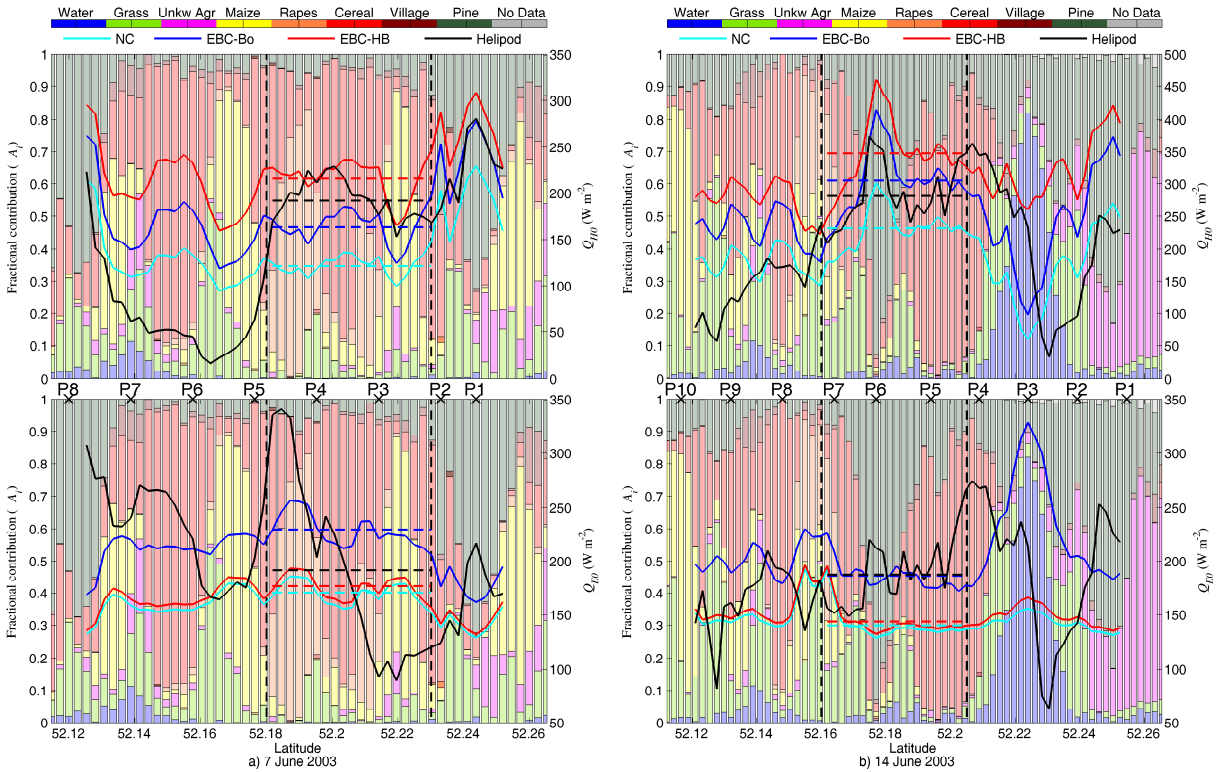

Figure 5.5: The comparison between the surface fluxes estimated from the footprint model and extrapolated fluxes from the Helipod (black). The footprint estimated surface fluxes were calculated from three types of composite fluxes, without energy balance correction (green), with EBC-Bo (blue) and with EBC-HB (red). Part of the flight that least influence by the presence of the lake are bounded by the vertical black dashed lines

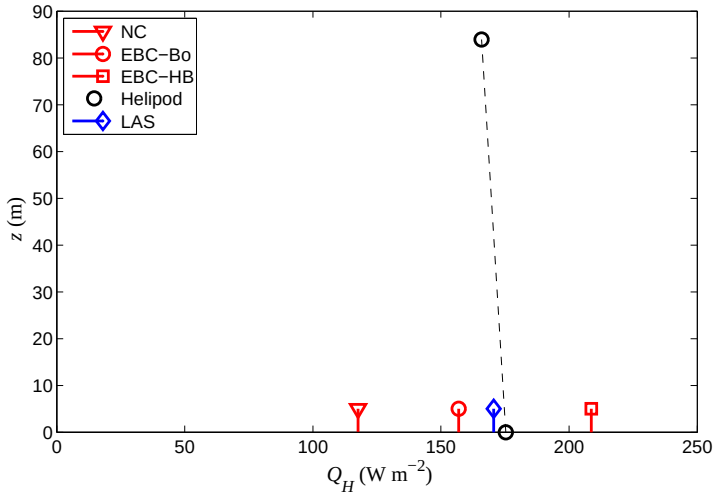

Figure 5.6: This diagram shows the comparison of surface fluxes on 7 June 2003, which was estimated from the flight segment above the LAS path over the farmland. The black circles represent sensible heat fluxes as measured by the Helipod (upper) and extrapolated to the surface (lower). All red symbols represent surface sensible heat fluxes estimated from the footprint model with no energy balance correction (triangle), EBC-Bo (circle) and EBC-HB (square). The blue diamond represents surface fluxes estimated from the LAS.

5.3.2 Tower

Three sets of surface fluxes estimated with the LPDM-B model were created in the same way as Eq. 5.12 and 5.13 for all selected 30-minute runs of M50 and M90. The comparisons of these fluxes with the surface fluxes extrapolated from the tower (Eq. 5.16 and 5.17) are shown in Fig. 5.7. Unlike the Helipod, $Q_{H0,tower}$ was best fit by $Q_{H0,footprint}$ with no energy balance correction, while $Q_{E0,tower}$ was equally good for all three sets of $Q_{E0,footprint}$. From the time average analysis (chapter 4), it was shown that both M50 and M90 normally experienced SC. However, within 30 minutes contributions from SC were not yet fully included. Therefore, the measured fluxes should be more comparable to the uncorrected fluxes. Additionally, at these two measurement heights, the steady state conditions or homogeneous conditions might no longer hold. This means their time averaged statistics could represent neither time-averaged nor spatial-averaged statistics of the source area and the relation with the composite fluxes as in Eq. 5.1 might not be applicable.

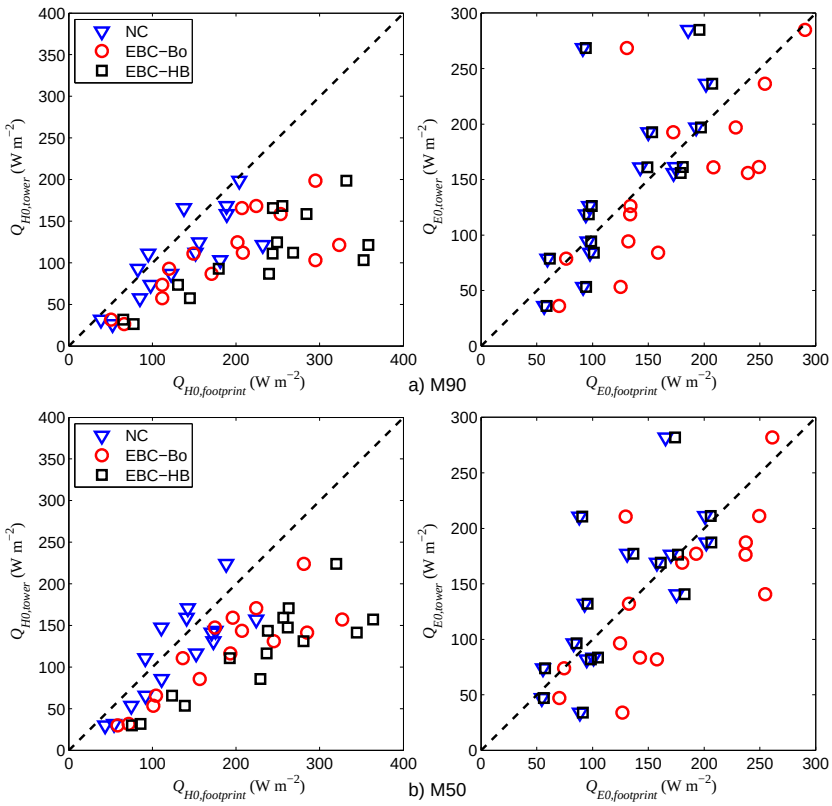

Figure 5.7: The comparison between the footprint surface fluxes and the surface fluxes extrapolated from M50 and M90 tower.

6

Conclusions

In this thesis, data from the LITFASS-2003 experiment was analyzed to study the energy balance closure problem at the earth's surface, which has been believed to be caused by the secondary circulations. The analysis was carried out in both time and space domains, from which several conclusions were drawn.

The time domain analysis mainly involved data from ground-based eddy-covariance towers, whose representative statistics were time-averaged statistics. To increase the possibility that secondary circulations were picked up by the sensor, the eddy-covariance averaging time was extended beyond a typical value of 30 minutes. This time extension strategy was accomplished through the ogive analysis (Desjardins et al., 1989; Oncley et al., 1990) and the block ensemble average (Finnigan et al., 2003).

The ogive analysis requires a steady state condition, restricting the time extension to only a few hours. In this thesis, the modified ogive analysis was formulated to deal with low frequency data, which allowed the investigation to include low frequency data from all available ground-based stations. Employed this approach, it was found that an averaging time extension up to four hours would not significantly improve the energy balance closure in all ground-based stations. The time extension, moreover, had more impact over tall vegetation. Sensible heat flux, latent heat flux and CO_2 flux were more sensitive to the time extension than friction velocity. Over low vegetation, the increase of these three turbulent fluxes with the time extension was related to the unsteadiness of the longer averaging period. The increase of the sensible heat flux was overall higher compared to one of the latent heat flux. Over a longer period, the increase or decrease of sensible and latent heat fluxes might not change proportionally as expected. For 4-hour averaging time in low vegetation, the sensible heat flux averagely increased by 15 - 45W m^{-2}, while the latent heat

flux averagely increased by 10 - 25 W m^{-2}. These amount of energy increased were not overall enough to close the energy balance in all low vegetation measurements of the LITFASS-2003 experiment. Therefore, the 30-minute averaging time is still sufficient for the eddy-covariance measurement over low vegetation.

The block ensemble average, which does not require a steady state condition, can extend the averaging time to several days by including period to period fluctuations or mesoscale fluxes ($\tilde{w}\tilde{c}$) to the mean vertical flux. These mesoscale fluxes indeed include low frequency contribution not only from secondary circulations, but also from other large scale events (for example a synoptic scale event). It was shown from the LITFASS-2003 data that there existed large scale eddies, which were believed to be secondary circulations, near the earth's surface. During the period between 1 June 2003 to 5 June 2003, when secondary circulations existed in the vicinity of the sensor and were not influenced by other large scale events, consecutive large mesoscale fluxes of temperature ($\tilde{w}\tilde{T}$) were found through the Hovmøller diagrams of mesoscale fluxes. During this period, the wavelet analysis suggested that these near-surface secondary circulations spanned a time and a spatial extension of 4-5 hours and 30-40 km respectively. Additionally the quadrant analysis of mesoscale fluxes in this period showed that positive contribution of the large mesoscale fluxes was mainly from the first quadrant, in which near-ground warm air was transported upward, while the negative contribution was mainly from the forth quadrant, in which warm air aloft was transported downward. These findings implied that secondary circulations near the earth's surface mainly transported sensible heat and led to an alternative energy balance correction with the buoyancy flux ratio approach. With this energy balance correction approach, the attribution of the residual depends on the relative contribution of the sensible heat flux to the buoyancy flux. Fraction of the residual attributed to the sensible heat flux by this energy balance correction is larger than in the energy balance correction that preserves the Bowen ratio. It was also found that at the high measurement height, which was probably outside the atmospheric surface layer, large scale eddies seemed to transport sensible and latent heat equally. This then suggested that large scale eddies in different similarity scaling domain might behave differently. Thus, to further investigate this aspect, appropriate experiments are needed in the future.

For the space domain analysis, the energy balance correction with the buoyancy flux ratio approach was validated with application to the area-averaged or composite fluxes (Beyrich et al., 2006). These composite fluxes were aggregated from time averaged fluxes of multiple eddy-covariance towers. When the contribution

from secondary circulations was included, these area-averaged fluxes were expected to be more comparable with the spatial-averaged fluxes as measured by the Helipod and a Large Aperture Scintillometer. These spatial average measurements then could include contribution from both stationary and slow moving secondary circulations, whose measured fluxes were normally larger than ones measured by an eddy-covariance tower (fixed tower). The validation process was assisted by the backward Lagrangian dispersion particle footprint model (LPDM-B, Kljun et al., 2002), which could effectively estimate the source area of the measurement. However, to estimate the surface fluxes correctly, the representative composite fluxes were needed. Under the conditions when extreme flux variability was found in the larger area, the composite fluxes could be very different from the locally measured fluxes. This could make the composite fluxes to be unsuitable to couple with the footprint model in order to estimate surface fluxes over some specific area. Moreover, the presence of the lake in the source area could limit the validity of the footprint model and caused the predicted surface fluxes to be over-estimated. Therefore, careful consideration must be made when this issue arises. Eventually, when the composite fluxes were representative and least disturbed by the presence of the lake, it was found that the energy balance correction with the buoyancy flux ratio approach and the Bowen ratio approach could significantly improve the agreement between the composite fluxes (time average) and spatial averaged fluxes, especially for the sensible heat flux. This then suggests that in order to include contribution from secondary circulations into a fixed tower measurement (time average), the energy balance correction is necessary. However, to justify whether which energy balance correction approach is more appropriate, spatial average measurements near the earth's surface are needed.

All the findings in both time and spatial averages analyses suggest that there exist large scale structures with a large spatial extension (about 30-40 km) near the earth's surface, that also significantly transport energy in the atmospheric surface layer. These large scale structures are relatively stationary and believed to be the secondary circulations, which are normally outside the atmospheric surface layer. Therefore, a single point flux measurement in the atmospheric surface layer within a typical time interval of 30 minutes mostly misses contribution from secondary circulations and causes the energy balance unable to be closed. To estimate the actual vertical transport of energy in the atmospheric surface layer, fluxes measured by a single point need to be corrected. It was also found that when secondary circulations existed in the vicinity of the sensor, they mainly affected the mesoscale flux of the sensible heat at the long averaging period. This finding implies that

near-surface secondary circulations mainly transport sensible heat and, therefore, are appropriate to correct mainly the sensible heat flux. Hence, the energy balance correction approach, which has been consistent with all the findings and is proved to be effective in this thesis, is the energy balance correction with buoyancy flux ratio approach, because it attributes larger fraction for the residual to the sensible heat flux than in the energy balance correction that preserves the Bowen ratio.

Bibliography

Aubinet M, Vesala T, Papale D (eds) (2012) Eddy Covariance A Practical Guide to Measurement and Data Analysis. Springer, Dordrecht

Baldocchi D, Falge E, Gu L, Olson R, Hollinger D, Running S, Anthoni P, Bernhofer C, Davis K, Evans R, Fuentes J, Goldstein A, Katul G, Law B, Lee X, Malhi Y, Meyers T, Munger W, Oechel W, Paw KT, Pilegaard K, Schmid HP, Valentini R, Verma S, Vesala T, Wilson K, Wofsy S (2001) FLUXNET: A new tool to study the temporal and spatial variability of ecosystem-scale carbon dioxide, water vapor, and energy flux densities. Bulletin of the American Meteorological Society 82(11):2415–2434

Bange J, Roth R (1999) Helicopter-borne flux measurements in the nocturnal boundary layer over land - A case study. Boundary-Layer Meteorology 92:295–325

Bange J, Beyrich F, Engelbart DAM (2002) Airborne measurements of turbulent fluxes during LITFASS-98: Comparison with ground measurements and remote sensing in a case study. Theoretical and Applied Climatology 73:35–51

Bange J, Spieß T, Herold M, Beyrich F, Hennemuth B (2006a) Turbulent fluxes from helipod flights above quasi-homogeneous patches within the LITFASS area. Boundary-Layer Meteorology 121:127–151

Bange J, Zittel P, Spieß T, Uhlenbrock J, Beyrich F (2006b) A new method for the determination of area-averaged turbulent surface fluxes from low-level flights using inverse models. Boundary-Layer Meteorology 119:527–561

Bernstein AB (1966) Examination of certain terms appearing in Reynolds' equations under unsteady conditions and their implications for micrometeorology. Quarterly Journal of the Royal Meteorological Society 92:533–542

Bernstein AB (1970) The calculation of turbulent fluxes in unsteady conditions. Quarterly Journal of the Royal Meteorological Society 96:762–762

Beyrich F, Leps JP (2012) An operational mixing height data set from routine radiosoundings at Lindenberg: Methodology. Meteorologische Zeitschrift 21:337–348

Beyrich F, Mengelkamp HT (2006) Evaporation over a heterogeneous land surface: EVA_GRIPS and the LITFASS-2003 experiment—an overview. Boundary-Layer Meteorology 121:5–32

Beyrich F, Adam WK, Bange J, Behrens K, Berger FH, Bernhofer C, Bösenberg J, Dier H, Foken T, Göckede M, Görsdorf U, Güldner J, Hennemuth B, Heret C, Huneke S, Kohsiek W, Lammert A, Lehmann V, Leiterer U, Leps JP, Liebethal C, Lohse H, Lüdi A, Mauder M, Meijninger WM, Mengelkamp HT, Queck R, Richter SH, Spieß T, Stiller B, Tittebrand A, Weisensee U, Zittel P (2004) Verdunstung über einer heterogenen Landoberfläche: Das LITFASS-2003 Experiment. No. 79 in Arbeitsergebnisse, Deutscher Wetterdienst Forschung und Entwicklung

Beyrich F, Leps J, Mauder M, Bange J, Foken T, Huneke S, Lohse H, Lüdi A, Meijninger WML, Mironov D, Weisensee U, Zittel P (2006) Area-averaged surface fluxes over the LITFASS region based on eddy-covariance measurements. Boundary-Layer Meteorology 121:33–66

Charuchittipan D, Babel W, Mauder M, Leps JP, Foken T (2013) Extension of the averaging time of the eddy-covariance measurement and its effect on the energy balance closure. Boundary-Layer Meteorology submitted

Crawford TL, Dobosy RJ, McMillen RT, Vogel CA, Hicks BB (1996) Air-surface exchange measurement in heterogeneous regions: extending tower observations with spatial structure observed from small aircraft. Global Change Biology 2:275–285

Desjardins RL, MacPherson JI, Schuepp PH, Karanja F (1989) An evaluation of aircraft flux measurements of CO_2, water vapor and sensible heat. Boundary-Layer Meteorology 47:55–69

Desjardins RL, Macpherson JI, Neumann H, Hartog GD, Schuepp PH (1995) Flux estimates of latent and sensible heat, carbon dioxide, and ozone using an aircraft-tower combination. Atmospheric Environment 29:3147–3158

Desjardins RL, MacPherson JI, Mahrt L, Schuepp P, Pattey E, Neumann H, Baldocchi D, Wofsy S, Fitzjarrald D, McCaughey H, Joiner DW (1997) Scaling up

flux measurements for the boreal forest using aircraft-tower combinations. Journal of Geophysical Research 102:D29,125–29,133

Eigenmann R, Metzger S, Foken T (2009) Generation of free convection due to changes of the local circulation system. Atmospheric Chemistry and Physics 9:8587–8600

de Feriet JK (1951) Average processes and Reynolds equations in atmospheric turbulence. Journal of Meteorology 8:358–361

Finnigan JJ, Clement R, Malhi Y, Leuning R, Cleugh H (2003) A re-evaluation of long-term flux measurement techniques part I: Averaging and coordinate rotation. Boundary-Layer Meteorology 107:1–48

Flesch TK (1996) The footprint for flux measurements, from backward Lagrangian stochastic models. Boundary-Layer Meteorology 78:399–404

Foken T (2008a) The energy balance closure problem: An overview. Ecological Applications 18:1351–1367

Foken T (2008b) Micrometeorology. Springer-Verlag, Berlin Heidelberg

Foken T, Wichura B (1996) Tools for quality assessment of surface-based flux measurements. Agricultural and Forest Meteorology 78:83–05

Foken T, Göockede M, Mauder M, Mahrt L, Amiro B, Munger W (2004) Post-field data quality control. In: Lee X, Massman W, Law B (eds) Handbook of Micrometeorology, Kluwer Academic Publishers, Dordrecht, pp 181–208

Foken T, Wimmer F, Mauder M, Thomas C, Liebethal C (2006) Some aspects of the energy balance closure problem. Atmospheric Chemistry and Physics 6:4395–4402

Foken T, Mauder M, Liebethal C, Wimmer F, Beyrich F, Leps JP, Raasch S, DeBruin H, Meijninger W, Bange J (2010) Energy balance closure for the LITFASS-2003 experiment. Theoretical and Applied Climatology 101:149–160

Foken T, Aubinet M, Finnigan JJ, Leclerc MY, Mauder M, Paw U KT (2011) Results of a panel discussion about the energy balance closure correction for trace gases. Bulletin of the American Meteorological Society 92:ES13–ES18

Foken T, Leuning R, Oncley SR, Mauder M, Aubinet M (2012) Corrections and data quality control. In: Aubinet M, Vesala T, Papale D (eds) Eddy Covariance, Springer, Dordrecht, pp 85–131

Hasager CB, Jensen NO (1999) Surface-flux aggregation in heterogeneous terrain. Quarterly Journal of the Royal Meteorological Society 125:2075–2102

Haverd V, Cuntz M, Leuning R, Keith H (2007) Air and biomass heat storage fluxes in a forest canopy: Calculation within a soil vegetation atmosphere transfer model. Agricultural and Forest Meteorology 147:125–139

Hollinger DY, Richardson AD (2005) Uncertainty in eddy covariance measurements and its application to physiological models. Tree Physiology 25:873–885

Hutjes R, Vellinga O, Gioli B, Miglietta F (2010) Dis-aggregation of airborne flux measurements using footprint analysis. Agricultural and Forest Meteorology 150:966–983

Inagaki A, Letzel MO, Raasch S, Kanda M (2006) Impact of surface heterogeneity on energy imbalance: A study using LES. Journal of the Meteorological Society of Japan 84:187–198

Kaimal JC, Finnigan JJ (1994) Atmospheric boundary layer flows: their structure and measurement. Oxford University Press

Kaimal JC, Gaynor JE (1991) Another look at sonic thermometry. Boundary-Layer Meteorology 56:401–410

Kaimal JC, Wyngaard JC, Izumi Y, Cote OR (1972) Spectral characteristics of surface-layer turbulence. Quarterly Journal of the Royal Meteorological Society 98:563–589

Kanda M, Inagaki A, Letzel MO, Raasch S, Watanabe T (2004) LES study of the energy imbalance problem with eddy covariance fluxes. Boundary-Layer Meteorology 110:381–404

Kljun N, MWRotach, Schmid H (2002) A three-dimensional backward Lagrangian footprint model for a wide range of boundary-layer stratifications. Boundary-Layer Meteorology 103:205–226

Kljun N, Calanca P, Rotach M, Schmid H (2004) A simple parameterisation for flux footprint predictions. Boundary-Layer Meteorology 112:503–523

Kohsiek W, Liebethal C, Foken T, Vogt R, Oncley S, Bernhofer C, Debruin H (2007) The energy balance experiment EBEX-2000. part III: Behaviour and quality of the radiation measurements. Boundary-Layer Meteorology 123:55–75

Kroonenberg A, Martin S, Beyrich F, Bange J (2012) Spatially-averaged temperature structure parameter over a heterogeneous surface measured by an unmanned aerial vehicle. Boundary-Layer Meteorology 142:55–77

Lenschow DH, Stankov BB (1986) Length scales in the convective boundary layer. Journal of the Atmospheric Sciences 43(12):1198–1209

Lenschow DH, Mann J, Kristensen L (1994) How long is long enough when measuring fluxes and other turbulence statistics? Journal of Atmospheric and Oceanic Technology 11:661–673

Leuning R, van Gorsel E, Massman WJ, Isaac PR (2012) Reflections on the surface energy imbalance problem. Agricultural and Forest Meteorology 156:65 –74

Liebethal C, Huwe B, Foken T (2005) Sensitivity analysis for two ground heat flux calculation approaches. Agricultural and Forest Meteorology 132:253–262

Lindroth A, Mölder M, Lagergren F (2010) Heat storage in forest biomass improves energy balance closure. Biogeosciences 7:301–313

Mahrt L (2010) Computing turbulent fluxes near the surface: Needed improvements. Agricultural and Forest Meteorology 150:501–509

Mahrt L, Vickers D, Sun J, McCaughey JH (2001) Calculation of area-averaged fluxes: Application to BOREAS. Journal of Applied Meteorology 40:915–920

Markkanen T, Steinfeld G, Kljun N, Raasch S, Foken T (2009) Comparison of conventional Lagrangian stochastic footprint models against LES driven footprint estimates. Atmospheric Chemistry and Physics 9:5575–5586

Martano P (2000) Estimation of surface roughness length and displacement height from single-level sonic anemometer data. Journal of Applied Meteorology 39:708–715

Massman WJ, Lee X (2002) Eddy covariance flux corrections and uncertainties in long-term studies of carbon and energy exchanges. Agricultural and Forest Meteorology 113:121–144

Mauder M, Foken T (2004) Documentation and instruction manual of the eddy covariance software package TK2. No. 26 in Arbeitsergebnisse, University of Bayreuth, Department of Micrometeorology, URL http://opus.ub.uni-bayreuth.de/opus4-ubbayreuth/frontdoor/index/index/docId/639

Mauder M, Foken T (2006) Impact of post-field data processing on eddy covariance flux estimates and energy balance closure. Meteorologische Zeitschrift 15:597–609

Mauder M, Foken T (2011) Documentation and instruction manual of the eddy covariance software package TK3. No. 46 in Arbeitsergebnisse, University of Bayreuth, Department of Micrometeorology, URL http://opus.ub.uni-bayreuth.de/opus4-ubbayreuth/frontdoor/index/index/docId/681

Mauder M, Liebethal C, Göckede M, Leps JP, Beyrich F, Foken T (2006) Processing and quality control of flux data during LITFASS-2003. Boundary-Layer Meteorology 121:67–88

Mauder M, Desjardins RL, MacPherson I (2007a) Scale analysis of airborne flux measurements over heterogeneous terrain in a boreal ecosystem. Journal of Geophysical Research 112:D13,112

Mauder M, Desjardins RL, Oncley SP, MacPherson I (2007b) Atmospheric response to a partial solar eclipse over a cotton field in central California. Journal of Applied Meteorology and Climatology 46:1792–1803

Mauder M, Desjardins R, Pattey E, Gao Z, van Haarlem R (2008) Measurement of the sensible eddy heat flux based on spatial averaging of continuous ground-based observations. Boundary-Layer Meteorology 128:151–172

Meek DW, Prueger JH, Kustas WP, Hatfield JL (2005) Determining meaningful differences for SMACEX eddy covariance measurements. Journal of Hydrometeorology 6:805–811

Meijninger WML, Beyrich F, Lüdi A, Kohsiek W, Bruin HARD (2006) Scintillometer-based turbulent fluxes of sensible and latent heat over a heterogeneous land surface - A contribution to LITFASS-2003. Boundary-Layer Meteorology 121:89–110

Metzger S, Junkermann W, Mauder M, Beyrich F, Butterbach-Bahl K, Schmid HP, Foken T (2012) Eddy-covariance flux measurements with a weight-shift microlight aircraft. Atmospheric Measurement Techniques 5:1699–1717

Metzger S, Junkermann W, Mauder M, Butterbach-Bahl K, Trancóny Widemann B, Neidl F, Schäfer K, Wieneke S, Zheng XH, Schmid HP, Foken T (2013) Spatially explicit regionalization of airborne flux measurements using environmental response functions. Biogeosciences 10:2193–2217

Meyers TP, Hollinger SE (2004) An assessment of storage terms in the surface energy balance of maize and soybean. Agricultural and Forest Meteorology 125:105–115

Moore CJ (1986) Frequency response corrections for eddy correlation systems. Boundary-Layer Meteorology 37:17–35

Nakamura R, Mahrt L (2006) Vertically integrated sensible heat budgets for stable nocturnal boundary layers. Quarterly Journal of the Royal Meteorological Society 132:383–403

Nordbo A, Launiainen S, Mammarella I, Leppäranta M, Huotari J, Ojala A, Vesala T (2011) Long-term energy flux measurements and energy balance over a small boreal lake using eddy covariance technique. Journal of Geophysical Research 116:D02,119

Oncley SP, Businger JA, Itsweire EC, Friehe CA, C LJ, Chang SS (1990) Surface layer profiles and turbulence measurements over uniform land under near-neutral conditions. In: 9th Symposium on Boundary Layer and Turbulence, American Meteorological Society, Roskilde, Denmark, pp 237–240

Oncley SP, Foken T, Vogt R, Kohsiek W, DeBruin HAR, Bernhofer C, Christen A, van Gorsel E, Grantz D, Feigenwinter C, Lehner I, Liebethal C, Liu H, Mauder M, Pitacco A, Ribeiro L, Weidinger T (2007) The energy balance experiment EBEX-2000. Part I: overview and energy balance. Boundary-Layer Meteorology 123:1–28

Oncley SP, Schwenz K, Burns SP, Sun J, Monson RK (2009) A cable-borne tram for atmospheric measurements along transects. Journal of Atmospheric and Oceanic Technology 26:462–473

Paw U KT, Baldocchi DD, Meyers TP, Wilson KB (2000) Correction of eddy-covariance measurements incorporating both advective effects and density fluxes. Boundary-Layer Meteorology 97:487–511

Raabe A (1983) On the relation between the drag coefficient and fetch above the sea in the case of off-shore wind in the near-shore zone. Zeitschrift für Meteorologie 33:363–367

Rannik Ü, Sogachev A, Foken T, Göckede M, Kljun N, Leclerc MY, Vesala T (2012) Footprint analysis. In: Aubinet M, Vesala T, Papale D (eds) Eddy Covariance, Springer, Dordrecht, pp 211–261

Ruppert J, Thomas C, Foken T (2006) Scalar similarity for relaxed eddy accumulation methods. Boundary-Layer Meteorology 120:39–63

Schmid HP (2002) Footprint modeling for vegetation atmosphere exchange studies: a review and perspective. Agricultural and Forest Meteorology 113:159–183

Schotanus P, Nieuwstadt F, De Bruin H (1983) Temperature measurement with a sonic anemometer and its application to heat and moisture fluxes. Boundary-Layer Meteorology 26:81–93

Seibert P, Beyrich F, Gryning SE, Joffre S, Rasmussen A, Tercier P (2000) Review and intercomparison of operational methods for the determination of the mixing height. Atmospheric Environment 34:1001–1027

Shaw RH (1985) On diffusive and dispersive fluxes in forest canopies. In: Hutchinson BA, Hicks BB (eds) The Forest-Atmosphere interaction, Reidel Publishing Company, Dordrecht, pp 407–419

Steinfeld G, Letzel M, Raasch S, Kanda M, Inagaki A (2007) Spatial representativeness of single tower measurements and the imbalance problem with eddy-covariance fluxes: results of a large-eddy simulation study. Boundary-Layer Meteorology 123:77–98

Stoy PC, Mauder M, Foken T, Marcolla B, Boegh E, Ibrom A, Arain MA, Arneth A, Aurela M, Bernhofer C, Cescatti A, Dellwik E, Duce P, Gianelle D, van Gorsel E, Kiely G, Knohl A, Margolis H, McCaughey H, Merbold L, Montagnani L, Papale D, Reichstein M, Saunders M, Serrano-Ortiz P, Sottocornola M, Spano D, Vaccari F, Varlagin A (2013) A data-driven analysis of energy balance closure across FLUXNET research sites: The role of landscape scale heterogeneity. Agricultural and Forest Meteorology 171-172:137–152

Stull RB (1988) An Introduction to boundary layer meteorology. Kluwer Academic Publishers, Dordrecht

Tanner BD, Swiatek E, Greene JP (1993) Density fluctuations and use of the Krypton hygrometer in surface flux measurements. In: Allen RG (ed) Management of Irrigation and Drainage Systems: Integrated Perspectives, American Society of Civil Engineers, New York, pp 945–952

Taylor GI (1938) The spectrum of turbulence. Proceedings of the Royal Society of London Series A - Mathematical and Physical Sciences 164:476–490

Taylor PA (1987) Comments and further analysis on effective roughness lengths for use in numerical three-dimensional models. Boundary-Layer Meteorology 39:403–418

Torrence C, Compo GP (1998) A practical guide to wavelet analysis. Bulletin of the American Meteorological Society 79:61–78

Twine TE, Kustas WP, Norman JM, Cook DR, Houser PR, Meyers TP, Prueger JH, Starks PJ, Wesely ML (2000) Correcting eddy-covariance flux underestimates over a grassland. Agricultural and Forest Meteorology 103:279–300

Vesala T, Kljun N, Rannik Ü, Rinne J, Sogachev A, Markkanen T, Sabelfeld K, Foken T, Leclerc M (2008) Flux and concentration footprint modelling: State of the art. Environmental Pollution 152:653–666

Warner TT (2011) Numerical Weather and Climate Prediction. Cambridge University Press, Cambridge

Webb EK, Pearman GI, Leuning R (1980) Correction of flux measurements for density effects due to heat and water vapour transfer. Quarterly Journal of the Royal Meteorological Society 106:85–100

Wilczak J, Oncley S, Stage S (2001) Sonic anemometer tilt correction algorithms. Boundary-Layer Meteorology 99:127–150

Wilson JD, Sawford BL (1996) Review of Lagrangian stochastic models for trajectories in the turbulent atmosphere. Boundary-Layer Meteorology 78:191–210

Appendix A

Individual contribution to the joint publication

Charuchittipan, D., Babel, W., Mauder, M., Leps, J.-P., and Foken, T.: Extension of the averaging time of the eddy-covariance measurement and its effect on the energy balance closure, submitted to Boundary-Layer Meteorology

- I partly developed the idea of this manuscript. I conducted the whole data analysis, wrote the text and act as the corresponding author of the manuscript.
- Wolfgang Babel developed the proposed new energy balance closure correction algorithm together with me and realised the respective part in the conclusions.
- Matthias Mauder initiated the use block ensemble average and wavelet analysis to the data from the LITFASS-2003 experiment. He also participate in the LITFASS-2003 experiment.
- Jens-Peter Leps provided data from several measuring stations of the LITFASS-2003 experiment. He also participate in the LITFASS-2003 experiment.
- Thomas Foken encouraged the structure of the manuscript and contributed with many scientific discussions. Furthermore, he initiated the project related to the manuscript.

Declaration / Erklärung

I hereby declare, to the best of my knowledge and belief, that this thesis does not contain any material previously published or written by another person, except where due reference has been made in the text. This thesis contains no material, which has been previously accepted or definitely rejected for award of any other doctoral degree at any university or equivalent institution.

Hiermit erkläre ich, dass ich die vorliegende Promotionsarbeit selbständig verfasst und keine anderen als die angegebenen Quellen und Hilfsmittel benutzt habe.

Hiermit erkläre ich, dass ich nicht bereits anderweitig versucht habe, diese Dissertation ohne Erfolg einzureichen oder mich einer Doktorprfung zu unterziehen.

Hiermit erkläre ich, dass ich die Hilfe von gewerblichen Promotionsberatern bzw. -vermittlern weder bisher in Anspruch genommen habe, noch knftig in Anspruch nehmen werde.

Bayreuth, den _____ _____

Doojdao Charuchittipan